DISS. ETH NO. 26469

MODELING OF SUBSURFACE SCATTERING FROM ICE SHEETS FOR POL-INSAR APPLICATIONS

A thesis submitted to attain the degree of
DOCTOR OF SCIENCES of ETH ZURICH
(Dr. sc. ETH Zurich)

presented by

GEORG FISCHER

M.Sc. Environmental Systems and Sustainability: Monitoring, Modeling, Management
Ludwig-Maximilians-Universität München (LMU)

born on 29.03.1986
citizen of Germany

accepted on the recommendation of

Prof. Dr. Irena Hajnsek
Prof. Dr. Jonathan Bamber
Prof. Dr. Jørgen Dall
Prof. Dr. Laurent Ferro-Famil
Prof. Dr. Helmut Rott
Prof. Dr. Konrad Steffen

2019

ABSTRACT

Remote sensing is a fundamental tool to measure the dynamics of ice sheets and provides valuable information for ice sheet projections under a changing climate. There is, however, the potential to further reduce the uncertainties in these projections by developing innovative remote sensing methods. One of these remote sensing techniques, the polarimetric synthetic aperture radar interferometry (Pol-InSAR), is known since decades to have the potential to assess the geophysical properties below the surface of ice sheets, because of the penetration of microwave signals into dry snow, firn, and ice. Despite this, only very few studies have addressed this topic and the development of robust Pol-InSAR applications is at an early stage. Two potential Pol-InSAR applications are identified as the motivation for this thesis. First, the estimation and compensation of the penetration bias in digital elevation models derived with SAR interferometry. This bias can lead to errors of several meters or even tens of meters in surface elevation measurements. Second, the estimation of geophysical properties of the subsurface of glaciers and ice sheets using Pol-InSAR techniques. There is indeed potential to derive information about melt-refreeze processes within the firn, which are related to density and affect the mass balance. Such Pol-InSAR applications can be a valuable information source with the potential for monthly ice sheet wide coverage and high spatial resolution provided by the next generation of SAR satellites. However, the required models to link the Pol-InSAR measurements to the subsurface properties are not yet established.

The aim of this thesis is to improve the modeling of the vertical backscattering distribution in the subsurface of ice sheets and its effect on polarimetric interferometric SAR measurements at different frequencies.

In order to achieve this, polarimetric interferometric multi-baseline SAR data at different frequencies and from two different test sites on the Greenland ice sheet are investigated. This thesis contributes with three concepts to a better understanding and to a more accurate modeling of the vertical backscattering distribution in the subsurface of ice sheets. First, the integration of scattering from distinct subsurface layers. These are formed by refrozen melt water in the upper percolation zone and cause an interesting coherence undulation pattern, which cannot be explained with previously existing models. This represents a first link between Pol-InSAR data and geophysical subsurface properties. The second step is the improved modeling of the general vertical backscattering distribution of the subsurface volume. The advantages of more flexible volume models are demonstrated, but interestingly, the simple modification of a previously existing model with a vertical shift parameter lead to the best agreement between model and data. The third contribution is the model based compensation of the penetration bias, which is experimentally validated. At the investigated test sites, it becomes evident that the model based estimates of the surface elevations are more accurate than the interferometric phase center

locations, which are conventionally used to derive surface elevations of ice sheets. This thesis therefore improves the state of the art of subsurface scattering modeling for Pol-InSAR applications, demonstrates the model-based penetration bias compensation, and makes a further research step towards the retrieval of geophysical subsurface information with Pol-InSAR.

ZUSAMMENFASSUNG

Die Fernerkundung ist ein wichtiges Instrument zur Messung der Dynamik von Eisschilden und trägt wertvolle Informationen zu Klimaprojektionen von Eisschilden bei. Innovative Fernerkundungsmethoden haben jedoch das Potential die Unsicherheiten in solchen Klimaprojektionen weiter zu reduzieren. Eine dieser Fernerkundungsmethoden ist das Verfahren der polarimetrischen Interferometrie mit synthetischem Apertur Radar (Pol-InSAR), die das Potential hat, die geophysikalischen Eigenschaften unter der Oberfläche von Eisschilden zu erfassen. Dies ist möglich da Mikrowellensignale in trockenen Schnee, Firn und Eis eindringen können. Allerdings haben sich bisher nur sehr wenige Studien mit diesem Thema beschäftigt und die Entwicklung von Pol-InSAR Anwendungen befindet sich in einem frühen Stadium. Zwei mögliche Pol-InSAR Anwendungen dienen als Motivation für diese Arbeit. Erstens, die Schätzung und Kompensation eines systematischen Fehlers in digitalen, mit SAR Interferometrie erstellten, Höhenmodellen von Eisschilden, der aufgrund der Eindringtiefe der Mikrowellensignale entsteht. Dies kann zu Fehlern von mehreren Metern oder sogar Dutzenden von Metern in den Höhenmodellen führen. Zweitens, die Erfassung von geophysikalischen Eigenschaften unterhalb der Oberfläche von Gletschern und Eisschilden mit Pol-InSAR Techniken. Hier besteht das Potential, Informationen über Schmelz-Gefrier-Prozesse im Firn abzuleiten, die die Dichte verändern und damit die Massenbilanz beeinflussen. Aufgrund des Potentials einer monatlichen Abdeckung der Eisschilde mit einer hohen räumlichen Auflösung, wie es die nächste Generation von SAR-Satelliten ermöglichen wird, können solche Pol-InSAR Anwendungen eine wertvolle Informationsquelle sein. Die erforderlichen Modelle, die eine Verbindung zwischen den Pol-InSAR Messungen und den Gegebenheiten unterhalb der Oberfläche herstellen, sind jedoch noch nicht entwickelt.

Das Ziel dieser Arbeit ist die Verbesserung der Modellierung der vertikalen Rückstreuungsverteilung unterhalb der Oberfläche von Eisschilden und ihrer Auswirkungen auf polarimetrische interferometrische SAR Messungen in verschiedenen Frequenzen.

Um das zu erreichen werden polarimetrische und interferometrische SAR Daten mit multiplen Basislinien in verschiedenen Frequenzen und von zwei verschiedenen Testgebieten auf dem grönländischen Eisschild untersucht. Diese Arbeit trägt mit drei Konzepten zu einem besseren Verständnis und zu einer präziseren Modellierung der vertikalen Rückstreuungsverteilung unterhalb der Oberfläche von Eisschilden bei. Erstens, die Berücksichtigung von stark streuenden Schichten, die durch wiedergefrorenes Schmelzwasser in der oberen Perkolationszone gebildet werden. Diese Schichten verursachen ein aufschlussreiches Kohärenzmuster, dass mit bisher existierenden Modellen nicht zu erklären ist. Dadurch kann eine erste Verbindung zwischen Pol-InSAR Messungen und geophysikalischen Eigenschaften hergestellt werden. Der zweite Schritt ist die verbesserte Modellierung der

allgemeinen vertikalen Rückstreuungsverteilung im Volumen unterhalb der Oberfläche. Die Vorteile flexiblerer Volumenmodelle werden aufgezeigt, aber interessanterweise führt die einfache Modifikation eines schon existierenden Modells mit einem vertikalen Verschiebungsparameter zur besten Übereinstimmung zwischen Modell und Daten. Der dritte Beitrag ist die modellbasierte Kompensation der Eindringtiefe, die experimentell validiert wird. In den untersuchten Testgebieten zeigt sich, dass die modellbasierten Schätzungen der Oberflächenhöhen genauer sind als die Lage der interferometrischen Phasenzentren, die üblicherweise zur Ableitung von Oberflächenhöhen von Eisschilden verwendet werden. Diese Arbeit verbessert daher den Stand der Technik der Streuungsmodellierung für Pol-InSAR Anwendungen von Eisschilden, demonstriert die modellbasierte Kompensation der Eindringtiefe und macht einen weiteren Forschungsschritt hin zur Ableitung geophysikalischer Eisschildinformationen mit Pol-InSAR.

ACKNOWLEDGEMENTS

At the time, when my idea of pursuing a PhD became reality by joining DLR, I was excited to start with the research, I had some dreams which I expected to be unrealistic, and I anticipated demanding challenges which I was not sure if I am capable of. Now I can say that, in the frame of my PhD, things became reality that go beyond those dreams and that I learned by far more than what I expected. I am utterly grateful that I had the opportunity to conduct the research which lead to this thesis and to make many valuable experiences, both on a scientific and a personal level. Fundamental to this are all the great people that were a part of this journey.

First and foremost, I want to express my deepest gratitude to Irena, who gave me the opportunity to pursue a PhD with a fascinating topic in an environment of highest expertise. Thank you for all your supervision and guidance, both scientifically and personally, and thank you for the freedom I had in the evolution of my research topics. I consider it something very special that you trusted me in defining the test sites in Greenland and gave me the opportunity to actually go there to conduct the campaign, which was one of the best experiences in my life.

At the time, it was Kostas who sparked the idea of applying for a PhD at DLR. Thank you for always asking the right and the tough questions, for being a challenging internal reviewer, as well as finding ways to improve the structure and clarity of manuscripts and presentations. Thank you also to Gerhard Krieger and Alberto Moreira for the possibility to work in such an interdisciplinary research environment in the department and the institute. Further, I would like to acknowledge Jonathan Bamber, Jørgen Dall, Laurent Ferro-Famil, Helmut Rott, and Konrad Steffen for accepting to be co-examiners of my work.

My entire PhD evolved around the ARCTIC15 campaign in Greenland and I cannot value the effort of everyone involved high enough. I want to specially mention Silvan and Martin, my field work fellows. I really enjoyed the strong motivation and high team spirit we had, even in stormy -27°C with freezing 30 knots of wind. Silvan, Martin, this was an experience with you that I will never forget. A huge thank you to everyone else who contributed to a successful campaign in Greenland. To Ralf, Daniel, and all the guys from DLR-FX who made the F-SAR acquisitions possible. It was great how everyone worked hard for a successful campaign, did not care about German working hour limits and cooperated across disciplines. And we came home with two more test sites than we had originally planned! This was of course also due to lucky weather, but even more so due to the effort of everyone in the team. Thanks also to everyone behind the scenes, I cannot name all of you. A big thank you to the processing guys Marc, Rolf, Jens, and Martin. In particular to Marc for his strong motivation for improving the data quality through additional processing iterations.

Thank you to all the colleagues in the Pol-InSAR and Information Retrieval groups at DLR. You were not only very valuable in sharing your expertise, but contributed to a fun and stimulating atmosphere and became my friends. Giuseppe, you are the best office mate, my personal polarimetry advisor, and I highly value all the fun we had, the good conversations, the

many hours of technical discussions, as well as the probably even more hours of bilateral therapy about PhD-life. Hannah and Matteo, thank you for helping me so much in the worlds of Pol-InSAR and tomography and for the great times during daily life and on conferences. Victor, it was great to go through the PhD with you and to share our common journey towards the finish line. Thank you to Jun Su, Alberto, Sandra, Thomas, Changhyun, and Roman as well as the ones who left the group during the last years. You made it an amazing international experience.

A big thank you to my mother who always believed in me and supported me. It is impossible to name all the big and small things you contributed to me being able to achieve a PhD. Thanks also to my sister, who is always there for me. You two make me always feel at home. At last and most importantly: Sarah, all the years as a PhD student were the happiest ever, even during the most frustrating days, thanks to you.

CONTENTS

LIST OF ABBREVIATIONS

ARCTIC15	Experimental airborne SAR campaign in Greenland
AWI	Alfred-Wegener-Institute, Germany
C-band	Frequency of 5.3 GHz, wavelength of 5.7 cm in case of F-SAR
CryoSAT-2	Radar altimetry satellite operated by ESA
CryoVex	CryoSAT-2 calibration and validation campaign
m a. s. l.	Meters above sea level
DEM	Digital elevation model
DLR	Deutsches Zentrum für Luft- und Raumfahrt (German Aerospace Center)
EGIG	Expéditions Glaciologiques Internationales au Groenland
F-SAR	Airborne SAR sensor owned and operated by DLR
GC-Net	Greenland Climate Network
GNSS	Global Navigation Satellite System
GPR	Ground Penetrating Radar
HH	Horizontal receive, horizontal transmit
HV	Horizontal receive, vertical transmit
IceSAT-2	Laser altimetry satellite operated by NASA
InSAR	Synthetic Aperture Radar Interferometry
L-band	Frequency of 1.3 GHz, wavelength of 23 cm in case of F-SAR
MUSIC	Multiple signal classification algorithm
NASA	National Aeronautics and Space Administration
P-band	Frequency of 0.44 GHz, wavelength of 69 cm in case of F-SAR
PolSAR	Polarimetric Synthetic Aperture Radar
Pol-InSAR	Polarimetric Synthetic Aperture Radar Interferometry
PPP	Precise Point Positioning
PROMICE	Programme for Monitoring of the Greenland Ice Sheet
Radar	Radio Detection and Ranging
Radarsat-2	Canadian SAR satellite operating at C-band
RTK	Real time kinematic
RVuG	Random-Volume-under-Ground
S-band	Frequency of 3.3 GHz, wavelength of 9.2 cm in case of F-SAR
SAR	Synthetic Aperture Radar
Seasat	First earth observation satellite with a SAR sensor operated by NASA
Sentinel-1	SAR satellite operated by ESA
SLC	Single-look-complex
SNR	Signal-to-noise ratio
SRTM	Shuttle Radar Topography Mission
Tandem-L	L-band SAR mission currently developed by DLR as successor of TanDEM-X

TanDEM-X	X-band single-pass SAR mission operated by DLR
UV	Uniform volume
VH	Vertical receive, horizontal transmit
VV	Vertical receive, vertical transmit
X-band	Frequency of 9.6 GHz, wavelength of 3.1 cm in case of F-SAR

LIST OF SYMBOLS

α	Mean alpha angle [°]
$a(z)$	Steering vector
γ	Complex interferometric coherence
γ_g	Coherence of the Gaussian model
γ_{max2}	Coherence at the position of the second maximum
γ_{min}	Coherence at the position of the minimum
γ_{proc}	Minor decorrelation contributions
γ_{range}	Range spectral decorrelation
γ_{SNR}	Noise decorrelation
γ_{temp}	Temporal decorrelation
γ_{uv}	Coherence of the UV model
γ_{vol}	Volumetric coherence
γ_w	Coherence of the Weibull model
Γ_v	Volume-only coherence matrix
d_{pen}	One-way penetration depth [m]
δ	Dirac delta function
δ_g	Mean of the Gaussian model [m]
$\vec{e}_i$	Eigenvectors of T
ϵ_r	Relative permittivity
H	Polarimetric scattering entropy
HoA	Height of ambiguity [m]
i	Imaginary unit
K	Number of tracks in a multi-baseline InSAR configuration
$\vec{k}_{3P}$	Pauli scattering vector
κ_e	Extinction coefficient [Nepers/m], conventionally expressed in [dB/m]
k_w	Weibull shape parameter
k_z	Interferometric vertical wavenumber [rad/m]
k_{zVol}	Vertical wavenumber in a volume [rad/m]
λ	Wavelength [m]
λ_i	Eigenvalues of T
λ_w	Weibull scale parameter
m	Layer-to-volume scattering ratio
N	Number of layers
p_j	Backscatter power of layer j
p_v	Volume backscatter power
R	Multi-baseline InSAR covariance matrix

S_{ij}	Scattering matrix element at polarization ij
s_j	SAR acquisition j
$\sigma_g(z)$	Vertical backscattering distribution of the Gaussian model
σ_{L_j}	Backscatter power of layer j
$\sigma_{uv}(z)$	Vertical backscattering distribution of the UV model
$\sigma_v(z)$	Vertical backscattering distribution
σ_v^0	Nominal backscatter power per unit volume
$\sigma_w(z)$	Vertical backscattering distribution of the Weibull model
T	Polarimetric coherency matrix
θ	Incidence angle [rad]
$\Delta\theta$	Difference in θ between interferometric SAR acquisitions [rad]
θ_r	Refracted incidence angle [rad]
$\Delta\theta_r$	Difference in θ_r between interferometric SAR acquisitions [rad]
$\vec{w}$	Polarization state
χ	Standard deviation of the Gaussian model
y	Multi-baseline InSAR data vector
z	Height (depth) axis [m]
z_0	Surface reference location [m], mostly defined as $z_0 = 0\ m$
z_j	Position of layer j [m]
z_{ul}	Upper limit of the UV model [m]
$(\cdot)^T$	Transpose
$(\cdot)^*$	Complex conjugate
$(\cdot)^H$	Complex conjugate transpose
$\langle\cdot\rangle$	Expectation value
$\lvert\cdot\rvert$	Magnitude
$\angle\cdot$	Phase

1 INTRODUCTION

1.1 MOTIVATION AND PROBLEM STATEMENT

Understanding and quantifying the dynamics of glaciers and ice sheets and their implications on environment and society is an important task, particularly in the context of climate change [1], which was reaffirmed recently [2]. One major question is how the mass losses of the Greenland and Antarctic ice sheets contribute to sea level rise. The Greenland ice sheet lost on average 278 ± 11 Gt of mass per year between 2006 and 2015, which is double the rate of the previous 10-year period [2]. The mass loss accelerated in the 2000s, while being rather balanced in the early 1990s [3]. Remote sensing measurements are essential for mass balance estimations and established methods exist to determine the changing extent of glaciers and ice sheets, their flow velocity, gravity anomalies, and the change in surface elevation. Laser (e.g. ICESat-2) and radar (e.g. CryoSat-2) altimeters provide surface elevation information for mass balance estimations with high vertical accuracy and are particularly suited for measurements over smooth terrain like the interior of the Greenland and Antarctic ice sheets [4], [5], [6], [7]. Also, synthetic aperture radar interferometry (InSAR) is one of the established methods to measure surface elevation of ice sheets [8]. In comparison to altimeters, data from current SAR missions, like TanDEM-X [9], Radarsat-2 [10], and Sentinel-1 [11], have the advantage of larger coverage and better spatial resolution. The surface elevations obtained with InSAR are used to derive volume and mass changes of glaciers and ice sheets [12], [13], [14] and to assess glacier dynamics [15]. Future missions, like Tandem-L [16], have the potential of monitoring entire ice sheets on a monthly basis with few tens of meters spatial resolution. This will provide the means to further refine the accuracy of glacier and ice sheet mass loss estimates and improve the understanding of land ice contributions to sea level rise. However, InSAR measurements of surface elevation are affected by a bias due to the penetration of the microwave signals into snow, firn, and ice under dry and frozen conditions. This penetration bias is the difference between the actual surface and the location of the interferometric phase center in the subsurface. It depends on the snow and ice conditions as well as on the acquisition parameters, i.e. polarization, frequency and interferometric baseline [17], [18]. Penetration bias values as large as -1 m to -10 m at X-band (in the transition from the percolation to the dry snow zone in Greenland) [8], down to -13 m at C-band (with decreasing trend with increasing elevation in the percolation zone) [19], and -14 m at L-band (Greenland Summit) [20], with rare cases down to -120 m (cold marginal ice) [20], have been reported. Since the bias, and its temporal change, can be larger than the measured surface elevation change, it can directly translate into significant errors in mass balance estimations. It is evident that tools have to be developed, which improve the accuracy of surface elevation measurements from InSAR through a better correction of penetration effects.

The snow and ice conditions as well as the acquisition parameters affect the scattering characteristics of the subsurface. From an interferometric perspective, it is the vertical distribution of scatterers that determines the penetration bias. Therefore, there is potential to estimate and compensate this bias through modeling of the vertical backscattering distribution in the subsurface of ice sheets and its effect on InSAR measurements, which is addressed in this thesis.

A second motivation for interferometric subsurface scattering modeling is to exploit the relationship to geophysical properties of ice sheets. Interferometric models can provide the foundation for future approaches deriving geophysical information about the subsurface from SAR data. Similar to the penetration bias, the essential link is here again the sensitivity of InSAR to the distribution of scatterers in the subsurface. Geophysical parameters like density, firn stratigraphy, accumulation rate, and the presence of melt-refreeze features are considered to affect InSAR measurements. However, it is not yet fully understood how these characteristics of the subsurface influence the vertical backscattering distribution and thus the InSAR measurements. Therefore, the methodology and the algorithms to extract geophysical subsurface parameters from SAR data are not yet established. The extraction of subsurface information could address uncertainties in mass balance estimations from remote sensing data. When mass balance estimations are carried out through the measurement of volume changes, uncertainty arises from changes in density [1], [4]. For instance, a reduction in surface elevation does not necessarily imply a mass loss, but can be due to an increase in firn density through compaction or refreezing of melt water. This is typically addressed by firn densification models [21], [22], [23]. Additionally, it was reported in [24] that 30% of the increase in melt water generated on the Greenland ice sheet in the years 1996 – 2008 refroze in the firn and thus did not contribute to mass loss, based on a regional climate model. Here, the link between InSAR measurements and the subsurface structure of ice sheet has the potential of providing an additional information source on densification and melt-refreeze processes.

This thesis aims to provide a modeling foundation for future applications addressing the two described phenomena: First, towards the correction of the penetration bias in InSAR digital elevation models (DEMs) over glaciers and ice sheets; Second, towards the retrieval of geophysical subsurface structure information. Polarimetric InSAR (Pol-InSAR) [25] and multi-baseline InSAR (SAR Tomography) [26] are essential techniques for this task, due to their sensitivity to the vertical backscattering distribution and are thus fundamental for this thesis. At the same time, it is important to establish the modeling foundation for future approaches of penetration bias correction and subsurface information retrieval that exploit the Pol-InSAR and tomographic imaging capabilities of future SAR missions, particularly at longer wavelengths [16].

1.2 SAR Techniques for Ice Sheet Observations

Synthetic aperture radar (SAR) data have the advantage of a large coverage, high revisit time, day and night imaging capability at (almost) all weather conditions [27]. Spatial

resolutions on the order of few meters make them suitable not only for the smooth interior of ice sheets, but also for outlet glaciers and alpine glaciers typically characterized by more complex topography.

The basic principle of SAR [27] is a side-looking radar, typically operating on an airborne or space borne platform, that actively transmits electromagnetic pulses. The echoes of the transmitted signals that are backscattered from the illuminated area on the ground are received by the SAR sensor. The received signals mainly depend on geometric (i.e. roughness, size, orientation) and dielectric (i.e. permittivity) properties of the scatterers on the Earth's surface. The 2-D imaging capability is achieved by determining the across-track (range) position of the signals from their travel time, and the along-track (azimuth) position by their Doppler frequency. The 2-D spatial resolutions are achieved by exploiting the signal bandwidth in the range direction, and the Doppler bandwidth in azimuth direction sampled along the flight track to form a synthetic aperture [27]. The intensity of the backscattered signals measured by SAR systems is used for the imaging and monitoring of ice sheets and some of its aspects are addressed in Section 1.4.

1.2.1 SAR POLARIMETRY

Transmitting and receiving in orthogonally polarized channels extends the single-channel SAR concept to *polarimetric SAR* (PolSAR). PolSAR sensors measure the full scattering matrix of the imaged area in HH, HV, VH, and VV channels, when employing the linear horizontal and vertical polarizations on transmit and receive. The polarimetric concepts relevant for this thesis are briefly summarized here. A more complete overview on PolSAR can be found in [28] and [29]. The complex scattering matrix

$$\mathrm{S} = \begin{bmatrix} S_{HH} & S_{HV} \\ S_{VH} & S_{VV} \end{bmatrix} \tag{1}$$

is the fundamental observable of a PolSAR system, which provides a more complete and detailed insight into the scattering mechanisms in each resolution cell. S_{HH} and S_{VV} are commonly termed co-polarized channels, while S_{HV} and S_{VH} are the cross-polarized channels. For monostatic systems, where transmitter and receiver are collocated, reciprocity is assumed for most natural scattering media, so that S is a symmetric matrix with $S_{HV} = S_{VH}$.

Deterministic point-like scatterers can be fully described by the S matrix. In contrast, the scattering from distributed targets, which can be understood as a set of point scatterers within one resolution cell, needs statistical descriptors. For this, the concepts of the *Pauli scattering vector* and the *coherency matrix* are introduced. The Pauli scattering vector has the advantage of a close relationship to physical scattering mechanisms [29]

$$\vec{k}_{3P} = \frac{1}{\sqrt{2}}[S_{HH} + S_{VV},\ S_{HH} - S_{VV},\ 2S_{HV}]^T \tag{2}$$

The first element of the Pauli vector $S_{HH} + S_{VV}$, is typically interpreted as the contribution from surface scattering, or more general any odd-bounce scattering. $S_{HH} - S_{VV}$ indicates even bounce contributions, mainly from dihedral structures. S_{HV} represents depolarizing volume scattering in natural media.

Based on the scattering vector, the second order statistics can be derived to describe distributed scatterers. The polarimetric coherency matrix T is the outer product of the Pauli scattering vector with its complex conjugate transpose [29]

$$T = \langle \vec{k}_{3P} \vec{k}_{3P}^{H} \rangle = \\ = \frac{1}{2} \begin{bmatrix} \langle |S_{HH} + S_{VV}|^2 \rangle & \langle (S_{HH} + S_{VV})(S_{HH} - S_{VV})^* \rangle & 2\langle (S_{HH} + S_{VV}) S_{HV}^* \rangle \\ \langle (S_{HH} - S_{VV})(S_{HH} + S_{VV})^* \rangle & \langle |S_{HH} - S_{VV}|^2 \rangle & 2\langle (S_{HH} - S_{VV}) S_{HV}^* \rangle \\ 2\langle S_{HV}(S_{HH} + S_{VV})^* \rangle & 2\langle S_{HV}(S_{HH} - S_{VV})^* \rangle & 4\langle |S_{HV}|^2 \rangle \end{bmatrix} \quad (3)$$

where ^{H} denotes the complex conjugate transpose, * the complex conjugate, and $\langle \cdot \rangle$ the expectation value, which is estimated through spatial averaging of neighboring resolution cells.

For natural media, the scattering in a resolution cell is often the superposition of more than one scattering mechanism. The separation and interpretation of the different scattering contributions is performed by means of decompositions of the coherency matrix T. One of the approaches is based on the analysis of eigenvalues λ_i and eigenvectors $\vec{e}_i$ of the T matrix. This can be seen as a decomposition of T into three statistically independent scattering contributions, each described by one combination of λ_i and $\vec{e}_i$ [28].

The polarimetric scattering entropy parameter H describes the distribution of the underlying scattering mechanisms based on the eigenvalues of T

$$H = \sum_{i=1}^{3} -P_i \log_3 P_i \;\; ; \;\; P_i = \frac{\lambda_i}{\lambda_1 + \lambda_2 + \lambda_3} . \quad (4)$$

An entropy of 0 indicates only one non-zero eigenvalue, meaning that only one scattering mechanism is present in the resolution cell. A value of 1 indicates three equal eigenvalues and the superposition of three equally strong scattering mechanisms.

The mean alpha angle α, ranging between 0° and 90°, is derived from the first element of each eigenvector $\vec{e}_{i,1}$ of T and indicates the type of the average scattering mechanism in the resolution cell

$$\alpha = \sum_{i=1}^{3} P_i \cos^{-1} \vec{e}_{i,1} . \quad (5)$$

Low alpha values ($\alpha < 30°$) are typically interpreted as surface scattering, intermediate values as volume scattering from randomly oriented particles, and high values approaching 90° as double bounce. The advantages of PolSAR for ice sheet monitoring are summarized in Section 1.4.1, which are mainly related to the characterization of different scattering processes.

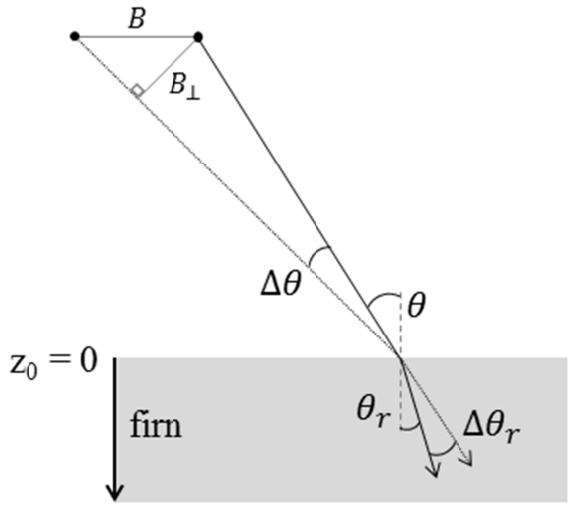

Fig. 1. InSAR geometry of two SAR sensors separated by a spatial across-track baseline B considering the refraction into the subsurface of an ice sheet.

1.2.2 SAR INTERFEROMETRY

While PolSAR allows the characterization of scattering mechanisms, the vertical location of the scatterer can be measured with *SAR interferometry* (InSAR). The concept of interferometry allows measuring phase differences between two coregistered SAR scenes acquired from airborne flight tracks or satellite orbits that are spatially separated in across-track direction. These phase differences correspond to differences in range distance between a scatterer and the two sensor positions. The spatial distance between the sensor positions is called baseline. Other interferometric techniques exploit separation in time or spatial separation in along-track, but are not within the scope of this thesis. InSAR principles are well described in [27] and [30] and are briefly summarized in the following.

This thesis focusses on across-track interferometry in the case of negligible temporal separation between the two SAR acquisitions. Therefore, the contributions to the interferometric measurements are mainly the topography of the scene and the vertical distribution of the scatterers within one resolution cell. The acquisition geometry for this scenario is shown in Fig. 1.

The phase to height conversion, which depends on the acquisition geometry, is described by the vertical wavenumber k_z

$$k_z = \frac{4\pi}{\lambda}\frac{\Delta\theta}{sin\theta}, \tag{6}$$

with the radar wavelength λ, the incidence angle θ, and the difference in incidence angles between the two acquisitions $\Delta\theta$. The phase to height conversion with the vertical wavenumber k_z is used, for instance, to derive surface topography for measuring ice sheet volume changes. Related to the vertical wavenumber is also the height of ambiguity, which describes the height of the 2π-interval of the interferometric phase

$$HoA = 2\pi/k_z. \tag{7}$$

Under dry and frozen conditions, microwave signals penetrate into snow, firn, and ice and the backscattered echoes are received from a few meters to tens of meters below the surface at typical SAR system frequencies. In this case, the phase to height relationship in the subsurface volume depends additionally on the permittivity ϵ_r of the medium, which influences the propagation speed of the electromagnetic wave and the refraction of the wave at the surface. This leads to the *vertical wavenumber in the volume* k_{zVol} [19], [31]

$$k_{zVol} = \frac{4\pi\sqrt{\epsilon_r}}{\lambda}\frac{\Delta\theta_r}{sin\theta_r}, \tag{8}$$

where the refracted incidence angle θ_r, and its difference between the sensors $\Delta\theta_r$, are derived by Snell's law.

The correlation coefficient between the two acquisitions s_1 and s_2 of an interferometric image pair is measured by the *complex coherence* γ

$$\gamma = \frac{\langle s_1 s_2^* \rangle}{\sqrt{\langle s_1 s_1^* \rangle \langle s_2 s_2^* \rangle}}, \tag{9}$$

which is estimated by spatial averaging. Its magnitude $|\gamma|$ corresponds to the amount of correlation between the two images. Its phase $\angle\gamma$ is the phase difference between the two acquisitions, corresponding to the range difference between the phase center of the investigated resolution cells and the two sensors. After conventional InSAR processing, the location of the phase center can be converted to its elevation by dividing the phase $\angle\gamma$ by k_z, which describes the surface topography if there is no signal penetration. If the phase center is within the subsurface of an ice sheet, its depth can be derived by using k_{zVol}, given appropriate surface elevation references.

The coherence magnitude $|\gamma|$ can vary between 1 and 0, indicating full correlation and complete decorrelation, respectively, between the interferometric image pair. The observed coherence can be described as a product of several decorrelation sources:

$$\gamma = \gamma_{vol}\gamma_{temp}\gamma_{SNR}\gamma_{range}\gamma_{proc}. \tag{10}$$

γ_{vol}, the *volumetric coherence*, depends on the vertical distribution of the scatterers in the subsurface. This is the main coherence contribution of interest in this thesis, because it provides the link to the subsurface of ice sheets. This quantity is thoroughly described and investigated in all main chapters of this thesis and is expressed as

$$\gamma_{Vol} = e^{ik_z z_0}\frac{\int_{-\infty}^{0}\sigma_v(z)e^{ik_{zVol}z}dz}{\int_{-\infty}^{0}\sigma_v(z)dz}, \tag{11}$$

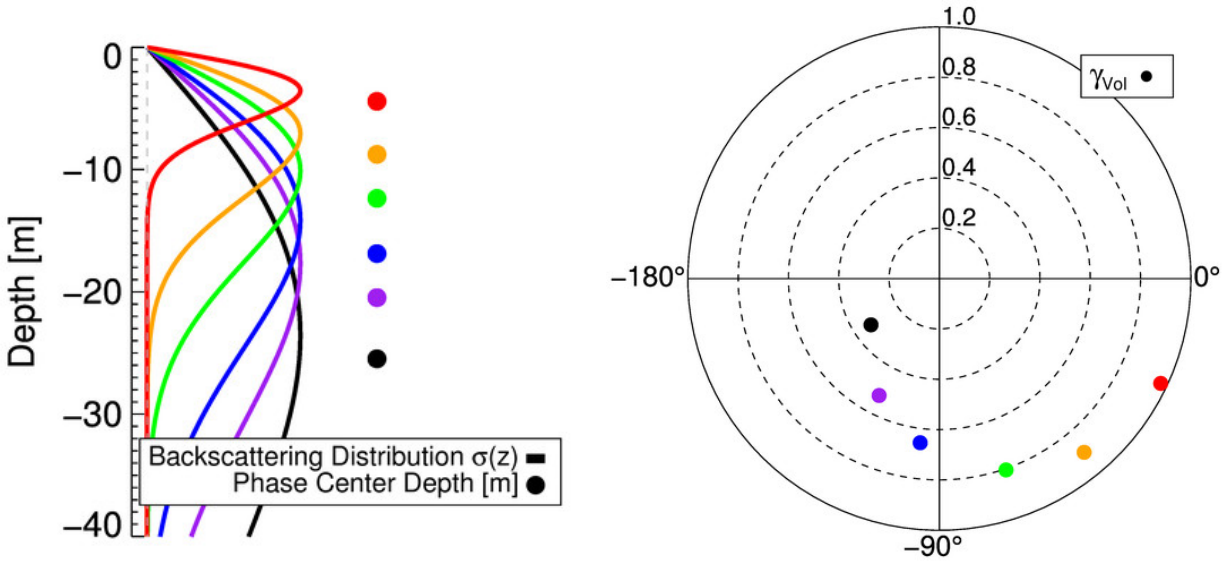

Fig. 2. (Left) Simulations of different vertical backscattering distributions $\sigma_v(z)$ and their respective phase center depths. (Right) The effect of the different $\sigma_v(z)$ on the volume coherences γ_{Vol}, simulated for $k_{zVol} = 0.1$, shown in the unit circle. The locations of the complex valued coherences in the unit circle change towards lower phase and magnitude values, when $\sigma_v(z)$ becomes deeper and more widely distributed.

where $e^{ik_z z_0}$ is the topographic phase of the surface and $\sigma_v(z)$ is the vertical backscattering distribution in the subsurface, which extends from the surface downwards. This leads to some fundamental behavior, shown in Fig. 2. The magnitude $|\gamma_{Vol}|$ depends on the shape and spread of $\sigma_v(z)$ along z. If $\sigma_v(z)$ is very narrow or even a point-like scattering, γ_{Vol} tends to 1. A wide distribution of $\sigma_v(z)$ leads to strong volume decorrelation and very low $|\gamma_{Vol}|$ values that can eventually reach 0. The interferometric phase center $\angle\gamma_{Vol}$ corresponds to the centroid of the vertical distribution of backscattering in a given resolution cell. The deeper the scattering contributions are below the surface, the deeper is the phase, respectively the location of the phase center $\angle\gamma_{Vol}/k_{zVol}$.

γ_{temp} is the temporal decorrelation, caused by temporal changes of the scattering processes between the acquisitions. This can have a strong influence on InSAR monitoring of ice sheets, for instance through melting processes, which can lead to strong decorrelation [32]. In the context of this thesis, the effect of temporal decorrelation can be neglected, due to the short temporal separation of the interferometric acquisitions under stable and frozen conditions.

γ_{SNR} is the noise decorrelation and depends on the noise level of the SAR system and the backscattered intensity. It is typically only problematic for areas with low backscattering and can be mitigated based on the HV and VH channels of a fully polarimetric system. The backscattered signals in these two cross-polarized channels are expected to be completely correlated under the assumption of reciprocity. Therefore, the decorrelation between the two channels indicates the level of noise decorrelation in the system and can thus be used to calculate and compensate for γ_{SNR} [33]. In the data used in this thesis, the effect of noise decorrelation is marginal, because the high backscatter levels lead to γ_{SNR} values always above 0.94 and mostly above 0.99.

γ_{range} is the range spectral decorrelation, which results from imaging the same area on the ground from slightly different viewing angles due to the baseline separation. This can be understood as a frequency shift in the spectra of the backscattered signals, which increases with baseline. Its effect can be filtered by retaining only the overlapping part of the spectra [34].

γ_{proc} comprises different minor decorrelation sources, e.g. coregistration errors or quantization noise [35]. These contributions are usually negligible compared to the previously described decorrelation sources.

1.2.3 POLARIMETRIC SAR INTERFEROMETRY

Adding the polarimetric observation space to SAR interferometry leads to the concept of *Polarimetric SAR Interferometry (Pol-InSAR)* extending the interferometry principle by deriving interferometric coherences at different polarizations [25]. The advantage is that the coherence of different scattering processes can be observed, which provides insights into their vertical location and distribution. Typically, identical polarizations $\vec{w}$ are selected for the acquisitions from both ends of the baseline. The polarization dependent coherence becomes then

$$\gamma(\vec{w}) = \frac{\langle s_1(\vec{w}) s_2^*(\vec{w}) \rangle}{\sqrt{\langle s_1(\vec{w}) s_1^*(\vec{w}) \rangle \langle s_2(\vec{w}) s_2^*(\vec{w}) \rangle}}. \tag{12}$$

The polarization states $\vec{w}$ used in this thesis correspond mostly to the lexicographic polarizations HH, VV, and HV.

Originally, Pol-InSAR techniques were established for forest applications, with the well-known Random-Volume-over-Ground model [36]. This model describes the scattering from the tree canopy as volume scattering from randomly orientated particles, and polarizing surface scattering from the ground below. Geophysical properties of forests, e.g. forest height, are then derived by the selection or optimization of polarization states that maximize the volume and the ground contributions [25], [37], and by modeling the vertical backscattering distribution with, e.g., an exponential function [37]. The demonstration of Pol-InSAR for the assessment of the vertical structure of different scattering mechanisms, particularly in the context of natural scattering volumes, indicates its potential for ice sheet subsurface applications.

The polarimetric properties of backscattering from snow, firn, and ice are still not fully understood and the backscattering contributions from different type of scatterers, e.g. the surface, ice layers, or the firn volume cannot be as clearly separated by different polarizations, as for instance the scattering from the ground and the tree canopy in a forest scenario. Still, the polarimetric observation space adds valuable information to the measurements over ice sheets. For the scope of this thesis, the main interest is to understand the differences in the vertical backscattering distributions of different polarizations and their effect on the coherence, through the volume decorrelation γ_{vol}. Existing Pol-InSAR approaches for ice sheet monitoring are reported in Section 1.4.3.

1.2.4 SAR TOMOGRAPHY

Instead of relying on models to link Pol-InSAR measurements to vertical backscattering distributions of volumes, *SAR tomography* allows estimating vertical profiles of the backscattering in each resolution cell, which essentially provides 3-D imaging capabilities. This was first demonstrated with airborne SAR data in [26]. Although the application of SAR tomography for glaciers and ice sheets is quite new and only a few studies have been published, the potential to estimate the 3-D backscattered power in the subsurface was demonstrated [38], [39]. Several acquisitions of the same scene on the ground, from different flight tracks separated by multiple baselines, are employed to achieve resolution in the vertical direction. Spectral estimators (overview in [40] and [41]) are then used to estimate the 3-D backscattered power from the multi-baseline interferometric coherences. There are model-based algorithms, which employ certain assumptions about the scattering properties to derive the vertical profiles. One example is MUSIC [42], which addresses the localization of multiple sources, which are assumed to be point-like. This can be useful for the detection of distinct subsurface layers, but is not applicable to vertically distributed volume scattering. Another group of tomographic approaches are model-free algorithms that estimate the 3-D scattering without assumptions on the scattering. This has the advantage of less constrained results, which is particularly important for scattering media where the modeling of the scattering distribution is not yet established. The most commonly used model-free algorithms are Fourier beamforming and Capon beamforming [40], [41]. They directly invert the Fourier relationship, cf. eq. (11), between the multi-baseline measurements and the vertical backscattering profile. In the frame of this thesis, Capon beamforming is chosen to estimate the subsurface scattering distribution from ice sheets, due to its enhanced vertical resolution, as well as improved side lobe and ambiguity suppression.

The estimation of the vertical backscattering distributions with SAR tomography in the subsurface of ice sheets at different polarizations and frequencies provides essential insights for improving the modeling for Pol-InSAR applications.

1.2.5 THE RELATIONSHIP OF ONE-WAY PENETRATION DEPTH, EXTINCTION, PHASE CENTER, AND PENETRATION BIAS

This section clarifies the terms one-way and two-way penetration depth, extinction, phase center depth, and penetration bias.

The *one-way penetration depth* d_{pen} is the depth at which the signal power in the subsurface drops to $1/e$ (about 37%) of its original value at the surface [51]. The *two-way penetration depth* is by a factor of two smaller, considering the signal travel path into the subsurface as well as the way backwards after scattering. The penetration depth can be seen as a material property of the scattering medium and is defined as a distance normal to the surface. It is related to the signal *extinction coefficient* κ_e through $\kappa_e = cos(\theta_r)/d_{pen}$. In this sense, the extinction κ_e, typically given in dB/m, is an "extinction-length" in the direction defined by the refracted incidence angle, and describes the rate at which the signal intensity reduces [51].

The interferometric *phase center* $\angle\gamma$ corresponds to the phase of the complex coherence measured with an InSAR system. The phase center is converted to meters by $\angle\gamma/k_{zVol}$, if it is located in the subsurface.

The *penetration bias* of surface elevations measured with InSAR is the difference between the phase center location in the subsurface and the actual surface. This is equivalent to the *phase center depth*, which is calculated by $(\angle e^{ik_z z_0} - \angle\gamma)/k_{zVol}$.

Assuming constant signal extinction along depth, the vertical backscattering distribution has an exponential shape. In this case, the phase center depth is equal to the two-way penetration depth. Strictly speaking, this requires an interferometric acquisition geometry with a small enough k_{zVol}, respectively a large enough HoA, so that all scattering contributions in the subsurface are within one 2π-phase-interval [17]. This is further addressed in Chapter 4.

1.3 THE SUBSURFACE OF ICE SHEETS

This section briefly introduces the main glaciological concepts for the subsurface of ice sheets, focusing on the relevant aspects that influence the subsurface scattering characteristics. Only the first several tens of meters below the surface are of interest, being within the penetration capability of typical SAR frequencies and imaging geometries under dry and frozen conditions.

The Greenland ice sheet is the second largest ice body on Earth, covering about 1,700,000 km² and its surface elevation ranges from sea level up to 3,200 m a. s. l. This leads to a large variety of climatic conditions which affect surface and subsurface processes. Temperature differences influence the length and intensity of melting periods. Similarly, accumulation rates differ across the ice sheet. Accumulation, ablation, and metamorphism processes, which are not described to their full extent here, influence the geophysical properties of the subsurface. This was summarized in the concept of *glacier zones* by Benson [43], which is sketched in Fig. 3. The subsurface characteristics, which are relevant for microwave scattering, can be well addressed in the glacier zone framework.

The *dry snow zone*, at the uppermost elevations, is characterized by the absence of snow melt [44]. Here, the accumulating snow turns into several tens of meters thick firn, which is gradually densifying with depth until it becomes glacier ice. The absence of melt leads to lower densities of the firn compared to other glacier zones. A rare exception to this occurred in 2012, when a very short melt event was observed even at the summit of Greenland, which lead to a 2-cm refrozen ice crust [45]. The dry snow zone is characterized by low backscatter in SAR images, since the (only) source of scattering are the snow and firn grains, which are small compared to the microwave wavelength [46].

In the *percolation zone*, melting occurs regularly during summer. The meltwater percolates from the surface into the snow and firn and refreezes. The resulting ice inclusions appear in the form of layers and lenses, oriented parallel to the surface, if a relatively impermeable layer causes a lateral spread of the percolating water [43], [44]. Also refrozen pipes form as residues

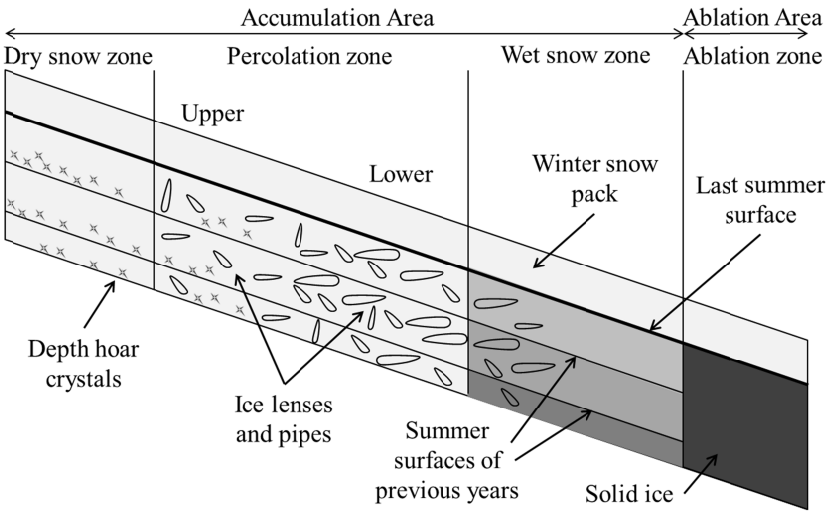

Fig. 3. A sketch of the subsurface characteristics of the glacier zones in Greenland from [48] modified after [43].

of the downward percolation. The size of the ice inclusions is between few cm and 1 m, which makes them strong scatterers at microwave wavelengths [46], [47]. The gradient of increased melting from higher to lower elevations leads to increased presence of refrozen melt features in the lower percolation zone compared to its upper part. This can be also recognized by increased SAR backscatter in the lower percolation zone [48].

The *wet snow zone*, below the percolation zone, experiences the same processes, but the further increased melting and temperatures lead to the fact that the entire winter snow pack is wet by the end of the summer. At this point, the snow accumulation of one year is raised to 0°C temperature, where also the large latent heat intake due to refreezing of melt water plays an important role [44]. This zone has similar scattering characteristics as the lower percolation zone if all melt water is refrozen [49]. At the lower end of the wet snow zone, the entire snow pack is melted at the end of summer and the melt water refreezes in new layers of superimposed ice on top of the older glacier ice. This area is called *superimposed ice zone* [44].

All glacier zones described above belong to the accumulation area, where the ice sheet gains mass from year to year. At lower elevations, melting of the entire winter accumulation and the ice below leads to a net mass loss in the so called *ablation zone*, which therefore has a bare ice surface in summer. The scattering from the ablation zone can be dominated by the sometimes very rough surface, particularly in crevasse fields or due to features related to glacier flow. With respect to microwave penetration, the glacier ice in the ablation zone can be quite homogeneous, which can lead to relatively deep penetration [20]. But also very heterogeneous subsurface scattering structures have been found with strong variations in penetration, which are not yet fully understood [50]. The accumulation area, with a positive surface mass balance, and the ablation area, with a negative surface mass balance, are separated by the equilibrium line.

The geophysical properties of the subsurface described in this section affect the SAR measurements only under dry and frozen conditions, when the low permittivity values of snow, firn, and ice favor the penetration of microwave signals. In contrast, if liquid water is present the

dielectric properties change significantly and prevent the penetration of microwaves. Already a volumetric moisture content of 2% decreases the penetration by a factor of 100 [51]. In this case, the SAR measurements become mainly sensitive to the surface properties. A wet ice sheet surface leads to higher backscatter values in areas with larger surface roughness, like the ablation zone, and to lower backscatter values in the accumulation area [46], [49], due to the smoother surface. However, addressing the modeling of subsurface scattering, this thesis focusses on SAR measurements in dry and frozen conditions.

Current approaches to investigate subsurface properties of ice sheets comprise for instance in situ measurements in the form of snow pits [52] and firn cores [53], [54], as well as remote sensing methods like ground-based and airborne radar sounders [55], [56], [57]. These methods can provide a high level of detail about the geophysical properties, e.g., density, refreezing processes, and stratigraphy information, but only as isolated point-like measurements or along transects. Therefore, they are limited in their spatial coverage and resolution. Similarly, due to the campaign-based nature of such measurements, they are also limited in terms of temporal sampling. This highlights the benefit of investigating Pol-InSAR approaches, because of the potential to provide geophysical subsurface information of entire ice sheets on a monthly basis with few tens of meters spatial resolution with the next generation of SAR missions [16].

1.4 State of the Art of SAR for Ice Sheet Subsurface Monitoring

Pol-InSAR techniques and their application to glaciers and ice sheets are still at an early research stage and only few studies are reported. This chapter gives a brief review on monitoring of ice sheets and glaciers with SAR, PolSAR, InSAR, Pol-InSAR, and SAR tomography, focusing on aspects related to subsurface scattering. Satellite based studies for monitoring glaciers and ice sheets with SAR backscatter are dating back to the Seasat mission, which was launched in 1978. The availability of polarimetric and interferometric SAR data through, e.g., the SRTM mission, the ERS satellites, or ENVISAT, fostered many PolSAR and InSAR studies. In contrast, only few Pol-InSAR and SAR tomography studies over ice sheets exist, because suitable data sets are only available from airborne platforms.

Early studies based on *SAR backscatter intensities* revealed the potential to discriminate different snow and ice surfaces [58] as well as glacier zones [46]. The dependence of the backscattering on the subsurface properties, like the presence of ice inclusions formed by refrozen melt water, was already highlighted [46]. The relationship between backscatter intensities and subsurface properties was also used in early studies to estimate accumulation rates [59], [60].

1.4.1 SAR Polarimetry

The next major step was the use of fully *polarimetric measurements* by means of PolSAR over glaciers and ice sheets [61], [62]. These studies revealed interesting polarimetric properties of the different glacier zones, namely the relatively strong cross-polarized backscatter from

volume scattering in the subsurface. Additionally, the complementary information content of measurements at different radar frequencies, which are sensitive to different scattering processes and sizes of scatterers, was pointed out. Based on these results, first polarimetric models described the main scattering contributions from ice lenses and pipes in the percolation zone of the Greenland ice sheet as scattering from horizontally and vertically oriented cylinders [63]. Polarimetric modeling advanced to a combination of rough surface scattering and volume scattering from dipoles [64] or spheroidal particles [65] to interpret PolSAR data from an ice cap in Svalbard. Also anisotropic propagation effects where introduced into polarimetric modeling in [65]. However, PolSAR measurements contain no information about the location and vertical distribution of scatterers in the subsurface of glaciers and ice sheets.

1.4.2 SAR INTERFEROMETRY

The vertical location of the scattering phase center can be measured with *InSAR*, which is widely used to derive surface elevations of glaciers (see Section 1.1). Another application of InSAR is to study the subsurface of ice sheets by employing the dependence of interferometric measurements on the vertical distribution of backscattering through volume decorrelation, which is the core of this thesis. By modeling the subsurface as a homogeneous, lossy, and infinitely deep scattering volume, a relation between InSAR coherence magnitudes and the rate of extinction of the microwave signals in the subsurface of ice sheets was established in [66]. This approach allows the estimation of the signal extinction parameter, which is inversely related to signal penetration depth, given the model assumptions. Note that this penetration depth is a model parameter and not the actual depth of the interferometric phase center. This concept of a homogeneous subsurface volume implies a uniform signal extinction with depth. Therefore, the model from [66] is called *Uniform Volume (UV) model* throughout this thesis. Note that the uniform extinction leads to a vertical distribution of backscattered power in the form of an exponential function. The extinction parameter, respectively the penetration depth, of the UV model can be seen as a first, yet simplified, indicator of subsurface properties, which differ across an ice sheet. This is used in recent studies for the classification and characterization of glacier zones in ice sheets with InSAR data [48].

Another approach based on coherence magnitudes was to estimate accumulation rates at C-band with physical snow scattering models [67], which account for rough surface scattering contributions at hoar layer interfaces and use the improved Born approximation [68] for volume scattering. Even if the study was hampered by a long time difference between the SAR measurements and validation data, it indicated the potential to analyze layered firn with InSAR. The same scattering models were discussed in [69] to assess Ka-band penetration. These models describe the geophysical subsurface properties in more detail with the drawback of relying on extensive a priori information and assumptions about grain size, density, temperature, and interface roughness.

The aforementioned penetration depth parameter of the UV model is a property of the medium indicating where the signal power drops to $1/e$, and can be derived solely based on

coherence magnitudes [66]. However, approaches based on the UV model may not adequately capture different scattering scenarios that occur within ice sheets because they are limited by the assumption of a constant signal extinction along depth. The signal penetration can be also directly measured by taking the difference between the interferometric phase center and the surface elevation. The dependence of this phase center depth on different snow, firn, and ice conditions was described in [20]. This phase center depth describes the penetration bias of InSAR digital elevation models, as mentioned in Section 1.1. However, measured phase centers were reported to be deeper than the penetration depth predicted by a UV model [70]. Furthermore, for a UV model, the measured phase center cannot be deeper than a quarter of the height of ambiguity, because of the way the measured phase depends on the interferometric baseline for a UV model [17]. The discrepancy between UV model penetration depth and InSAR phase center depth motivates the use of non-uniform volume models. This was introduced in [70] by allowing an increasing extinction with depth proportional to the increase of density in ice sheets. However, unrealistic density profiles were necessary to match the data, which indicated the need for further improvements in interferometric modeling of ice sheet subsurface scattering.

1.4.3 POLARIMETRIC SAR INTERFEROMETRY

Based on PolSAR and InSAR techniques, the next development was the coherent combination of SAR data separated by a spatial baseline and acquired at different polarizations by means of *polarimetric SAR interferometry (Pol-InSAR)*, which is today a well-established remote sensing discipline. In particular, the successful retrieval of vertical structure parameters by means of Pol-InSAR [71] and the generation of related biophysical products demonstrated the performance of this approach. Despite this, only few studies have assessed the potential of Pol-InSAR to retrieve geophysical information from glaciers and ice sheets. The retrieval of signal extinction with Pol-InSAR at L- and P-band over an ice cap in Svalbard was shown in [31], by the combination of a UV model with a surface scattering component, also known as Random-Volume-under-Ground (RVuG) model. The approach employed a polarimetric decomposition to separate surface contributions from subsurface volume scattering, which was then parameterized by a constant extinction coefficient (UV model). A similar formulation with not only a surface contribution on top of a UV, but also a boundary below the volume, in the sense of a snow-firn interface, was used in [69] to describe Ka-band penetration into the snow cover at Greenland's summit. It was also demonstrated that the dissimilar subsurface structures of different glacier zones have a clearly separable effect on the measured Pol-InSAR coherences [72]. Despite these findings, gaps in the interpretation of Pol-InSAR signatures from snow and ice remain so that existing Pol-InSAR models often cannot interpret the measurements [70], [72], [73]. The main limitation is the assumption of a constant extinction along depth, which can be insufficient to capture different scattering scenarios that occur within ice sheets. Additionally, the discrepancy between model-based penetration depth and measured interferometric phase center depth exists also in the Pol-InSAR context.

1.4.4 SAR TOMOGRAPHY

In recent studies multi-baseline data was exploited for *SAR tomography* to estimate 3-D backscattered power. The imaging of subsurface features in snow [74], lake and fjord ice [75], glaciers [38], and ice sheets [39], [50] was demonstrated. Depending on the study, the effect of subsurface layers, firn bodies, crevasses, and the bed rock was recognized in the profiles derived with SAR tomography. This verified that the subsurface of glaciers and ice sheets can have a more complex backscattering structure than what is accounted for in existing models. SAR tomography can therefore play a major role for investigating and improving subsurface scattering modeling of ice sheets.

1.5 THE ARCTIC15 CAMPAIGN

The SAR data from the ARCTIC15 campaign in Greenland in 2015 is the foundation of the research conducted in this thesis. It provides an exceptional test bed of polarimetric multi-baseline interferometric SAR measurements at different frequencies. In particular, the multi-baseline data acquired from several parallel airborne tracks is a huge asset for the research objectives of this thesis and is currently not available from satellite sensors. The combination of a unique SAR data set with coordinated in situ measurements and external reference data provides the basis for model development and validation for new approaches in the frame of PolSAR, Pol-InSAR, and SAR tomography related to ice sheet surface and subsurface properties.

A large number of people were involved in the campaign and I cannot value their work highly enough.

The author's contributions:

- Scientific planning of the test sites and scientific coordination of the ARCTIC15 campaign and participation in the ground activities (corner reflectors, GNSS and accumulation probe measurements, GPR data).
- Acquisition, processing, and analysis of the GPR data.
- Involved in the debugging and calibration process of the F-SAR data and conducted several iterations of reprocessing, using the SAR processor written by the F-SAR processing group at DLR.
- Polarimetric, interferometric, and tomographic processing and analysis of the SAR data.

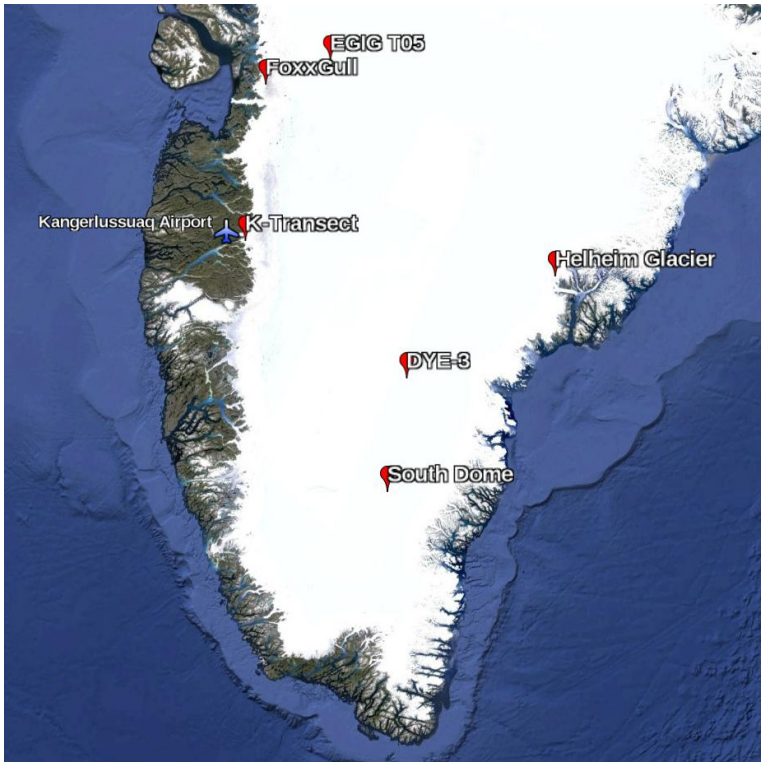

Fig. 4. Overview of the land ice test site locations in the southern part of Greenland. © Google Earth

Contributions of the ARCTIC15 campaign team:

- Prof. Dr. Irena Hajnsek (DLR, ETH Zurich) initiated the campaign and was the principle investigator, contributing to all planning and coordination steps.
- Ralf Horn (F-SAR coordinator), Martin Keller, and the team at DLR's flight experiments facility carried out the operational planning and the logistics of the campaign.
- Dr. Matteo Pardini (DLR) calculated the baselines to optimize the tomographic imaging.
- Martin Keller (DLR) and Dr. Silvan Leinss (ETH Zurich) were in charge of the installation of the corner reflectors and the acquisition of the GNSS data during the ground activities. The work on the ground (corner reflectors, GNSS and accumulation probe measurements, GPR data) was carried out in concerted teamwork of the two and myself.
- Ralf Horn, Daniel Geßwein, and the team of DLR's flight experiments facility (pilots and airplane engineer) conducted the airborne F-SAR acquisitions. Martin Keller processed the first data quality checks on site.
- The F-SAR processing group of DLR (Dr. Rolf Scheiber, Marc Jäger, and Jens Fischer) was responsible for the SAR processing until coregistered SLC data level, including the multi-baseline interferometric phase calibration.

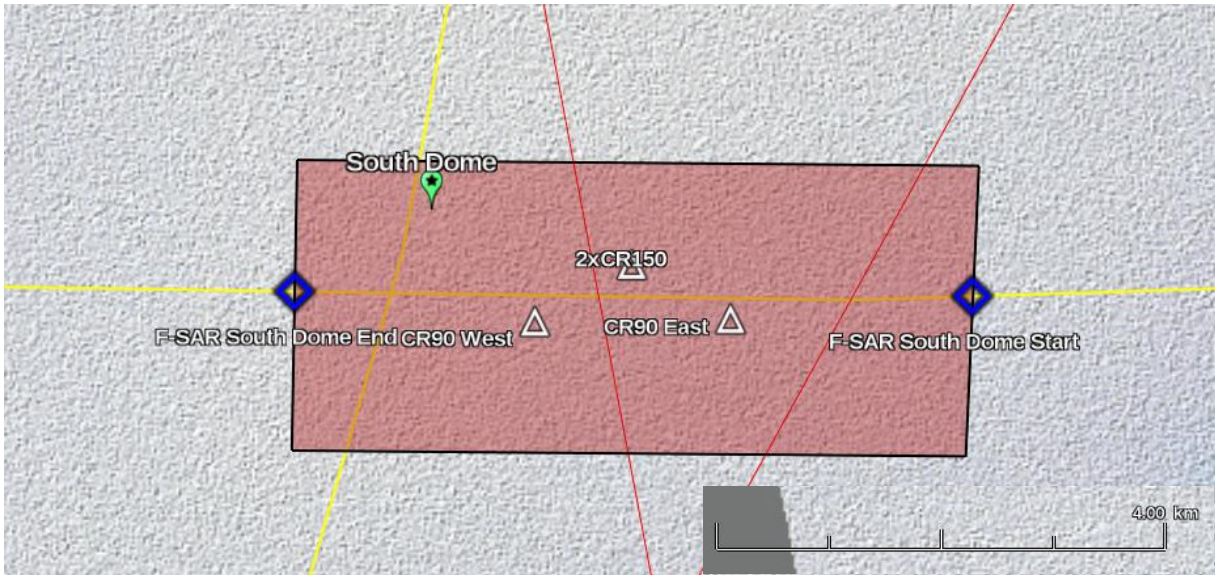

Fig. 5. South Dome test site planning overview with F-SAR coverage and corner reflector locations. Yellow lines: AWI Accumulation Radar 2012; Red lines: IceBridge flight planning 2015; Background: TanDEM-X DEM.

The airborne SAR dataset was acquired with DLR's F-SAR system in Greenland during April and May 2015. The goal of the ARCTIC15 campaign was to acquire fully polarimetric multi-baseline datasets, which are suitable for Pol-InSAR and SAR tomography, in five different microwave frequency bands over a range of different glacier zones in Greenland. Seven test sites on the ice sheet (see Fig. 4), mainly in the percolation and ablation zone, as well as one sea ice test site were covered. Unfortunately, the dry snow zone could not be accessed due to the limited flight endurance. The standard acquisition concept for the ice sheet test sites was a quad-pol configuration in X-, C-, L-, and P-bands from one heading and X-, S-, L-, and P-bands from the opposite direction in a multi-baseline setup with 7 - 9 tracks per heading. This concept was not always achieved due to flight endurance or technical limitations.

The airborne SAR acquisitions were coordinated with ground activities conducted by DLR and ETH Zurich. These are comprised of GPR and GNSS tracks, accumulation probe measurements and the placement of corner reflectors. Additionally, the test sites where defined in a way to maximize synergies with valuable external datasets and campaigns. These include NASA IceBridge data [56], CryoVex campaigns [76], AWI Accumulation Radar [57], AWI firn cores [53], temperature bore holes [54], surface mass balance measurements [77], as well as PROMICE [78] and GC-Net [79] weather stations. An example for the alignment of F-SAR coverage, the ground activities, and external data is provided in Fig. 5. Table I summarizes all available data sets comprising seven land ice and one sea ice test site.

The baselines for the heading with the X-, S-, and L-band acquisitions were optimized for L-band. The nominal setup comprised baselines separated by -35 m, -30 m, -25 m, -20 m, 0 m, 20 m, 40 m, and 55 m from the reference track flown at 3000 m above ground. This corresponds to nominal k_z values at mid-range of 1.3 rad/m for the largest baseline and 0.07 rad/m for the shortest baseline at L-band. This results in a nominal vertical resolution for SAR tomography of about 5 m at mid-range at L-band. The non-ambiguous height is about 90 m. These values are

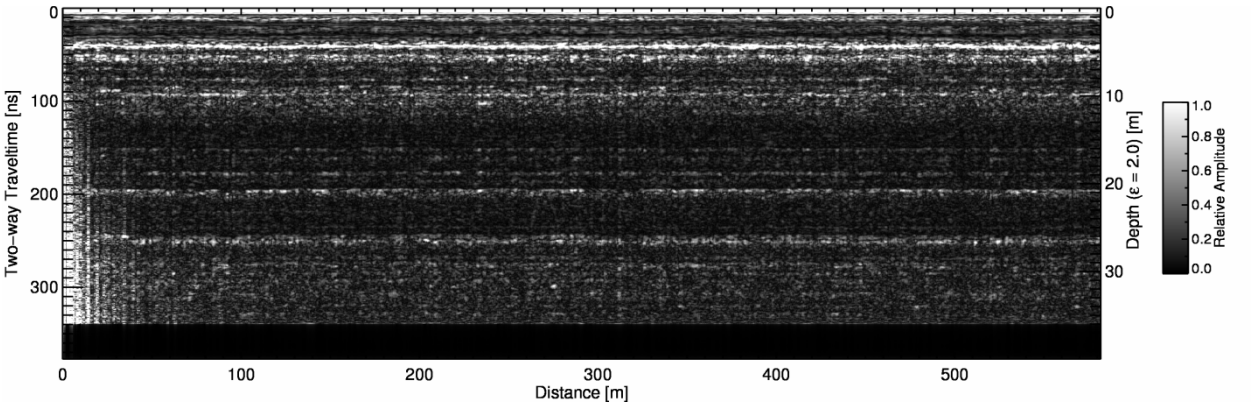

Fig. 6. Amplitude envelope of a GPR transect at South Dome. Distinct layers are visible. The deepest section of approximately 35-40 m is removed due to filter artefacts and low signal-to-noise ratio. At the left side, at the start of the GPR transects, artefacts are visible which are related to the presence of the Twin Otter aircraft, which was used to access the test sites.

by a factor of 2.5 and 7.4 smaller for S- and X-band, respectively. The opposite heading with the X-, C-, and L-band acquisitions was optimized for C-band with horizontal baselines separated by -15 m, -10 m, -5 m, 0 m, 5 m, 10 m, 15 m, and 20 m from the reference track. This corresponds to nominal k_z values at mid-range of 1.7 rad/m for the largest baseline and 0.3 rad/m for the shortest baseline at C-band, resulting in a vertical resolution of 3.8 m and a non-ambiguous height of 22.7 m. These values are 4 times larger at L-band and 1.8 times smaller at X-band for this heading. The P-band data was acquired during separate flights and both headings had the same baselines with a nominal spatial separation of -105 m, -90 m, -75 m, -65 m, 0 m, 60 m, 120 m, and 165 m from the reference track. This leads to maximum and minimum k_z values at mid-range of 1.2 rad/m and 0.04 rad/m, providing a vertical resolution of 5 m and a non-ambiguous height of 140 m. The baselines at each test site can deviate slightly from this nominal acquisition concept.

Advanced SAR processing is implemented for the F-SAR system, comprising SAR focusing and motion compensation algorithms that can account for the movement of the airborne platform. This includes the navigation and attitude data from the airplane as well as range and topography dependent motion compensation algorithms based on multi-squint approaches. Further steps include antenna pattern correction and the radiometric calibration. Multi-baseline interferometric phase calibration was also an essential factor to achieve good tomographic 3-D imaging quality. More details on the F-SAR processing can be found in [80] and [81].

Corner reflectors were installed at all test sites on the ice sheet, except FoxxGull, and are used as a surface reference for the interferometric phase measurements. They were placed prior to the F-SAR flights and fixed into the firn with anchors. The larger 1.50 m reflectors were located right next to the predefined landing spot at each test site. The 90 cm reflectors were transported on site with a sledge, therefore their spatial separation between few hundred meters and 1 km depended on the weather and snow conditions during installation.

GNSS surface coordinates where acquired along the triangle that follows the positions of the corner reflectors (example in Fig. 5). They provide precise surface reference for comparison

Fig. 7. Accumulation probe measurements for the detection of hard layers in the subsurface. One 90 cm corner reflector is visible on the sledge on the left as well as the GPR system on the right.

with InSAR elevations and GNSS information for the GPR measurements. A base station was established next to the 150 cm reflectors and the GNSS surface tracks were acquired in real time kinematic (RTK) mode. A second base station was used to average GNSS positions during the entire stay at each test site (approx. 4-5 h) in order to have a GNSS reference station, because real reference stations are scarce and far away in Greenland. This second station was then post-processed with Precise Point Positioning (PPP) and considered the "true" position. By cross-validation of the PPP processed true base station with the base station of the RTK measurements, a constant correction offset for the RTK surface tracks was derived and applied to the measurements. The final surface GNSS tracks have an accuracy in the centimeter range.

GPR data was acquired along the same triangle as the surface GNSS tracks with a system provided by the Alfred-Wegener-Institute. In most cases a 500 MHz antenna was used with a receive time window corresponding to about 40 m depth. A measuring wheel ensured a spatially homogeneous sampling every 0.25 m. The center wavelength in firn ($\epsilon_r = 2.0$) is approximately 0.42 m. The theoretical vertical depth resolution is about 0.21 m. One example from the South Dome test site is given in Fig. 6, which highlights the subsurface layers present in the upper percolation zone. The following processing steps for the GPR data were implemented according to [82]. Direct current removal: Correction for the mean offset of the direct current level; Time zero correction: To ensure that the first sample corresponds to the direct wave between transmit and receive antenna; Bandpass filtering: SNR enhancement was performed with a Butterworth bandpass filter; Time gain: A combination of an energy decay gain, to compensate for the range spread losses, and a user-defined linear and exponential gain function was applied to make the visualization of layers at all depths possible.

Since the GPR tracks were acquired without a GNSS receiver, it was necessary to link the GPR tracks to the GNSS surface tracks in post processing steps. Both GPR and GNSS measurements were taken along the same path between the corner reflectors at each test site,

therefore the GNSS tracks can be directly used for the GPR data. The GNSS coordinates are considered to be within $\pm$ 10 m of the GPR tracks.

A snow accumulation probe was used to detect refrozen melt layers in the subsurface. This was conducted by thrusting the accumulation probe vertically into the snow and registering a hard layer depending on the force necessary to penetrate further (see Fig. 7). An example for the layer detections is shown in Fig. 3 in Chapter 2. Due to the manual and subjective nature of the approach, the measurements have to be considered carefully. Some layers were not permeable, making it impossible to detect further deeper layers. Thinner or weaker layers were sometimes undetected. To improve these reliability issues, up to five measurements were conducted around each corner reflector in an area with about 5 m radius.

The following Table I summarizes all test sites of the ARCTIC15 campaign.

TABLE I
SUMMARY OF THE TEST SITES OF THE ARCTIC15 CAMPAIGN

Test Sites 1-3	South Dome	EGIG T05	Dye-3
Number of headings	2	2	1
Frequency bands heading1	X-S-L-P with 7 tracks	X-S-L-P with 9 tracks	X-S-L-P with 8 tracks
Frequency bands heading2	X-C-L-P with 7 tracks	X-C-L-P with 9 tracks	-
Heading1 horiz. baselines [m] X-S-L-band	-35, -30, -20, 0, 20, 40, 55	-35, -30, -25, -20, 0, 20, 30, 40, 55	-35, -30, -25, -20, 0, 20, 40, 55
Heading2 horiz. baselines [m] X-C-L-band	-15, -10, -5, 0, 5, 15, 20	-20, -15, -10, -5, 0, 5, 10, 15, 20	-
Heading1&2 horiz. baselines [m] P-band	-105, -90, -75, -65, 0, 60, 165	-105, -90, -75, -65, 0, 60, 90, 120, 165	-105, -90, -75, -65, 0, 60, 120, 165
Flight altitude above ground	3000 m	3000 m	3000 m
Center Coordinate	44.5306°W, 63.5266°N	47.1291°W, 69.8695°N	43.8863°W, 65.1836°N
Scene Length:	6 km	11 km	7 km
Scene Width:	3 km	3 km	3 km
External Data	NASA IceBridge, GC-Net weather station, AWI firn cores (2012), AWI radar echo sounding (2012)	ESA CryoVex campaigns, NASA IceBridge, GC-Net weather station, AWI radar echo sounding (2012)	NASA IceBridge, AWI firn cores (2012), AWI radar echo sounding (2012)
Glacier Zone	Percolation Zone	Percolation Zone	Percolation Zone
Corner Reflectors	2 x 150 cm, 2 x 90 cm	2 x 150 cm, 2 x 90 cm	1 x 150 cm, 2 x 90 cm
GPR data	Ca. 3 km with 500 MHz	Ca. 2 km with 500 MHz	Ca. 1.5 km with 500 MHz
Accumulation probe	Hard layer detection	Hard layer detection	Hard layer detection

TABLE I - CONTINUED
SUMMARY OF THE TEST SITES OF THE ARCTIC15 CAMPAIGN

Test Sites 4-6	K-Transect	Helheim Glacier	K_Transect_long
Number of headings	2	2	2
Frequency bands heading1	X-S-L-P with 8 tracks	X-S-L with 2 tracks	X-S-L with 1 track
Frequency bands heading2	X-C-L-P with 8 tracks	X-C-L with 1 track	X-C-L with 1 track
Heading1 horiz. baselines [m] X-S-L-band	-35, -30, -25, -20, 0, 20, 40, 55	0, 55	1 track
Heading2 horiz. baselines [m] X-C-L-band	-15, -10, -5, 0, 5, 10, 15, 20	1 track	1 track
Heading1&2 horiz. baselines [m] P-band	-105, -90, -75, -65, 0, 60, 120, 165	-	-
Flight altitude above ground	3000 m	3000 m	3000 m
Center Coordinate	49.9717°W, 67.0978°N	38.3884°W, 66.5758°N	47.9581°W, 67.0304°N
Scene Length:	26 km	26 km	200 km
Scene Width:	3 km	3 km	3 km
External Data	NASA IceBridge, PROMICE weather stations, yearly surface mass balance	NASA IceBridge, TanDEM-X Dual Pol super test site	NASA IceBridge, PROMICE weather stations, yearly surface mass balance
Glacier Zone	Ablation Zone	Transition from Percolation to Ablation Zone	Transition from Percolation to Ablation Zone
Corner Reflectors	2x 150 cm, 2 x 90 cm	2x 150 cm, 2 x 90 cm	-
GPR data	-	Ca. 1.5 km with 500 MHz	-
Accumulation probe	-	Hard layer detection	-

TABLE I - CONTINUED
SUMMARY OF THE TEST SITES OF THE ARCTIC15 CAMPAIGN

Test Sites 7-8	FoxxGull	Sea Ice
Number of headings	2	2
Frequency bands heading1	X-S-L with 7 tracks	X-S-L with 1 track
Frequency bands heading2	X-C-L with 7 tracks	X-S-L with 1 track
Heading1 horiz. baselines [m] X-C-L-band	-35, -30, -20, 0, 20, 40, 55	1 track
Heading2 horiz. baselines [m] X-S-L-band	-15, -10, -5, 0, 5, 15, 20	1 track
Heading1&2 horiz. baselines [m] P-band	-	-
Flight altitude above ground	3000 m	3000 m
Center Coordinate	49.7996°W, 69.4492°N	57.9512°W, 67.6845°N
Scene Length:	8.5 km	200 km
Scene Width:	3 km	3 km
External Data	ETH Zurich bore holes	-
Glacier Zone	Ablation Zone	Transition from open water to sea ice
Corner Reflectors	-	-
GPR data	-	-
Accumulation probe	-	-

1.6 RESEARCH OBJECTIVES AND SCOPE OF THE THESIS

The main objective of this thesis is to improve the modeling of the effect of subsurface scattering from ice sheets on polarimetric interferometric SAR measurements. The key aspect is the vertical backscattering distribution in the subsurface, because it directly determines the measured interferometric coherences through volume decorrelation, as described in Section 1.2.2. This contributes not only to an improved understanding of Pol-InSAR measurements from ice sheets, but lays the modeling foundation for future applications. The modeling efforts are targeted towards the estimation of the penetration bias in DEMs acquired with InSAR and the potential to retrieve geophysical subsurface information from SAR data, as described in Section 1.1. However, further applications are possible, for instance in performance studies for future SAR missions. While the application of a penetration bias correction is investigated, the relationship to geophysical information and its retrieval goes beyond the scope of this thesis, yet benefits from the presented model improvements. The goal is to derive models which accurately reproduce the measurements, minimize the need of a priori information, and are simple enough to allow model inversions for the development of potential applications.

The thesis is based on airborne SAR data acquired during the ARCTIC15 campaign focusing on the South Dome and EGIG T05 test sites in the percolation zone. These two test sites were chosen due to the interesting circumstance of being within the same glacier zone but having different subsurface structures.

The main objective of this thesis is to improve the modeling of the vertical backscattering distribution in the subsurface of ice sheets and its effect on polarimetric interferometric SAR measurements. This leads to the following specific research questions, some of which were also triggered by the particularities found in the ARCTIC15 data:

- Can different subsurface structures be recognized in InSAR, Pol-InSAR, and SAR tomography measurements?
- Are different polarizations and frequencies providing additional information content?
- Are existing models accurate enough to describe the effect of the vertical backscattering distribution in the subsurface of ice sheets on InSAR data?
- To what extent are the investigated models applicable to different areas, frequencies, and polarizations?
- Is the vertical backscattering distribution in the subsurface of ice sheets polarization dependent and to which extent does this have to be considered in the modeling?
- Do the investigated models provide a link to the geophysical subsurface properties?

- Can the models be used to estimate the penetration bias in InSAR surface elevation measurements (DEMs) and how accurate is the estimation?

1.7 Organization of the Thesis

In Chapter 1, the motivation and problem statement, a brief summary of the fundamentals of SAR techniques and ice sheet subsurface, as well as the state of the art are described, followed by the research objectives. They are addressed in the following three chapters of this thesis, consisting of published, accepted, and submitted papers. Each of these chapters can be read and understood separately.

Chapter 2 "*Modeling Multifrequency Pol-InSAR Data From the Percolation Zone of the Greenland Ice Sheet*" addresses the effect of distinct refrozen melt layers in the subsurface on interferometric measurements. A multiple layer plus volume model is introduced to interpret the effects of such subsurface layers. This improved model is able to describe the interesting coherence undulation in the InSAR data. It allows the characterization of the subsurface layers from the InSAR measurements at different polarizations and frequencies. The derived distances between the layers are validated with GPR measurements.

In Chapter 3 "*Modeling the Vertical Backscattering Distribution in the Percolation Zone of the Greenland Ice Sheet with SAR Tomography*" the investigation of different model parameterizations of the vertical backscattering distribution is described. Here the focus is on the volume component, either in the background behind the layers or in the case where no layers are present. The model results are compared to vertical backscattering distributions derived with SAR tomography, showing improved performance with respect to existing models and indicating the generalizability across test sites, polarizations, and frequencies.

Chapter 4 "*Modeling and Compensation of the Penetration Bias in InSAR DEMs of Ice Sheets at Different Frequencies*" covers the correction of the penetration bias in InSAR ice sheet surface elevation measurements with interferometric models based on the results of Chapter 3. The baseline dependence of the penetration bias is modeled and validated, and a novel phase center depth retrieval is introduced. The accuracy of the penetration bias estimates is quantitatively assessed by comparison with GNSS measurements.

Chapter 5 summarizes the conclusions of this thesis and provides answers to the research questions. The resulting implications are described.

1.8 REFERENCES

[1] D.G. Vaughan, J.C. Comiso, I. Allison, J. Carrasco, G. Kaser, R. Kwok, P. Mote, T. Murray, F. Paul, J. Ren, E. Rignot, O. Solomina, K. Steffen, and T. Zhang, "Observations: Cryosphere," in *Climate Change 2013: The Physical Science Basis. Contribution of Working Group I to the Fifth Assessment Report of the Intergovernmental Panel on Climate Change,* [Stocker, T.F., D. Qin, G.-K. Plattner, M. Tignor, S.K. Allen, J. Boschung, A. Nauels, Y. Xia, V. Bex and P.M. Midgley (eds.)]. Cambridge University Press, Cambridge, United Kingdom and New York, USA, 2013.

[2] M. Meredith, M. Sommerkorn, S. Cassotta, C. Derksen, A. Ekaykin, A. Hollowed, G. Kofinas, A. Mackintosh, J. Melbourne-Thomas, M. M. C. Muelbert, G. Ottersen, H. Pritchard, and E. A. G. Schuur, "Chapter 3: Polar Regions," in *IPCC Special Report on the Ocean and Cryosphere in a Changing Climate,* [H.-O. Pörtner, D.C. Roberts, V. Masson-Delmotte, P. Zhai, M. Tignor, E. Poloczanska, K. Mintenbeck, M. Nicolai, A. Okem, J. Petzold, B. Rama, N. Weyer (eds.)]. In press, 2019.

[3] J. L. Bamber, R. M. Westaway, B. Marzeion, and B. Wouters, "The land ice contribution to sea level during the satellite era," *Environmental Research Letters*, vol. 13, no. 6, p. 063008, Jun. 2018.

[4] A. S. Gardner, G. Moholdt, J. G. Cogley, B. Wouters, A. A. Arendt, J. Wahr, E. Berthier, R. Hock, W. T. Pfeffer, G. Kaser, S. R. M. Ligtenberg, T. Bolch, M. J. Sharp, J. O. Hagen, M. R. van den Broeke, F. Paul, "A reconciled estimate of glacier contributions to sea level rise: 2003 to 2009," *Science*, vol. 340, pp. 852–857, May 2013.

[5] V. Helm, A. Humbert, and H. Miller, "Elevation and elevation change of Greenland and Antarctica derived from CryoSat-2," *The Cryosphere*, vol. 8, no. 4, pp. 1539–1559, 2014.

[6] The IMBIE team, "Mass balance of the Antarctic Ice Sheet from 1992 to 2017," *Nature*, vol. 558, no. 7709, pp. 219–222, Jun. 2018.

[7] H. J. Zwally, J. Li, A. C. Brenner, M. Beckley, H. G. Cornejo, J. DiMarzio, M. B. Giovinetto, T. A. Neumann, J. Robbins, J. L. Saba, D. Yi, and W. Wang, "Greenland ice sheet mass balance: distribution of increased mass loss with climate warming; 2003–07 versus 1992–2002," *Journal of Glaciology*, vol. 57, no. 201, pp. 88–102, 2011.

[8] B. Wessel, A. Bertram, A. Gruber, S. Bemm, and S. Dech, "A New High-Resolution Elevation Model of Greenland Derived from Tandem-X," *ISPRS Annals of Photogrammetry, Remote Sensing and Spatial Information Sciences*, vol. III–7, pp. 9–16, Jun. 2016.

[9] G. Krieger, A. Moreira, H. Fiedler, I. Hajnsek, M. Werner, M. Younis, and M. Zink, "TanDEM-X: A Satellite Formation for High-Resolution SAR Interferometry," *IEEE Transactions on Geoscience and Remote Sensing*, vol. 45, no. 11, pp. 3317–3341, Nov. 2007.

[10] L. C. Morena, K. V. James, and J. Beck, "An introduction to the RADARSAT-2 mission," *Canadian Journal of Remote Sensing*, vol. 30, no. 3, pp. 221–234, Jan. 2004.

[11] R. Torres, P. Snoeij, D. Geudtner, D. Bibby, M. Davidson, E. Attema, P. Potin, B. Rommen, N. Floury, M. Brown, I. N. Traver, P. Deghaye, B. Duesmann, B. Rosich, N. Miranda, C. Bruno, M. L'Abbate, R. Croci, A. Pietropaolo, M. Huchler, and F. Rostan, "GMES Sentinel-1 mission," *Remote Sensing of Environment*, vol. 120, pp. 9–24, May 2012.

[12] H. Rott, W. A. Jaber, J. Wuite, S. Scheiblauer, D. Floricioiu, J. M. van Wessem, T. Nagler, N. Miranda, and M. R. van den Broeke, "Changing pattern of ice flow and mass balance for glaciers discharging into the Larsen A and B embayments, Antarctic Peninsula, 2011 to 2016," *The Cryosphere*, vol. 12, no. 4, pp. 1273–1291, Apr. 2018.

[13] W. Abdel Jaber, H. Rott, D. Floricioiu, J. Wuite, and N. Miranda, "Heterogeneous spatial and temporal pattern of surface elevation change and mass balance of the Patagonian icefields between 2000 and 2016," *The Cryosphere Discussions*, pp. 1–39, Dec. 2018.

[14] P. Malz, W. Meier, G. Casassa, R. Jaña, P. Skvarca, and M. Braun, "Elevation and Mass Changes of the Southern Patagonia Icefield Derived from TanDEM-X and SRTM Data," *Remote Sensing*, vol. 10, no. 2, p. 188, Jan. 2018.

[15] L. M. Kehrl, I. Joughin, D. E. Shean, D. Floricioiu, and L. Krieger, "Seasonal and interannual variabilities in terminus position, glacier velocity, and surface elevation at Helheim and Kangerlussuaq Glaciers from 2008 to 2016: Helheim and Kangerlussuaq Glaciers," *Journal of Geophysical Research: Earth Surface*, vol. 122, no. 9, pp. 1635–1652, Sep. 2017.

[16] A. Moreira, G. Krieger, I. Hajnsek, K. Papathanassiou, M. Younis, P. Lopez-Dekker, S. Huber, M. Villano, M. Pardini, M. Eineder, F. De Zan, and A. Parizzi, "Tandem-L: A Highly Innovative Bistatic SAR Mission for Global Observation of Dynamic Processes on the Earth's Surface," *IEEE Geoscience and Remote Sensing Magazine*, vol. 3, no. 2, pp. 8–23, Jun. 2015.

[17] J. Dall, "InSAR Elevation Bias Caused by Penetration Into Uniform Volumes," *IEEE Transactions on Geoscience and Remote Sensing*, vol. 45, no. 7, pp. 2319–2324, Jul. 2007.

[18] G. Fischer, G. Parrella, K. P. Papathanassiou, and I. Hajnsek, "Sensitivity of polarimetric SAR interferometry data to different vertical subsurface structures of the Greenland ice sheet," in *Proceedings of IGARSS*, Forth Worth, USA, 2017, pp. 3581–3584.

[19] J. Dall, S. N. Madsen, K. Keller, and R. Forsberg, "Topography and penetration of the Greenland Ice Sheet measured with Airborne SAR Interferometry," *Geophysical Research Letters*, vol. 28, no. 9, pp. 1703–1706, May 2001.

[20] E. Rignot, K. Echelmeyer, and W. Krabill, "Penetration depth of interferometric synthetic aperture radar signals in snow and ice," *Geophysical Research Letters*, vol. 28, no. 18, pp. 3501–3504, Sep. 2001.

[21] J. Li and H. J. Zwally, "Modeling of firn compaction for estimating ice-sheet mass change from observed ice-sheet elevation change," *Annals of Glaciology*, vol. 52, no. 59, pp. 1–7, 2011.

[22] S. R. M. Ligtenberg, M. M. Helsen, and M. R. van den Broeke, "An improved semi-empirical model for the densification of Antarctic firn," *The Cryosphere*, vol. 5, no. 4, pp. 809–819, Oct. 2011.

[23] N. Reeh, "A nonsteady-state firn-densification model for the percolation zone of a glacier," *Journal of Geophysical Research*, vol. 113, no. F3, Sep. 2008.

[24] M. van den Broeke, J. Bamber, J. Ettema, E. Rignot, E. Schrama, W. J. van de Berg, E. van Meijgaard, I. Velicogna, and B. Wouters, "Partitioning Recent Greenland Mass Loss," *Science*, vol. 326, no. 5955, pp. 984–986, Nov. 2009.

[25] S. R. Cloude and K. P. Papathanassiou, "Polarimetric SAR Interferometry," *IEEE Transactions on Geoscience and Remote Sensing*, vol. 36, no. 5, p. 15, 1998.

[26] A. Reigber and A. Moreira, "First demonstration of airborne SAR tomography using multibaseline L-band data," *IEEE Transactions on Geoscience and Remote Sensing*, vol. 38, no. 5, pp. 2142–2152, Sep. 2000.

[27] A. Moreira, P. Prats-Iraola, M. Younis, G. Krieger, I. Hajnsek, and K. P. Papathanassiou, "A tutorial on synthetic aperture radar," *IEEE Geoscience and Remote Sensing Magazine*, vol. 1, no. 1, pp. 6–43, Mar. 2013.

[28] S. Cloude, *Polarisation: applications in remote sensing,* 1st ed. Oxford ; New York: Oxford University Press, 2010.

[29] J.-S. Lee and E. Pottier, *Polarimetric radar imaging: from basics to applications*, Boca Raton: CRC Press, 2009.

[30] R. Bamler and P. Hartl, "Synthetic aperture radar interferometry," *Inverse Problems*, vol. 14, no. 4, pp. R1–R54, Aug. 1998.

[31] J. Sharma, I. Hajnsek, K.P. Papathanassiou, and A. Moreira, "Estimation of glacier ice extinction using long-wavelength airborne Pol-InSAR," *IEEE Transactions on Geoscience and Remote Sensing*, vol. 51, no. 6, pp. 3715-3732, Jun. 2013.

[32] S. Leinss, A. Wiesmann, J. Lemmetyinen, and I. Hajnsek, "Snow Water Equivalent of Dry Snow Measured by Differential Interferometry," *IEEE Journal of Selected Topics in Applied Earth Observations and Remote Sensing*, vol. 8, no. 8, pp. 3773–3790, Aug. 2015.

[33] I. Hajnsek, K. P. Papathanassiou, and S. R. Cloude, "Removal of additive noise in polarimetric eigenvalue processing," in *Proceedings of IGARSS*, Sydney, NSW, Australia, 2001, pp. 2778–2780.

[34] F. Gatelli, A. Monti Guamieri, F. Parizzi, P. Pasquali, C. Prati, and F. Rocca, "The wavenumber shift in SAR interferometry," *IEEE Transactions on Geoscience and Remote Sensing*, vol. 32, no. 4, pp. 855–865, Jul. 1994.

[35] G. Krieger, K. P. Papathanassiou, and S. R. Cloude, "Spaceborne Polarimetric SAR Interferometry: Performance Analysis and Mission Concepts," *EURASIP Journal on Advances in Signal Processing*, vol. 2005, no. 20, Dec. 2005.

[36] R. N. Treuhaft and P. R. Siqueira, "Vertical structure of vegetated land surfaces from interferometric and polarimetric radar," *Radio Science*, vol. 35, no. 1, pp. 141–177, Jan. 2000.

[37] S. R. Cloude and K. P. Papathanassiou, "Three-stage inversion process for polarimetric SAR interferometry," *IEE Proceedings - Radar, Sonar and Navigation*, vol. 150, no. 3, p. 125, 2003.

[38] S. Tebaldini, T. Nagler, H. Rott, and A. Heilig, "Imaging the Internal Structure of an Alpine Glacier via L-Band Airborne SAR Tomography," *IEEE Transactions on Geoscience and Remote Sensing*, vol. 54, no. 12, pp. 7197–7209, Dec. 2016.

[39] F. Banda, J. Dall, and S. Tebaldini, "Single and Multipolarimetric P-Band SAR Tomography of Subsurface Ice Structure," *IEEE Transactions on Geoscience and Remote Sensing*, vol. 54, no. 5, pp. 2832–2845, May 2016.

[40] F. Gini and F. Lombardini, "Multibaseline cross-track SAR interferometry: a signal processing perspective," *IEEE Aerospace and Electronic Systems Magazine*, vol. 20, no. 8, pp. 71–93, Aug. 2005.

[41] P. Stoica and R. L. Moses, *Spectral analysis of signals*, Upper Saddle River, N.J: Pearson/Prentice Hall, 2005.

[42] R. Schmidt, “Multiple emitter location and signal parameter estimation,” *IEEE Transactions on Antennas and Propagation*, vol. 34, no. 3, pp. 276–280, Mar. 1986.

[43] C. S. Benson, *Stratigraphic Studies in the Snow and Firn of the Greenland Ice Sheet*, U.S. Army Snow, Ice and Permafrost Research Establishment, 1962, Reprinted Aug. 1996.

[44] W. S. B. Paterson, *The physics of glaciers*, 3rd ed. Oxford, OX, England; Tarrytown, N.Y., U.S.A: Pergamon, 1994.

[45] S. V. Nghiem, D. K. Hall, T. L. Mote, M. Tedesco, M. R. Albert, K. Keegan, C. A. Shuman, N. E. DiGirolamo, and G. Neumann, , “The extreme melt across the Greenland ice sheet in 2012,” *Geophysical Research Letters*, vol. 39, no. 20, Oct. 2012.

[46] M. Fahnestock, R. Bindschadler, R. Kwok, and K. Jezek, “Greenland ice sheet surface properties and ice dynamics from ERS-1 SAR imagery,” *Science*, vol. 262, no. 5139, pp. 1530–1534, Dec. 1993.

[47] K. C. Jezek, P. Gogineni, and M. Shanableh, “Radar measurements of melt zones on the Greenland Ice Sheet,” *Geophysical Research Letters*, vol. 21, no. 1, pp. 33–36, Jan. 1994.

[48] P. Rizzoli, M. Martone, H. Rott, and A. Moreira, “Characterization of snow facies on the Greenland ice sheet observed by TanDEM-X interferometric SAR data,” *Remote Sensing,* vol. 9, no. 4, p. 315, Mar. 2017.

[49] K. C. Partington, “Discrimination of glacier facies using multi-temporal SAR data,” *Journal of Glaciology*, vol. 44, no. 146, pp. 42–53, 1998.

[50] M. Pardini, G. Parrella, G. Fischer, and K. Papathanassiou, “A Multi-Frequency SAR Tomographic Characterization of Sub-Surface Ice Volumes,” in *Proceedings of EUSAR*, Hamburg, Germany, 2016, pp. 1-6.

[51] F. T. Ulaby, R. K. Moore, and A. K. Fung, *Radar remote sensing and surface scattering and emission theory,* Norwood, Mass: ARTECH House, 1982.

[52] V. Parry, P. Nienow, D. Mair, J. Scott, B. Hubbard, K. Steffen, and D. Wingham, “Investigations of meltwater refreezing and density variations in the snowpack and firn within the percolation zone of the Greenland ice sheet,” *Annals of Glaciology*, vol. 46, pp. 61–68, 2007.

[53] J. Freitag, S. Kipfstuhl, S. Hoerz, L. Eling, B. Vinther, and T. Popp, “Melt layer statistic of two firn cores recently drilled at Dye3 and South Dome in the dry snow zone of Southern Greenland,” *presented at the EGU General Assembly*, Vienna, Austria, Apr./May 2014.

[54] M. P. Lüthi, C. Ryser, L. C. Andrews, G. A. Catania, M. Funk, R. L. Hawley, M. J. Hoffman, and T. A. Neumann, “Heat sources within the Greenland Ice Sheet: dissipation, temperate paleo-firn and cryo-hydrologic warming,” *The Cryosphere*, vol. 9, no. 1, pp. 245–253, Feb. 2015.

[55] J. Brown, J. Bradford, J. Harper, W. T. Pfeffer, N. Humphrey, and E. Mosley-Thompson, “Georadar-derived estimates of firn density in the percolation zone, western Greenland ice sheet,” *Journal of Geophysical Research: Earth Surface*, vol. 117, no. F1, pp. 1-14, Mar. 2012.

[56] C. Leuschen, “IceBridge accumulation radar L1B geolocated radar echo strength profiles, version 2,” *Nat. Snow Ice Data Center*, Boulder, CO, USA, 2015. [Online]. Available: https://nsidc.org/data/iracc1b, doi: 10.5067/0ZY1XYHNIQNY.

[57] D. Steinhage, S. Kipfstuhl, and H. Miller, “Interpolating accumulation rates by means of internal layering detected by airborne radio-echo sounding,” *Symposium on Radioglaciology*, Lawrence, KS, USA, Sep. 2013.

[58] H. Rott, “The analysis of backscattering properties from SAR data of mountain regions,” *IEEE Journal of Oceanic Engineering*, vol. 9, no. 5, pp. 347–355, Dec. 1984.

[59] R. Forster, K. C. Jezek, J. Bolzan, F. Baumgartner, and S. P. Gogineni, “Relationships between radar backscatter and accumulation rates on the Greenland ice sheet,” *International Journal of Remote Sensing*, vol. 20, nos. 15-16, pp. 3131–3147, Jan. 1999.

[60] G. Rotschky, W. Rack, W. Dierking, and H. Oerter, “Retrieving snowpack properties and accumulation estimates from a combination of SAR and scatterometer measurements,” *IEEE Transactions on Geoscience and Remote Sensing*, vol. 44, no. 4, pp. 943–956, Apr. 2006.

[61] K. C. Jezek, M. R. Drinkwater, J. P. Crawford, R. Bindschadler, and R. Kwok, “Analysis of synthetic aperture radar data collected over the southwestern Greenland ice sheet,” *Journal of Glaciology*, vol. 39, no. 131, pp. 119–132, Jan. 1993.

[62] E. J. Rignot, S. Ostro, J. J. van Zyl, and K. C. Jezek, “Unusual radar echoes from the Greenland ice sheet,” *Science*, vol. 261, no. 5129, pp. 1710–1713, Sep. 1993.

[63] E. J. Rignot, “Backscatter model for the unusual radar properties of the Greenland ice sheet,” *Journal of Geophysical Research*, vol. 100, no. E5, pp. 9389–9400, May 1995.

[64] J. J. Sharma, I. Hajnsek, K. P. Papathanassiou, and A. Moreira, “Polarimetric decomposition over glacier ice using long-wavelength airborne PolSAR,” *IEEE Transactions on Geoscience and Remote Sensing*, vol. 49, no. 1, pp. 519–535, Jan. 2011.

[65] G. Parrella, I. Hajnsek, and K. P. Papathanassiou, “Polarimetric decomposition of L-band PolSAR backscattering over the Austfonna ice cap,” *IEEE Transactions on Geoscience and Remote Sensing*, vol. 54, no. 3, pp. 1267–1281, Mar. 2016.

[66] E. W. Hoen and H. Zebker, “Penetration depths inferred from interferometric volume decorrelation observed over the Greenland ice sheet,” *IEEE Transactions on Geoscience and Remote Sensing*, vol. 38, no. 6, pp. 2571–2583, Nov. 2000.

[67] S. Oveisgharan and H. A. Zebker, “Estimating snow accumulation from InSAR correlation observations,” *IEEE Transactions on Geoscience and Remote Sensing*, vol. 45, no. 1, pp. 10–20, Jan. 2007.

[68] C. Mätzler, “Improved Born approximation for scattering of radiation in a granular medium,” *Journal of Applied Physics*, vol. 83, no. 11, pp. 6111–6117, Jun. 1998.

[69] S. Hensley, D. Moller, S. Oveisgharan, T. Michel, and X. Wu, “Ka-Band Mapping and Measurements of Interferometric Penetration of the Greenland Ice Sheets by the GLISTIN Radar,” *IEEE Journal of Selected Topics in Applied Earth Observations and Remote Sensing*, vol. 9, no. 6, pp. 2436–2450, Jun. 2016.

[70] J. Dall, K.P. Papathanassiou, and H. Skriver, “Polarimetric SAR interferometry applied to land ice: Modeling,” in *Proceedings of EUSAR*, Ulm, Germany, 2004, pp. 247-250.

[71] K. P. Papathanassiou and S. R. Cloude, “Single-baseline polarimetric SAR interferometry,” *IEEE Transactions on Geoscience and Remote Sensing*, vol. 39, no. 11, pp. 2352–2363, Nov. 2001.

[72] O. Stebler, A. Schwerzmann, M. Luthi, E. Meier, and D. Nuesch, “Pol-InSAR observations from an Alpine glacier in the cold infiltration zone at L- and P-band,” *IEEE Geoscience Remote Sensing Letters*, vol. 2, no. 3, pp. 357-361, Jul. 2005.

[73] T. Nagler, H. Rott, I. Hajnsek, K.P. Papathanassiou, and R. Scheiber, “An airborne experiment on snow parameter retrieval by means of multi-channel SAR data,” in *Proceedings of EUSAR*, Dresden, Germany, May 2006, pp. 1-4.

[74] B. Rekioua, M. Davy, L. Ferro-Famil, and S. Tebaldini, “Snowpack permittivity profile retrieval from tomographic SAR data,” *Comptes Rendus Physique*, vol. 18, no. 1, pp. 57–65, Jan. 2017.

[75] T. G. Yitayew, L. Ferro-Famil, T. Eltoft, and S. Tebaldini, “Lake and Fjord Ice Imaging Using a Multifrequency Ground-Based Tomographic SAR System,” *IEEE Journal of Selected Topics in Applied Earth Observations and Remote Sensing*, vol. 10, no. 10, pp. 4457–4468, Oct. 2017.

[76] H. Skourup, V. R. Barletta, I. Einarsson, R. Forsberg, C. Haas, V. Helm, S. Hendricks, S. M. Hvidegaard, and L. S. Sørensen, “ESA CryoVEx 2011: airborne field campaign with ASIRAS radar, EM induction sounder and laser scanner”. Kgs.Lyngby, DTU Space, Technical Report, 2013.

[77] R. S. W. van de Wal, W. Boot, C. J. P. P. Smeets, H. Snellen, M. R. van den Broeke, and J. Oerlemans, “Twenty-one years of mass balance observations along the K-transect, West Greenland,” *Earth System Science Data*, vol. 4, no. 1, pp. 31–35, Aug. 2012.

[78] R. S. Fausto and D. van As, “Programme for monitoring of the Greenland ice sheet (PROMICE): Automatic weather station data. Version: v03”, Dataset published via *Geological Survey of Denmark and Greenland*, 2019. [Online]. Available: http://www.promice.org, doi: https://doi.org/10.22008/promice/data/aws

[79] K. Steffen, J. E. Box, and W. Abdalati, “Greenland climate network: GC-net,” in *CRREL 96-27 Special Report on Glaciers, Ice Sheets and Volcanoes,* S. C. Colbeck, Ed., Hanover, NH, USA: U.S. Army Cold Regions Research and Engineering Laboratory, 1996, pp. 98-103.

[80] A. Reigber, R. Scheiber, M. Jäger, P. Prats-Iraola, I. Hajnsek, T. Jagdhuber, K. P. Papathanassiou, M. Nannini, E. Aguilera, S. Baumgartner, R. Horn, A. Nottensteiner, A. Moreira, “Very-High-Resolution Airborne Synthetic Aperture Radar Imaging: Signal Processing and Applications,” *Proceedings of IEEE*, vol. 101, no. 3, pp. 759–783, Mar. 2013.

[81] M. Jäger, R. Scheiber, and A. Reigber, “External Calibration of Multi-Channel SAR Sensors Based on the Pulse-by-Pulse Analysis of Range Compressed Data,” in *Proceedings of EUSAR*, Aachen, Germany, Jun. 2018, pp. 75–78.

[82] H. M. Jol, *Ground Penetrating Radar Theory and Applications.* Amsterdam, The Netherlands: Elsevier, 2009.

2 MODELING MULTIFREQUENCY POL-INSAR DATA FROM THE PERCOLATION ZONE OF THE GREENLAND ICE SHEET

G. Fischer, K. P. Papathanassiou, and I. Hajnsek

IEEE Transactions on Geoscience and Remote Sensing

Published in vol. 57, no. 4, pp. 1963 – 1976, April 2019. DOI:10.1109/TGRS.2018.2870301

This chapter is a post-print, differing from the published paper only in terms of layout and formatting.

The author's contributions:

- Interferometric processing and analysis of the SAR data.
- Modeling of the effect of subsurface layers on interferometric SAR data.
- Analysis and interpretation of the SAR data based on the developed model.
- Writing of the manuscript.

The co-authors' contributions:

- I. Hajnsek and K. P. Papathanassiou provided guidance throughout the research.
- I. Hajnsek and K. P. Papathanassiou contributed to the main ideas, the discussion of the results, and reviewed the manuscript.

MODELING MULTIFREQUENCY POL-INSAR DATA FROM THE PERCOLATION ZONE OF THE GREENLAND ICE SHEET

Georg Fischer[1,2], Konstantinos P. Papathanassiou[1], and Irena Hajnsek[1,2]
[1] German Aerospace Center, Microwaves and Radar Institute, Wessling, Germany
[2] ETH Zurich, Institute of Environmental Engineering, Zurich, Switzerland

Abstract

The analysis of data from an airborne synthetic aperture radar (SAR) campaign in the percolation zone of Greenland revealed an interferometric coherence undulation behavior with respect to vertical wavenumber, which cannot be explained with existing models. We propose a model extension that accounts for scattering from distinct layers below the surface. Simulations show that the periodicity of the coherence undulation is mainly driven by the vertical distance between dominant subsurface layers, while the amplitude of the undulation is determined by the ratio between scattering from distinct layers and scattering from the firn volume. We use the model to interpret quad-pol SAR data at X-, C-, S-, L-, and P-bands. The inferred layer depths match layer detections in ground-based radar data and in situ measurements. We conclude that in the percolation zone, scattering from subsurface layers has to be taken into account to correctly interpret SAR data and demonstrate the potential to retrieve geophysical information about the vertical subsurface structure.

2.1 INTRODUCTION

The dynamics of glaciers and ice sheets are an important indicator of climate change with implications on environment and society [1]. While mass balance estimations are derived today from remote sensing data, uncertainties due to subsurface structure and density related to melt-refreeze processes remain [1], [2]. Synthetic aperture radar (SAR) measurements provide a way to address these uncertainties due to their penetration into glaciers and ice sheets, especially at lower frequencies, and their sensitivity to different conditions of snow, firn, and ice. This potentially allows inferring information about the vertical subsurface structure. However, the methodology and the algorithms to extract physical vertical structure parameters from SAR data are not established, because it is not yet fully understood how the vertical structure below the surface affects SAR measurements.

Early studies make use of SAR backscattering coefficients to estimate accumulation rates [3], [4] and to map glacier zones [5]. One step forward toward subsurface characterization was the development of decompositions and models to interpret polarimetric SAR (PolSAR) data from glaciers and ice sheets. Based on polarimetric studies that indicated the sensitivity of polarimetric backscatter to glacier zones [6], [7], first polarimetric models considered ice lenses

and glands as the main scattering contributions [8]. Further advances in polarimetric modeling improved the ability to describe the subsurface of an ice cap in Svalbard [9], [10]. However, PolSAR measurements cannot resolve the vertical distribution of the scattering contributions.

The vertical distribution of scatterers in the subsurface can be retrieved by SAR interferometry (InSAR). Hoen and Zebker [11] modeled the subsurface of ice sheets as a uniform lossy volume with constant extinction and infinite depth to analyze InSAR coherence measurements at C-band. This approach allows the estimation of the penetration depth of InSAR signals which is related to the vertical structure of scatterers. The dependence of the penetration depth on different snow, firn, and ice conditions was also reported by Rignot *et al.* [12]. A model proposed by Oveisgharan and Zebker [13] aimed to relate accumulation rates in the dry snow zone of Greenland to InSAR coherences by assuming a layered firn body. Even if the study was hampered by a time difference of 83 years between the SAR measurements and validation data, it indicated the potential to analyze vertically layered firn with InSAR. Nevertheless, the uniform volume assumption [11] is still used in recent studies for the characterization of ice sheets [14].

The combination of both aforementioned techniques, by means of Pol-InSAR [15], allows investigating the vertical distribution of different scattering processes and was successfully used to estimate physical structure parameters from natural volumes, particularly in forest applications. Few studies have assessed the potential of Pol-InSAR to retrieve geophysical information from glaciers and ice sheets. Sharma *et al.* [16] employed a polarimetric decomposition to separate surface from volume scattering contributions and then used the uniform volume model [11] to retrieve extinction coefficients at L- and P-bands over the Austfonna ice cap in Svalbard. Stebler *et al.* [17] demonstrated that different subsurface structures at different glacier zones have a clear separable effect on Pol-InSAR coherences. Despite this, the existing approaches are still very limited in the interpretation of Pol-InSAR data [18], [19] and therefore also in the retrieval of geophysical information, since the combination of a uniform volume and scattering from the surface has only limited flexibility to represent different scattering scenarios from glaciers and ice sheets.

Recent polarimetric studies improved the understanding of anisotropic propagation behavior of snow [20] and firn [10], and investigated the polarimetric scattering characteristics from oriented particles within the firn volume [10]. This overcomes assumptions made in earlier Pol-InSAR studies [16] about scattering from sastrugi, which is only applicable to specific areas if acquired under certain radar aspect angles.

New developments indicated the necessity to consider the impact of subsurface layers on InSAR coherence [21], [22]. The term *layer* is used in the literature for both thin layers associated with surface scattering mechanisms [13], [16], [20], [22] as well as extended firn bodies associated with volume scattering [10], [11], [13], [16], [19]. We use the first meaning, referring to clear discontinuities within the firn column in the percolation zone of glaciers and ice sheets. We refer to the first layer as the snow-firn interface, which corresponds to the surface at the end of the last summer, ignoring a shallow winter snow pack, which is likely transparent at microwave frequencies if it is dry and did not experience melting [20].

Even though Hoen [23] and Oveisgharan and Zebker [13] already considered a layered subsurface to improve the correlation between modeled and in situ accumulation rates, a direct assessment of subsurface layer effects in InSAR data is missing. A concise modeling effort of such effects, with limited a priori assumptions, may facilitate the development of robust retrieval algorithms. The objective of this paper is to advance these findings and to propose a realistic scattering model for the interpretation of Pol-InSAR data collected in the percolation zone of Greenland.

In Section 2.2, the experimental SAR data and ground measurements of this paper are described. The proposed multiple-layer-plus-volume model is introduced and discussed in Section 2.3. In Section 2.4, the SAR data are analyzed with respect to the model characteristics, followed by discussions and conclusions in Section 2.5.

2.2 EXPERIMENTAL DATA

2.2.1 ARCTIC15 CAMPAIGN AND THE SOUTH DOME TEST SITE

This paper is based on an airborne SAR data set acquired during April and May 2015 in Greenland with DLR's F-SAR system [24] in the frame of the ARCTIC15 campaign. Fully polarimetric, multibaseline interferometric SAR data were acquired at five different frequencies (X-, C-, S-, L-, and P-bands; 9.6, 5.3, 3.3, 1.3, and 0.44 GHz, respectively) over different glacier zones.

This paper focuses on the South Dome test site (63.52° N, 44.54° W, Alt.: 2868 m, see Fig. 1), where SAR data covering an area of approximately 6 km × 3 km were acquired. Coordinated ground activities were carried out by the German Aerospace Center (DLR) and ETH Zurich, which comprised the placement of corner reflectors, the acquisition of ground penetrating radar (GPR) and GNSS profiles, as well as manual probing of near surface layers with an accumulation probe.

The F-SAR was flown at 3000 m altitude above ground, with six to eight parallel flight tracks from two opposite headings. The nominal horizontal baselines were 10–90 m for the X-, S-, and L-band acquisitions and 5–35 m at the opposite heading at X-, C-, and L-bands. P-band data were acquired during a separate flight 16 days later with nominal horizontal baselines of 10–270 m. The incidence angle varies from 25° to 60°, and the spatial resolution is between 0.5 m (azimuth) × 0.6 m (slant range) at X-band and 1 m × 3.8 m at P-band.

Different baselines and the incidence angle variation lead to a wide range of vertical wavenumbers k_z that has been exploited in this paper. In all frequencies, k_z values below 0.1 rad/m exist, except for S-band where the smallest value is 0.2 rad/m. The maximum k_z values are at least 2.8 rad/m in all frequencies.

Temporal decorrelation can be neglected for the ARCTIC15 data with only about 15 min between consecutive acquisitions and a maximum temporal separation of 1 h 45 min at stable negative temperatures. Noise decorrelation γ_{SNR} is well above 0.94 (above 0.99 at L- and

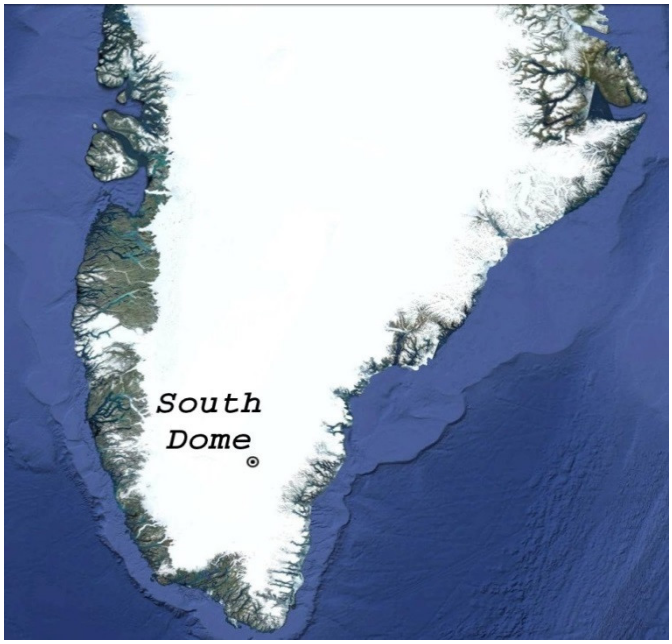

Fig. 1. Location of the South Dome test site in the southern part of Greenland.

P-bands), due to the strong backscatter in the percolation zone of Greenland. Therefore, its effect on the presented results is marginal. Nevertheless, the magnitude of the interferometric coherence $|\gamma|$, which this paper focuses on, is corrected for γ_{SNR} by means of the polarimetric HV - VH coherence [25].

Each interferometric image pair was common bandwidth filtered individually, accounting for the variation of the incidence angle over range [26]. The coregistration was performed using a reference DEM generated from X-band single-pass InSAR data acquired by F-SAR during the campaign.

2.2.2 Ground Measurements

South Dome is located in the percolation zone, where refreezing of seasonal melt water leads to high-density ice layers in the firn column, which are considered strong scatterers in both GPR and SAR data. Therefore, GPR data can provide the necessary information on the vertical subsurface structure to understand its influence on Pol-InSAR measurements. In particular, layers related to years with stronger melting are visible in GPR profiles, which is confirmed by firn cores [27].

For this purpose, more than 2 km of GPR transects were acquired one week before the X-, C-, S-, and L-band and two weeks after the P-band acquisitions using a 500-MHz pulse radar system. The profiles acquired before and after the SAR acquisitions are very similar without any recognizable differences.

The time window of the GPR measurements was 377 ns, corresponding to a depth range of almost 40 m, even though the last 5 m are dominated by noise. The theoretical vertical resolution is about 20 cm in firn. A basic processing chain was applied, including removal of direct current bias, time-zero correction, bandpass filtering, and gain adjustment [28].

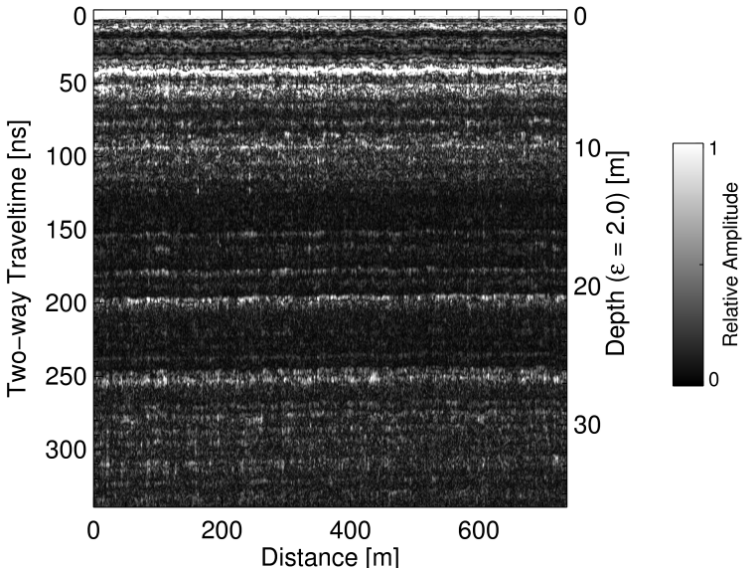

Fig. 2. Amplitude envelope of a GPR profile at South Dome. Several layers with varying backscattered power are visible.

One example of our GPR measurements at South Dome is shown in Fig. 2, revealing the aforementioned stratigraphy with its distinct layers and a particular strong one at about -4.5 m depth.

The layered subsurface structure visible in our GPR data was confirmed by echograms from the Accumulation Radar instrument of NASA's Operation IceBridge [29] acquired in April 2014. The effect of the one year difference is limited due to the average accumulation rate of approximately 0.5 m water equivalent per year [30]. The large coverage of Accumulation Radar data confirmed the horizontal homogeneity of the subsurface structure in the South Dome area at larger distances then our SAR coverage. Therefore, we consider the GPR profiles to be representative for the entire test site.

Complementary information about stratigraphy in the first 3-4 m was collected with an accumulation probe, which was used to manually detect hard layers within the firn. The layer detections for South Dome are shown in Fig. 3. Two to five samples were taken at three locations in the SAR scene center before and after the SAR acquisitions. The consistency of the layer readings was encouraging even though the individual point measurements have a randomness to hit or miss ice lenses that form the layers. The depth accuracy of the manual readings on the accumulation probe was assessed to be ±5 cm, which is accurate enough for our purposes. These measurements are considered reliable only in case of consistently detected layers. Thinner and weaker layers were likely to be penetrated without a clear reading, e.g., the inconsistent detections around -1 m depth in Fig. 3.

The layer at -3 m was detected most consistently, with further detections just a few centimeters below which were sometimes recorded as a single thicker layer. Based on the average accumulation rate [30] and snow radar data [31], the spacing of annual layers is about 1 m, which matches our manual measurements, even though potential layers at -1 and -2 m were not consistently detected.

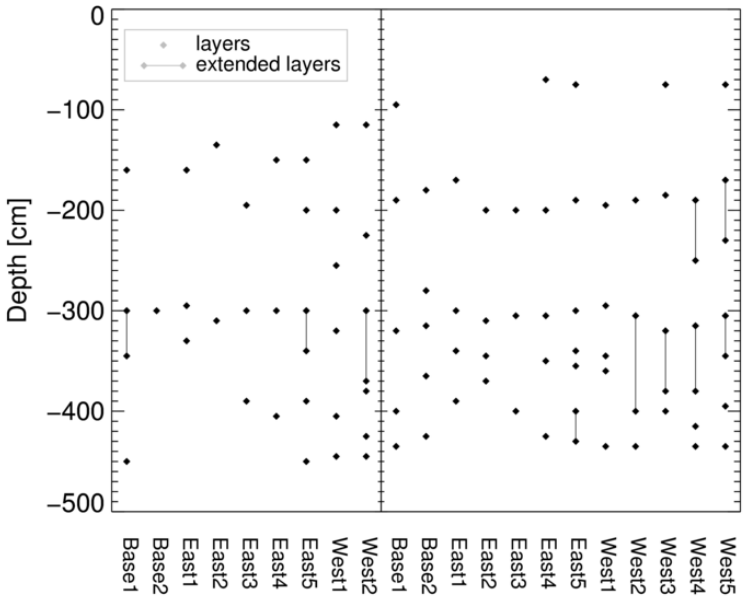

Fig. 3. Manual layer probing results at South Dome from measurements before (April 25, 2015, left part) and after (May 28, 2015, right part) the SAR acquisitions.

All our in situ and SAR data were acquired within 33 days. We consider the situation temporally stable throughout this period with negative temperatures and only 1 cm snow height change based on data from the South Dome weather station of the Greenland Climate Network [32].

2.2.3 POLSAR ASSESSMENT

South Dome is the highest elevated area in the south of Greenland and is a flat and horizontally homogeneous plateau with a maximum elevation difference of less than 20 m within the area imaged by the SAR. This homogeneity is also revealed by the Pauli color composite images of polarimetric backscatter in Fig. 4 (top). Since there are no visible changes along azimuth for any given frequency, we aggregated all five frequencies into a single image. Within one frequency, only a range trend is present due to the incidence angle variation indicating stronger scattering in HH+VV, typically interpreted as surface scattering, in near range. The overall very strong HV channel, which is increasing with frequency, is typically associated with volume scattering.

Conventional polarimetric analyses by means of the entropy and alpha scattering parameters [33] indicate dominant volume scattering with overall high entropy values, e.g., above 0.8, and alpha angles between 40° and 60° at X-, C-, S-, and L-bands. At P-band entropy ranges between 0.2 and 0.55 and alpha between 15° and 40°. Scattering entropy and alpha for all frequencies are shown in Fig. 4 (middle and bottom). An increase with incidence angle can be observed, and entropy and alpha saturate around 0.9° and 55°, respectively, for X-, C-, S-, and L-bands. This increase of both parameters with incidence angle is related to the fact that volume scattering decreases significantly less (theoretically not at all) with incidence angle than surface scattering.

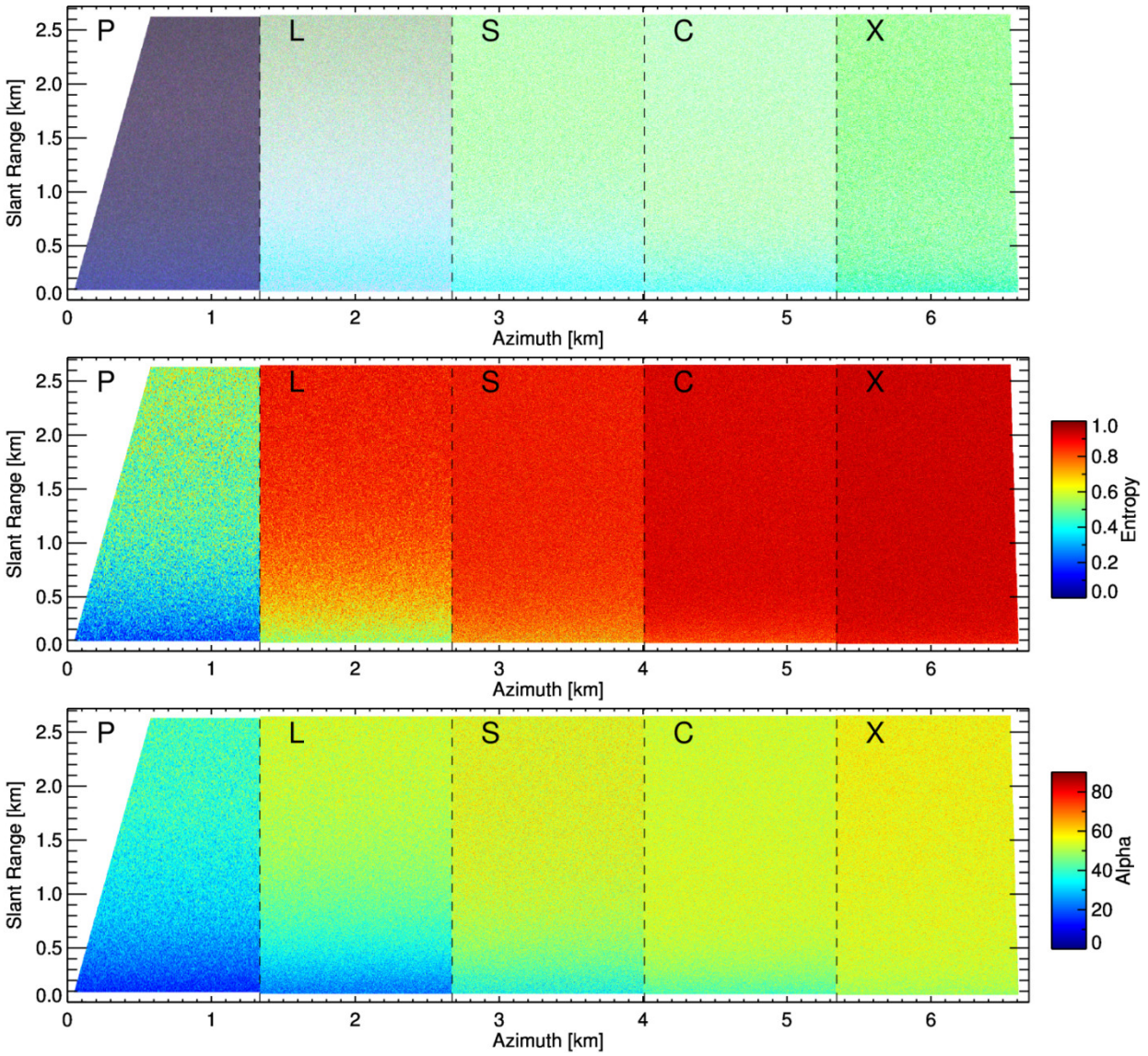

Fig. 4. (Top) Multifrequency Pauli representation (HH + VV: blue, HH - VV: red, and HV: green) of the South Dome test site at 63.52° N, 44.54° W, Alt.: 2868 m. (Middle) Scattering entropy parameter. (Bottom) Scattering alpha parameter. Due to the horizontal homogeneity of the area, P-, L-, S-, C-, and X-bands are aggregated into a single graphic for illustration purposes. Within one frequency, only a range trend due to incidence angle variation is present, while the azimuth dimension is constant across the entire scene.

At the same time, entropy and alpha increase with frequency due to an increased depolarization of surface scattering induced by the increase in effective roughness. Also, smaller particles may contribute additionally to volume scattering at higher frequencies.

Backscatter values are well above -15 dB even at HV at 60° incidence angle for L-band and increase up to 0.7 dB at 28° incidence angle in HH. Only at P-band HV drops to -29 dB. The noise contribution to the high entropy values is marginal, since the signal-to-noise ratio stays above 11 dB for all frequencies and polarizations.

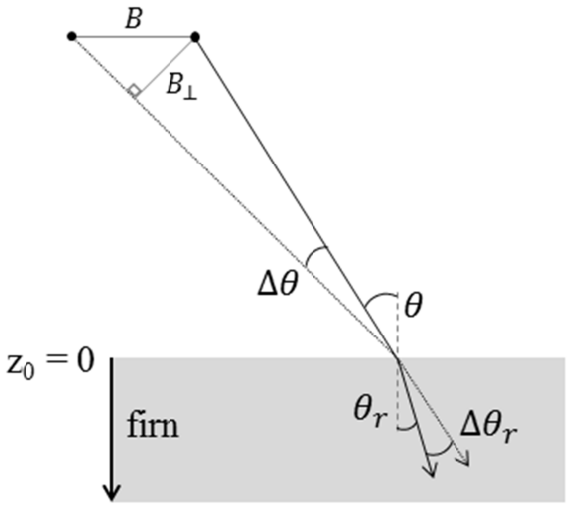

Fig. 5. InSAR geometry considering the refraction into the firn body, ignoring the shallow, partial cover of low-density snow.

2.2.4 InSAR Coherence Profiles at L-Band

While the polarimetric backscatter analysis indicated only a frequency and incidence angle dependence, the interferometric analysis revealed an "unusual" undulation pattern of the InSAR coherence [22], which was the initial trigger of this paper.

The complex interferometric coherence γ is obtained by forming the normalized cross correlation between the interferometric image pair s_1 and s_2 at a given polarization $\vec{w}$ [15], [33]

$$\gamma(\vec{w}) = \frac{\langle s_1(\vec{w}) s_2^*(\vec{w}) \rangle}{\sqrt{\langle s_1(\vec{w}) s_1^*(\vec{w}) \rangle \langle s_2(\vec{w}) s_2^*(\vec{w}) \rangle}} . \tag{1}$$

After common bandwidth filtering, the compensation of additive noise decorrelation and neglecting temporal decorrelation, the remaining volume coherence depends on the vertical distribution of backscattering $\sigma_v(z)$, stretching from z_0 at the glacier surface (i.e., snow-firn interface, respectively, the surface at the end of the last summer) to depth z, as depicted in Fig. 5, and can be written as

$$\gamma_{Vol} = e^{ik_z z_0} \frac{\int_{-\infty}^{0} \sigma_v(z) e^{ik_{zVol} z} dz}{\int_{-\infty}^{0} \sigma_v(z) dz} \tag{2}$$

with topographic phase $e^{ik_z z_0}$. k_{zVol} is the vertical wavenumber in the subsurface volume, considering refraction and permittivity in the glacier subsurface [16]

$$k_{zVol} = \frac{4\pi\sqrt{\epsilon_r}}{\lambda} \frac{\Delta\theta_r}{sin\theta_r} , \tag{3}$$

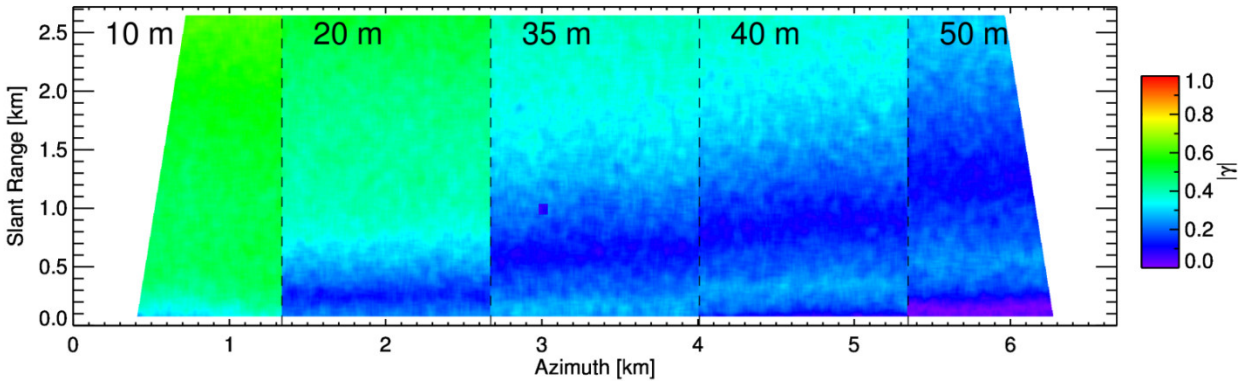

Fig. 6. L-band interferometric HH coherence at five different horizontal baselines, indicated in the image, at a flight altitude of 3000 m over ground at the South Dome test site. Overall a strong volume decorrelation is observed which is undulated with range in dependence of horizontal baseline. Large estimation windows of at least 3200 looks are applied to reduce coherence estimation bias. Average vertical wavenumbers k_{zVol} are 0.19, 0.30, 0.49, 0.58, and 0.78 rad/m, respectively. The effect of a corner reflector is visible in the middle of the scene at 3 km azimuth and 1 km slant range.

with λ being the wavelength in free space and ϵ_r the bulk relative permittivity of the subsurface volume in which the signal penetrates into. $\Delta\theta_r$ is the angular difference, after considering refraction into the firn, between the two radar look vectors of the interferograms, driven by the spatial baseline between the acquisitions, as depicted in Fig. 5. Similarly, θ_r is the refracted incidence angle within the firn volume given by Snell's law. The permittivity ϵ_r can be derived from the density of firn cores [27] through established relationships [34] and is set to 2.0 throughout this analysis. We use a real-valued permittivity since scattering losses dominate over absorption losses under dry and frozen conditions [34].

During the field work, a partial cover of loose snow of about 5 cm was present on top of an already compacted surface. The last substantial snow height increase measured at the South Dome weather station of the Greenland Climate Network [32] was about 10 cm around March 20, 2015, 41 and 56 days prior to our SAR acquisitions. This fine grained, low density snow, which is likely to be transparent at microwave frequencies, is ignored here, due to its marginal extent.

Fig. 6 shows the magnitude of the interferometric coherence $|\gamma|$ at L-band in HH polarization for five different baselines with average k_{zVol} between 0.19 and 0.78 rad/m. In general, coherence values are very low due to strong volume decorrelation, which was expected after the PolSAR analysis. An undulation of coherence is observed in range, which changes with baseline. The analysis of the full data set showed that the undulation pattern changes also with frequency. In fact, the undulation is a function of vertical wavenumber k_{zVol}.

Average L-band coherence profiles are shown in Fig. 7 and demonstrate the dependence on k_{zVol}. We derived the coherence profiles for this analysis using 2-D histograms of $|\gamma|$ against k_{zVol} for each scene. In order to cope with the low $|\gamma|$ values, large estimation windows with at least 3200 looks are used to reduce the coherence estimation bias and standard deviation. The slant range size of the resulting estimation windows is up to 86 m × 181 m, which is no problem due to the horizontal homogeneity of the test site. The profiles from six different horizontal

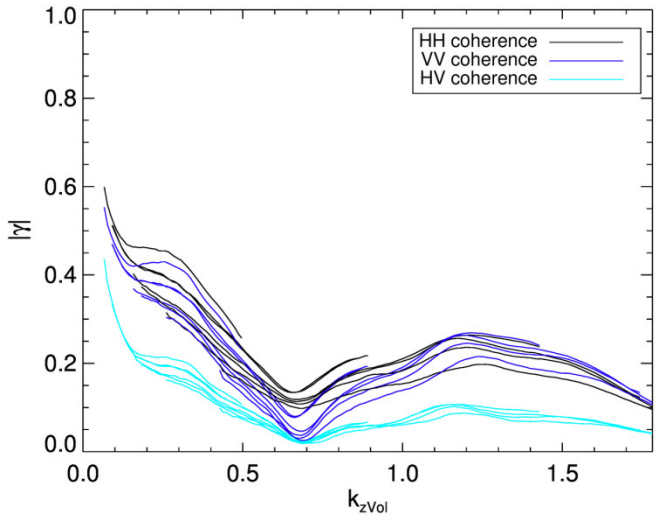

Fig. 7. Coherence profiles at L-band for South Dome versus k_{zVol} for six different horizontal baselines (Between 10 and 50 m horizontal baselines, flight altitude 3000 m above ground). HH, VV, and HV profiles are depicted in black, blue, and cyan, respectively. The vertical spread at each polarization is related to the fact that the same k_{zVol} values correspond to different incidence angles for different baselines.

baselines from 10 to 50 m strongly overlap. The coherence profile from the shortest baseline with 0.05 rad/m (in far range) $< k_{zVol} <$ 0.5 rad/m (in near range) is the only profile not affected by the main undulation pattern (see also Fig. 6), with a coherence minimum at $k_{zVol} \approx$ 0.65 rad/m. It is important to clarify that due to the different horizontal baselines behind each profile, the same k_{zVol} corresponds to different incidence angles. This leads to different surface scattering contributions at the same k_{zVol}, which is the reason for the vertical variation of the overlapping profiles.

The uniform volume model [11] for InSAR coherences from ice sheets assumes an infinitely deep volume of uniformly distributed scatterers characterized by a constant extinction. It predicts an exponential decay of the coherence with k_{zVol} (solid line in Fig. 8), which is not observed in the data. The differences between the co-pol and cross-pol profiles indicate different vertical structure functions for different polarization channels.

We therefore conclude that the shown coherence undulation and the polarization dependence introduce the necessity for a different scattering model for the interpretation of Pol-InSAR data over glaciers and ice sheets.

2.3 Multiple Layer plus Volume Model

In this section, we discuss interferometric coherence models appropriate to interpret the experimental data. The coherence model for a uniform volume, a two layer structure and their combination is introduced step by step. Simulations are used to illustrate the effects of the key parameters layer depth, layer-to-volume scattering ratio and number of layers.

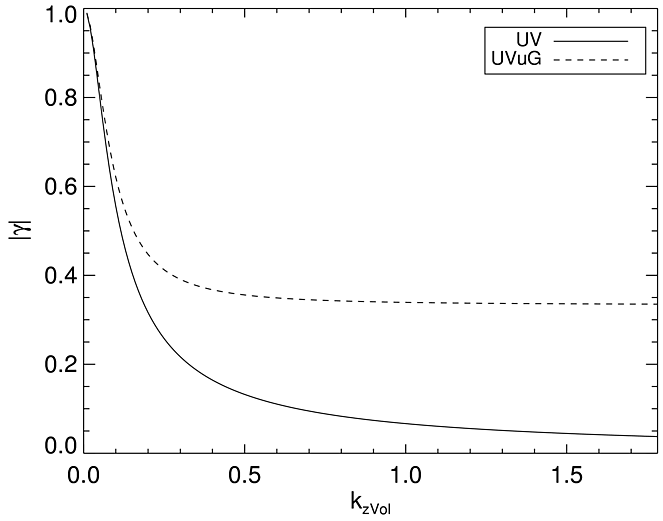

Fig. 8. One example of a coherence profile from a uniform volume model with penetration depth parameter set to 30 m and a uniform volume under ground model with ground-to-volume ratio 0.5.

2.3.1 Uniform Volume Model

Assuming a uniform distribution of scatterers with a constant extinction coefficient $\kappa_e(\vec{w})$ [11], the vertical structure function $\sigma_v(z)$ in (2) becomes an exponential

$$\sigma_v(z) = \sigma_v^0(\vec{w})\mathrm{e}^{\frac{2z\kappa_e(\vec{w})}{cos\theta_r}} = \sigma_v^0(\vec{w})\mathrm{e}^{\frac{2z}{d_{pen}(\vec{w})}} \tag{4}$$

where z is the vertical (depth) axis, $cos\theta_r$ accounts for the off- vertical radar look vector, $\sigma_v^0(\vec{w})$ is the nominal backscatter power per unit volume and the extinction coefficient $\kappa_e(\vec{w})$ accounts for both scattering and absorption losses for a given polarization channel $\vec{w}$. Henceforth, we use the parameterization with one-way penetration depth d_{pen}, which is inversely related to κ_e through $\kappa_e = cos(\theta_r)/d_{pen}$. Simulations of γ_{Vol} for a uniform volume model lead always to a quasi-exponential coherence decrease (solid line in Fig. 8) and are given by [11]

$$\gamma_{vol} = e^{ik_z z_0}\frac{1}{1+\frac{id_{pen}(\vec{w})k_{zVol}}{2}}. \tag{5}$$

Additional scattering contributions from the surface, modelled as a Dirac delta function at depth 0 m, lead to the uniform volume under ground model [19] with one additional parameter, namely, the ground-to-volume ratio. This ratio defines the lower coherence limit which is asymptotically reached for larger k_{zVol} values (dashed line in Fig. 8).

In Section 2.2.4, we already discussed why the uniform volume and uniform volume under ground models (Fig. 8) cannot explain our measurements (Fig. 7). Therefore, we extend the uniform volume under ground model in order to account not only for additional scattering from the surface [16], but also scattering from layers within the firn volume.

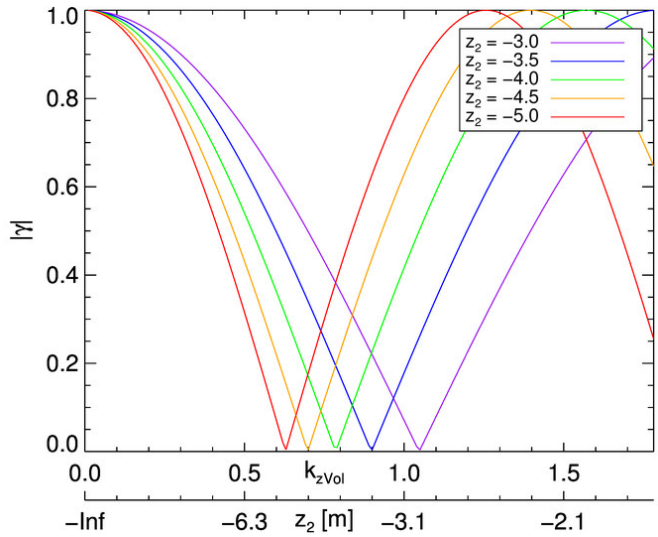

Fig. 9. Coherence magnitude simulations for two layers only with varying depth of the second layer. The first layer is at $z_1 = 0\,m$ and the depth of the second layer z_2 is varied between $-3\,m$ and $-5\,m$ as indicated by the colored lines. The scattering powers of the two layers are equal $\sigma_{L_1} = \sigma_{L_2} = 1$. The second x-axis is not a real x-axis, but indicates the depth of the second layer for a given position of the coherence minimum.

It is worth highlighting that the uniform volume model is used as a single-channel model without any assumptions on the polarization dependence of the volume scattering. A random volume scenario is obtained assuming the same one-way penetration depth d_{pen} for all polarizations $\vec{w}$ while an oriented volume scenario is given when d_{pen} is polarization dependent.

2.3.2 Two Layer Model

In the case of a simple vertical structure consisting of two equally strong layers (e.g., the snow-firn interface and one subsurface layer) without any volume contribution, their interference pattern leads to a periodic coherence magnitude undulation with k_{zVol} (Fig. 9). Neglecting multiple scattering, the interferometric coherence is given by

$$\gamma = e^{ik_z z_0} \frac{\sigma_{L_1}(\vec{w}) e^{ik_{zVol} z_1} + \sigma_{L_2}(\vec{w}) e^{ik_{zVol} z_2}}{\sigma_{L_1}(\vec{w}) + \sigma_{L_2}(\vec{w})} \tag{6}$$

with layer backscattering powers $\sigma_{L_{1,2}}(\vec{w})$ and layer depths $z_{1,2}$.

The minima positions are located at

$$k_{zVol} = n\pi/(z_1 - z_2) \tag{7}$$

with $n = 1,3,5, \ldots$, which is indicated in Fig. 9 by the second x-axis. The periodicity of the coherence minima is similar to the behavior observed not only at L-band (Fig. 7), but also at all

other frequencies at the South Dome site. Increasing the vertical distance between the two layers moves the coherence minimum position toward smaller k_{zVol} values.

While the distance between the layers drives the k_{zVol} positions of the minima and maxima, it does not affect the extrema values of the coherence magnitude. The coherence magnitude values are sensitive to the scattering powers of the layers $\sigma_{L_{1,2}}(\vec{w})$, which in turn do not affect the k_{zVol} position of the minima and maxima. According to (7), when the layer distance $z_1 - z_2$ becomes an even multiple of π/k_{zVol}, the two layers are in phase and the coherence reaches 1, independently of the individual $\sigma_{L_{1,2}}(\vec{w})$ values. On the contrary, the coherence magnitude at the minimum depends on the difference in scattering power of the layers. The layers interfere destructively if $z_1 - z_2$ is an odd multiple of π/k_{zVol} and the coherence drops to 0 for $\sigma_{L_1} = \sigma_{L_2}$. The coherence minimum increases with increasing contrast (i.e., difference in power) between the two layers with $|\gamma_{min}| = |\sigma_{L_1} - \sigma_{L_2}|/(\sigma_{L_1} + \sigma_{L_2})$. Accordingly, the coherence undulation is the same regardless whether the first or second layer is stronger as long as their difference is the same.

2.3.3 Layer plus Volume Model

In order to explain the overall low coherence values and the steep coherence drop at small k_{zVol} in Fig. 7, a volume decorrelation contribution needs to be considered additionally. The resulting vertical structure function is then given by the sum of (4) and Dirac delta functions δ for each of the N layers located at depth z_j with layer backscattering power $\sigma_{L_j}(\vec{w})$

$$\sigma_v(z) = \sigma_v^0(\vec{w})\mathrm{e}^{\frac{2z}{d_{pen}(\vec{w})}} + \sum_{j=1}^{N} \sigma_{L_j}(\vec{w})\, \delta(z_j). \tag{8}$$

The interferometric coherence is given by

$$\gamma = e^{ik_z z_0} \frac{\gamma_{Vol}(k_{zVol}, d_{pen}(\vec{w})) + \sum_{j=1}^{N} m_j(\vec{w}) e^{ik_{zVol} z_j}}{1 + \sum_{j=1}^{N} m_j(\vec{w})} \tag{9}$$

with $m_j(\vec{w}) = \sigma_{L_j}(\vec{w}) / \int \sigma_v^0(\vec{w})\mathrm{e}^{\frac{2z}{d_{pen}(\vec{w})}}$ being the layer-to-volume scattering ratio. $\gamma_{Vol}(k_{zVol}, d_{pen}(\vec{w}))$ is the coherence of a uniform volume model with infinite depth, as given in (5), but omitting the topographic phase of (5).

The predictions of such a combined model are shown in Fig. 10 for N = 2 and d_{pen}= 30 m. The layer-to-volume ratios m_j are fixed to 0.2 for the surface layer and ranges between 0.1 and 0.4 for the second layer located at -4.5 m depth. The simulated vertical structure is sketched in the inset. The following points are worth being mentioned:

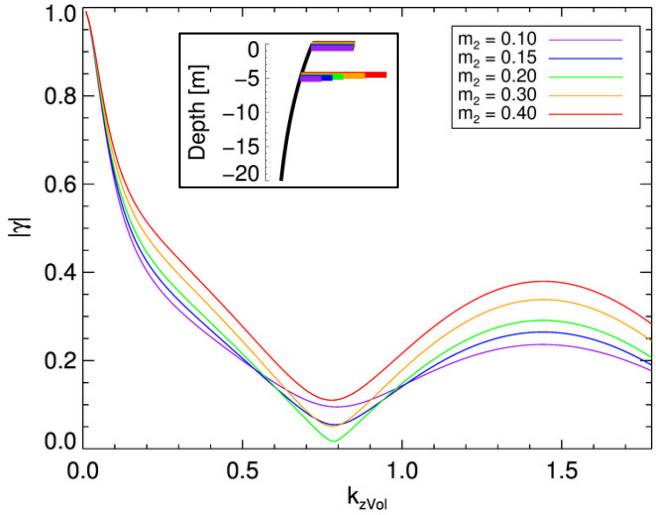

Fig. 10. Two layer plus uniform volume model. The layer-to-volume ratio m_1 of the first layer located at $z_1 = 0\,m$ is fixed to 0.2. The second layer is at $z_2 = -4.5\,m$ with m_2 varying between 0.1 and 0.4, as indicated by the colored lines. The volume is modelled by a uniform volume with infinite depth and one-way penetration of 30 m. The simulated vertical structure is sketched in the inset.

1) The fast drop of coherence magnitude with increasing k_{zVol} until the first minimum is mainly driven by the decorrelation of the volume component and becomes therefore stronger with increasing volume-only penetration depth.
2) The position of the first coherence minimum is largely determined by the vertical distance of the two layers, according to (7), with a small shift induced by the volume.
3) The coherence value at the minimum becomes lowest for $m_1 = m_2$.
4) The second coherence maximum γ_{max2} can be approximated by the sum of the layer-to-volume ratios through

$$|\gamma_{max2}| = \frac{\sum_{j=1}^{N} m_j}{1+\sum_{j=1}^{N} m_j} \tag{10}$$

because γ_{Vol} tends to zero for larger k_{zVol} (e.g. $|\gamma_{Vol}| < 0.05$ for $d_{pen} > 28$ m at $k_{zVol} = 1.4$ rad/m).

Under the assumption that the volume is already completely decorrelated at the first minimum of the undulation pattern, i.e. $\gamma_{Vol} = 0 + i0$, we can derive an approximation for the coherence value $|\gamma|$ at this first minimum. The minimum decreases for decreasing layer-to-volume ratio difference $|m_1 - m_2|$, as described for the two layer only case in Section 2.3.2. Additionally, the coherence value at the minimum is affected by the power of the layers compared to the volume leading to

$$|\gamma_{min}| = \frac{|m_1 - m_2|}{1+\sum_{j=1}^{N} m_j}. \tag{11}$$

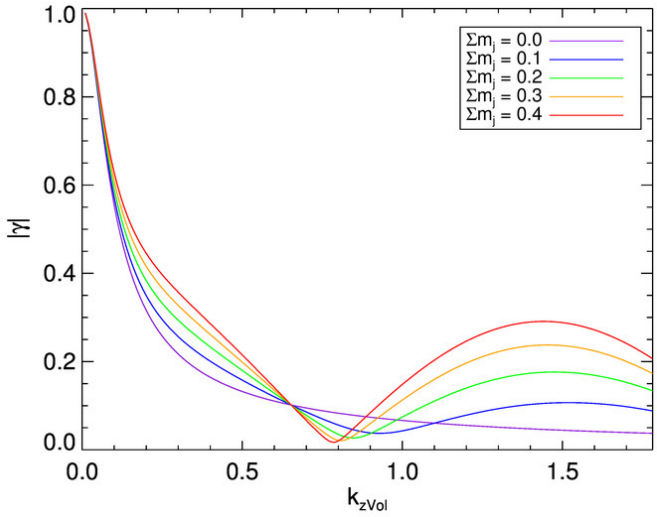

Fig. 11. Effect of the sum of layer-to-volume ratios $\sum m_j$ for a two layer plus volume model. Layer parameters are $m_1 = m_2; z_1 = 0, z_2 = -4.5\ m$. The sum of layer-to-volume ratios $\sum m_j$ varies between 0.0 and 0.4. The case of $\sum m_j = 0.4$ (red line) corresponds to $m_2 = 0.2$ in Fig. 10 (green line).

To further illustrate the model behavior, Fig. 11 shows the effect of the sum of the layer-to-volume ratios $\sum m_j$ for $m_1 = m_2$. The case of $\sum m_j$ = 0.4 (see red line in Fig. 11) corresponds to m_2 = 0.2 in Fig. 10 (green line). The effect of the layers, compared to the uniform volume model (purple line in Fig. 11), is clearly visible. The second coherence maximum is mainly driven by $\sum m_j$, while the position and the value of the coherence minimum are less sensitive to $\sum m_j$-changes above 0.2. Interestingly, the layers barely affect the coherences for k_{zVol} < 0.1 rad/m, but their effect is obvious between k_{zVol} = 0.1 rad/m and the coherence minimum. The volume influences the coherences starting from k_{zVol} = 0 rad/m. Accordingly, layers and volume similarly contribute to the coherence in the range 0.1 rad/m < k_{zVol} < 0.6 rad/m. At larger k_{zVol}, the effect of the volume is marginal.

The effect of an increasing number of layers needs to be analyzed when thinking about the firn structure at the test site [27] as indicated by the GPR data in Fig. 2. As explained in Section 2.3.2, the superposition of layers leads to undulations, where the periodicity in k_{zVol} direction is determined by the distance of the layers while the magnitude of the undulation is driven by the layer-to-volume ratios. Fig. 12 shows the effect of an additional weaker layer (0.02 < m_3 < 0.06) at a depth of z_3 = -20.5 m, which is visible in the GPR data in Fig. 2. This simulation roughly matches the higher order undulations of the data in Fig. 7. Thus, an increasing number of layers allows generating more complex coherence undulation patterns.

Note that even several layers would eventually constructively interfere after the first minimum, leading to higher coherence magnitudes than observed if no volume is considered.

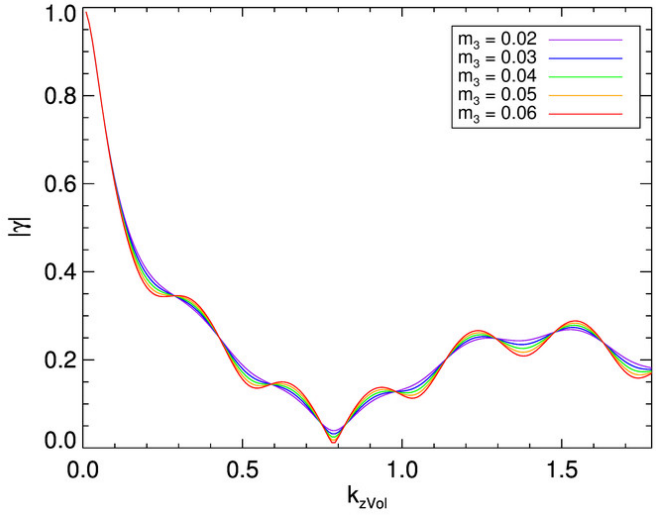

Fig. 12. Three layer plus uniform volume model. The first two layers are fixed at $m_1 = 0.2; m_2 = 0.15; z_1 = 0; z_2 = -4.5\,m$. The third layer is located at $z_3 = -20.5\,m$ with weaker powers m_3 varying between 0.02 and 0.06. The volume is modelled by a uniform volume with infinite depth and one-way penetration of 30 m.

2.3.4 Vertically Extended Subsurface Layers

Up to now, the scattering layers were considered to be Dirac delta functions at a certain depth z_j. There are several reasons, why a layer may have a vertical extent. In the percolation zone of Greenland, the formation of refrozen melt layers is complex and different mechanisms exist that lead to laterally continuous scattering layers [35]. Therefore, there is a chance that these layers are extended over a small depth range. Furthermore, large estimation windows are required to obtain an unbiased coherence estimation at low coherence values, likely associated with small changes in layer depth within their spatial coverage.

We assessed the influence of a layer extent d_j for each layer j. This leads, for each layer, to a sinc-like contribution [36] to the overall coherence, resulting theoretically in a widening of the coherence minima and a lowering of the maxima. However, for the first minimum the widening effect is negligible, even for a 2 m vertical extent of the layer at -4.5 m. The same is true for the coherence maxima. We therefore stick to the representation of layers with Dirac delta functions.

2.4 Results

2.4.1 Multifrequency Coherence Profiles

The multiple-layer-plus-volume model is now used to analyze the coherence profiles from the percolation zone of Greenland. Fig. 13 shows the dependence of the coherence magnitude $|\gamma|$ on the vertical wavenumber k_{zVol} averaged over the entire scene for six interferograms available at each frequency.

At P-band the HH and VV coherences are almost identical, which implies similar vertical structure functions, while HV has lower coherences and a less pronounced undulation. The second maximum shows the weaker layer contributions in HV as expected, which is true for all frequencies. The small difference between HH and VV in P-band for low k_{zVol} values could be an indication of a slightly oriented volume with different d_{pen} for HH and VV. This could be caused by polarization-dependent scattering in the firn and from ice inclusions which are not part of the layers. The lower coherence in HV is due to the lower HV layer-to-volume ratios according to our model.

At L-band, the minima at VV are lower than at HH, which means, according to (11), that the $|m_1 - m_2|$ layer difference is smaller at VV. The second coherence maximum is almost equal in HH and VV, which implies that the sum of layer-to-volume ratios $\sum m_j$ is similar, according to (10). L-band shows also a higher order undulation which may indicate the presence of a third layer.

The S-band profiles show also an undulation, but not as pronounced as at the other frequencies. Also the minimum positions for HH and VV seem to be at different k_{zVol} values. The very wide coherence minima could be explained by vertically extended layers (see Section 2.3.4) but would require unrealistically large vertical distributions of the layer structure functions.

A clear minimum is present at C-band in HH, but is less pronounced in VV. Interestingly, the minima appear at higher k_{zVol} values than for the P- and L-band frequencies, indicating scattering contributions from a shallower subsurface layer.

Finally, the X-band profiles have a well pronounced coherence undulation with a clearly visible second minimum. HH and VV maxima are similar, indicating similar sums of layer-to-volume ratios $\sum m_j$, but at VV the difference between the two layers is smaller.

2.4.2 Layer Depth Dependence on Frequency

Using the relationship between layer spacing and minimum position of the coherence profiles in (7), and neglecting a small shift introduced from the volume coherence, we can calculate the depth of the second layer by assuming the first layer to be at $z_1 = 0\,m$. Looking only at the dominant minima at each frequency in Fig. 13, the second layer is estimated to be roughly at -3.0 m at C- and X-bands and -4.75 m at P- and L-bands. At S-band, the minima positions are different across polarizations. The VV and HV minimum position is approximately at k_{zVol} = 0.7 rad/m which corresponds to -4.5 m, similar to L- and P-bands. Contrarily, the HH minimum position is roughly at k_{zVol} = 1.0 rad/m, which corresponds to a layer depth of -3.1 m, similar to C- and X-bands. Even though it is not clear why the polarizations behave differently at S-band, it seems that S-band is like a transition frequency for the particular vertical subsurface structure at South Dome.

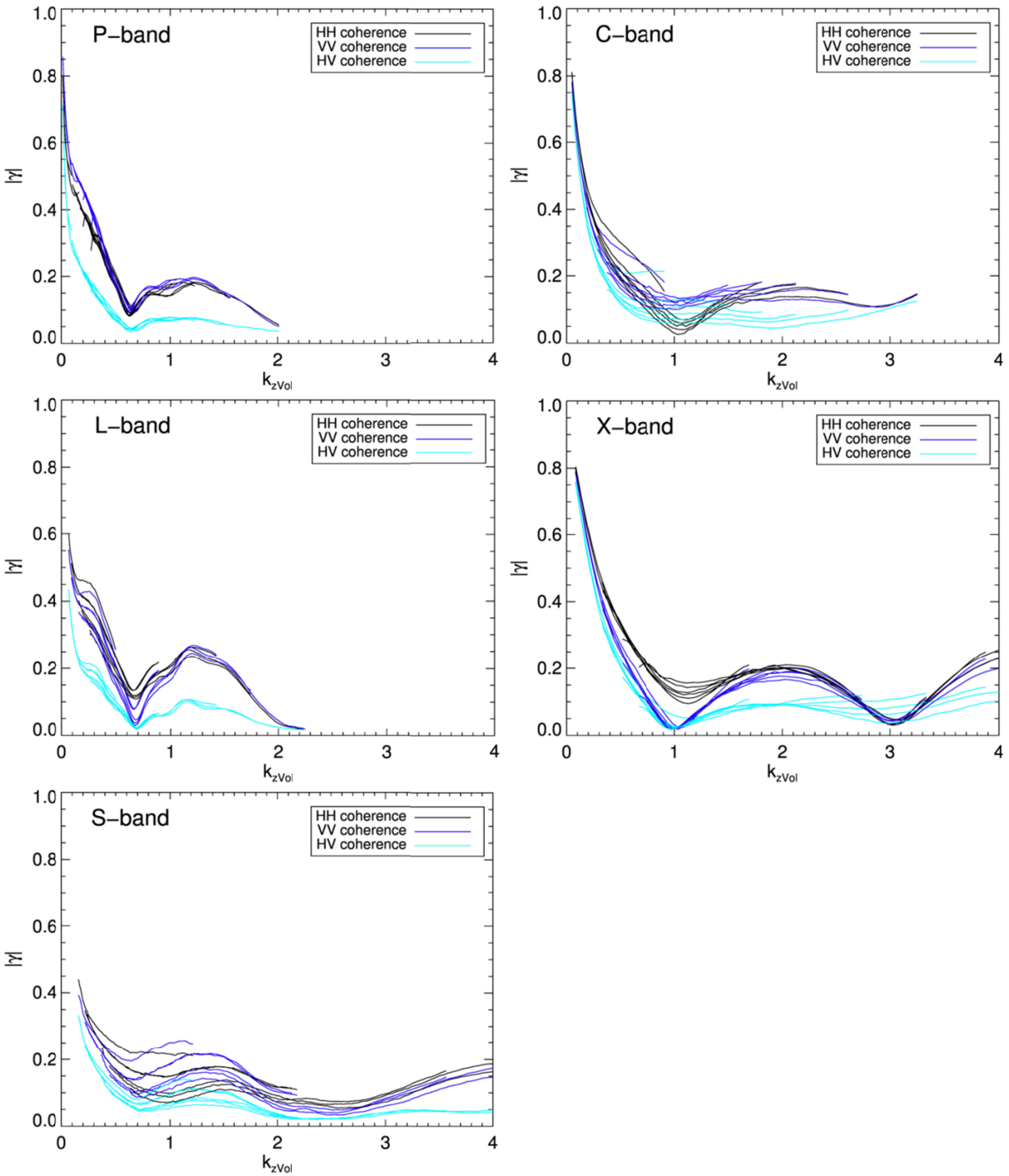

Fig. 13. Coherence profiles at P-, L-, S-, C-, and X-bands for South Dome over k_{zVol} for six different horizontal baselines. HH, VV, and HV profiles are depicted in black, blue, and cyan, respectively. The vertical spread at each polarization is related to the fact that the same k_{zVol} values correspond to different incidence angles for different baselines. The x-axis is extended compared to Fig. 7.

A layer located at -4.75 m, as indicated by the P- and L-band data, fits well to the dominant layer at -4.5 m in the GPR data (Fig. 2). Note that the volume contribution introduces also a small shift in the minimum position, which can lead to an underestimation of layer depth of e.g. 0.5 m for $d_{pen} = 30\ m$. This shift becomes smaller with larger d_{pen}.

TABLE I
SUM OF LAYER-TO-VOLUME SCATTERING RATIOS $\sum m_j$

$\sum m_j$	HH	VV	HV
P	0.23	0.25	0.09
L	0.34	0.35	0.12
S	0.17	0.22	0.10
C	0.19	0.20	-
X	0.25	0.22	0.10

Average sum of layer-to-volume scattering ratios $\sum m_j$ approximated from the coherence profiles in Fig. 13 with (10) (mean values from Fig. 14). For C-band HV no value is derived because the coherence profiles do not have a clear second coherence maximum.

In case, the first scattering layer is not at the surface, i.e., the snow-firn interface, the layers visible at -4.75 m and -10.0 m in the GPR data, could also explain the coherence undulation at L- and P-band, because they have approximately the required vertical distance to produce the observed undulation periodicity.

The higher frequencies, particularly C- and X-bands, indicate a subsurface layer at -3.0 m, which is not visible in the GPR data. Possible reasons for this are the limited vertical resolution of the GPR and the fact that it is operated at P-band. Thus, we use our manual layer probing measurements to better assess the near surface layering. The only consistently detected layer was located at -3 m depth and was sometimes not even permeable with the probe (see Fig. 3). While all other layers were permeable with one thrust, the layer at -3 m had a significant vertical extent. This observation fits to the necessity of a scattering layer at -3 m to explain the C- and X-band profiles. Despite being within the penetration depth of P- and L-bands, the effect of this layer is barely visible at these frequencies, which might be related to the longer wavelengths since the layer is also not visible in the (P-band) GPR data.

2.4.3 LAYER-TO-VOLUME SCATTERING RATIO DEPENDENCE ON POLARIZATION

The polarization dependence in the data is primarily due to the layer-to-volume ratios m_j according to the layer plus volume model. A potential polarization dependence of the volume (i.e., an oriented volume) is barely indicated and is discussed in Section 2.4.4. Only at S-band, there seems to be an additional polarization sensitivity to the layer depth z_j as described above. The simulations in Section 2.3 show that there are two key parameters that describe the coherence profiles if only two layers are assumed: first, the normalized difference of layer-to-volume scattering ratios $|m_1 - m_2|$, and second the sum of the layer-to-volume ratios $\sum m_j$.

$\sum m_j$ directly affects the second coherence maximum. At these k_{zVol} values, it is fair to assume that the volume coherence is very close to zero. In this case, we can directly infer the sum of layer ratios from the plots (see Table I) through (10). The HV layer scattering ratios are by a factor of 1.7-2.9 lower than at co-pol channels, while HH and VV are very similar. An

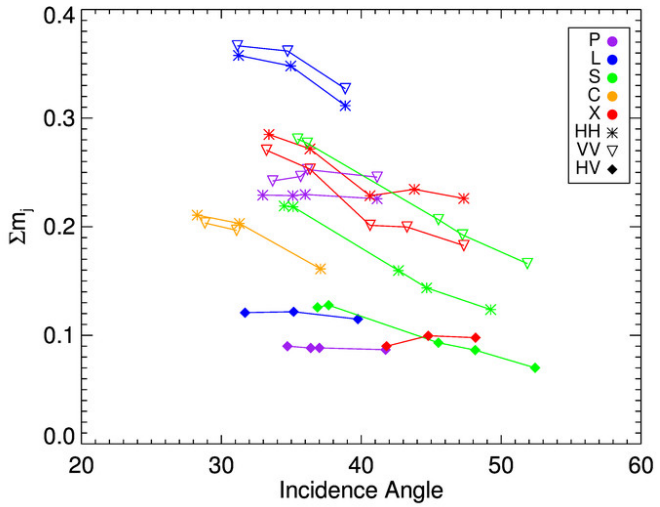

Fig. 14. Sum of layer-to-volume scattering ratios $\sum m_j$ derived from the InSAR coherence profiles in Fig. 13 with (10) over incidence angle. The spread across incidence angles comes from the fact that for a given second coherence maximum, the corresponding k_{zVol} value is at a different incidence angle for different horizontal baselines. Values are only extracted for profiles with a clear second coherence maximum.

exception is here again the S-band, where the different polarizations also seem to be sensitive to different layers.

Furthermore, the sum of layer-to-volume ratios $\sum m_j$ is derived for different incidence angles, because the second coherence maxima found at a certain k_{zVol} value correspond to different incidence angles for different horizontal baselines. The incidence angle dependence of $\sum m_j$ is shown in Fig. 14, where only coherence profiles with a clear second maximum have been considered.

Additional to the general pattern of stronger layer-to-volume ratios in the co-pol than in the cross-pol channels, the decrease of layer backscattering with increasing incidence angle is well pronounced. This trend is equally strong for HH and VV, while there are no changes at HV. Only at P-band, the layer-to-volume ratios appear stable over the whole incidence angle range for all polarizations.

Unfortunately, the layer scattering ratios cannot be directly validated. Nevertheless, the observed differences between the co and cross-pol channels and the trends with incidence angle fit to the expected behavior if layer scattering is considered as a rough surface scattering mechanism and given that volume scattering has marginal sensitivity to incidence angle variations [33].

The behavior of layer scattering ratios with incidence angle is in agreement with the qualitative assessment of scattering mechanisms in Section 2.2.3. Polarimetric entropy and alpha parameters (Fig. 4) indicate the decrease of surface scattering with incidence angle, which leads to an increase of the relative strength of volume scattering.

Another observation is that for the frequencies sensitive to the same layer (i.e., P- and L-bands at -4.75 m; C- and X-bands at -3.0 m under the assumption of z_1 = 0 m), higher layer-to-volume ratios are retrieved for higher frequencies.

The simulations in Section 2.3.3 show that the layer-to-volume ratios do not only directly affect the magnitude of the second coherence maxima, but also the coherences at smaller k_{zVol}, even before the first minimum (Fig. 10 and Fig. 11). This is also reflected by the profiles from shorter baselines in Fig. 13 that have slightly higher coherence magnitudes. For a given k_{zVol}, these profiles correspond to steeper incidence angles, and therefore to larger layer-to-volume ratios, as shown in Fig. 14. The effect is stronger at L-, S-, and C-bands.

2.4.4 VOLUME COHERENCE

The volume contribution is visible in the generally fast drop of coherence values at k_{zVol} < 0.1 rad/m in Fig. 13. At L- and S-band this part of the profile cannot be completely presented because of the lack of very small k_{zVol}. At P-, C-, and X-bands, the available horizontal baselines are small enough to have coherences starting almost at k_{zVol} = 0 rad/m.

There is a slight trend of weaker volume decorrelation with increasing frequency confirming less volume penetration at X-band compared to C-band.

At C- and X-bands, the coherences are similar across all polarizations for k_{zVol} < 0.1 rad/m, which could be interpreted as equal d_{pen} for all polarizations (i.e., random volume) based on the findings from Fig. 11, because the layers have negligible impact for k_{zVol} < 0.1 rad/m. The same could be speculated for L- and S-bands, but coherences at k_{zVol} < 0.1 rad/m are not available. On the contrary, the polarization differences of the coherence profiles at P-band at small k_{zVol} could indicate an oriented volume with different d_{pen} for HH and VV.

2.4.5 MODEL FIT

From the six baselines at L-band in Fig. 13, we extracted a synthetic average coherence profile and fit a three layer plus volume model to the data independently for each polarization, as shown in Fig. 15. The possibility for a third layer (i.e., second subsurface layer) was added to account for the higher order undulations in the profile. The first layer was assumed to be at z_1 = 0 m. The simulations agree well with the general behavior of the L-band coherence profiles, but lack a precise representation of the higher order undulations.

Table II summarizes the parameters obtained by the model fit. The locations of the two subsurface layers at z_2 = -5.1 m and z_3 = -21.3 m agree well, with a mismatch of only 0.1 m and 1.2 m, respectively, across polarizations, and show only small differences to the layers at -4.5 m and -20.5 m in the GPR data in Fig. 2. No contribution of a third layer was obtained at HV.

Interestingly, the second layer is stronger than the surface in VV, which leads to a similar undulation pattern as in HH, where the difference of layer-to-volume ratios m_1 and m_2 is identical. It is described in Section 2.3.2 that the undulation pattern is mainly driven by the layer difference, regardless of which of them is stronger. Layers for HV and the third layer in the co-pol channels are about one order of magnitude weaker.

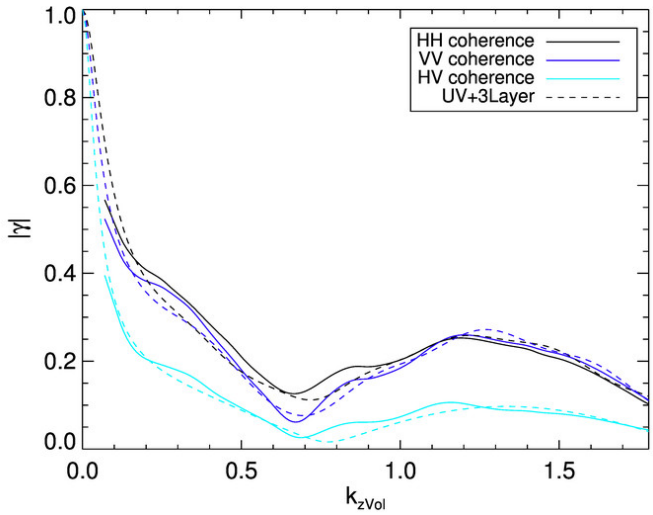

Fig. 15. Three layer plus uniform volume model (dashed lines) fitted to a synthetic mean coherence profile (solid lines) generated for each polarization from six baselines at L-band.

TABLE II
PARAMETERS OF THE THREE LAYERS PLUS UNIFORM VOLUME MODEL FITTED TO THE SYNTHETIC AVERAGE COHERENCE PROFILE AT L-BAND.

	HH	VV	HV
z_1 [m]	0	0	0
z_2 [m]	-5.1	-5.1	-5.0
z_3 [m]	-21.3	-20.1	-
m_1	0.23	0.11	0.05
m_2	0.10	0.24	0.05
m_3	0.007	0.015	0.0
pen. depth [m]	32	45	60

The one-way penetration depth values appear very large, but one has to consider that this is the parameter of the volume-only model. The combined penetration depth is shallower due to the layer contributions. The penetration depths differ with polarization, which is an indication for an oriented volume scenario. But the lack of data with $k_{zVol} < 0.1$ rad/m, where the volume contribution can be best assessed (see Section 2.4.4), hampers a clear assessment of the random versus oriented volume question. Theoretically, the HV penetration depth has to be in between the values for HH and VV in an oriented volume scenario, which is not the case for the results of the model fit. This could indicate a different vertical distribution of backscattered power of the volume at HV, which cannot be interpreted by a uniform volume model.

2.5 DISCUSSION AND CONCLUSION

In this paper, a scattering model for Pol-InSAR coherences from the percolation zone in Greenland has been proposed and validated. We observed a coherence undulation with vertical wavenumber k_{zVol} in our data that cannot be explained with existing uniform volume only [11] or volume under ground [19] models. For this, the presence of subsurface layers is required.

Simulations show how the layered vertical structure below the surface affects the InSAR coherences due to the constructive and destructive interference of the layer contributions leading to pronounced coherence minima and maxima in dependence of k_{zVol}. At all frequencies, two layers are enough to interpret the main coherence magnitude behavior. Only at L-band, a higher order undulation is present that can be described by a third, deeper layer.

Furthermore, the simulations also reveal the potential to estimate and characterize subsurface layers from InSAR coherences. Under the assumption of the first layer being located at the surface, we can interpret the data, by comparison with forward simulations, with a second layer at -4.75 m at P- and L-bands and at -3.0 m for C- and X-bands, which is supported by in situ data. A model fit to the L-band data indicates a second layer at -5.1 m, which is considered a good agreement given that the model fit shows small deviations from the data. The situation at S-band is less clear and seems to be a transition between the other frequencies.

Also layer-to-volume scattering ratios can be inferred from the measured coherences, potentially revealing the relative importance of different scattering mechanisms. As expected, cross-pol layer-to-volume scattering ratios are smaller than at co-pol channels throughout the data set, but a subsurface layer is still necessary to explain the undulations at HV. The VV layer scattering ratios are slightly larger than at HH for most frequencies, but the differences can be as small as 3 %.

The validation is mainly limited to layer depths, which can be inferred from our in situ measurements, since manually measured layer thickness or GPR signals cannot directly be used to validate layer-to-volume ratios based on SAR data. Furthermore, it is not yet completely understood which layers detected in a GPR profile are dominant enough to have an impact on InSAR coherences.

We generally conclude that ice sheet areas exist where the assumptions of a uniform volume or uniform volume under ground scenario are not valid. However, the overall low coherence magnitudes and the retrieved layer-to-volume scattering ratios demonstrate the overall dominance of volume scattering, which is supported by polarimetric analyses and is also consistent with [11] and [16]. Despite that, we show clear evidence that dominant subsurface layers have to be taken into account.

The inversion of the proposed model has not been addressed here as it goes beyond the scope of this paper, but will strongly depend on the observation scenario as well as on the subsurface characteristics of the area under investigation. The simplest case is a two-layer plus volume model, where the first layer is assumed to be at the surface and the volume is independent of the polarization (i.e., random volume). The resulting nine model parameters could be theoretically inverted with a dual-baseline Pol-InSAR setup providing 12 independent observables. There is potential in combining observations at small k_{zVol}, which are mainly sensitive to the volume, and at larger k_{zVol}, which are mainly sensitive to the layer contributions. Such an inversion scheme remains to be established. Any additional layer or a polarization-dependent volume (i.e., oriented volume) add at least two parameters and will complicate the inversion. For comparison, single-pol single-baseline data allow only the inversion of a uniform volume model without any layers. Full-pol single-baseline data improve the inversion capability to, e.g., a random volume

under ground model, but the existence of a second layer requires dual-baseline data for any inversion, as described above.

In the percolation zone of Greenland, distinct subsurface layers are related to refreezing of melt water. Therefore, the analysis of coherence patterns could support the assessment of accumulation rates, density changes or melt-refreeze processes. Starting from a clear melt layer structure as we observed at South Dome, the effect of such dominant layers within the firn body is expected to differ for areas with less or no melting during summer toward the dry snow zone. The explicit modeling of depth hoar layers within firn in the dry snow zone of Greenland by Oveisgharan and Zebker [13] relied on a priori information and was compared to accumulation rates from firn cores. Unfortunately, it was impossible to acquire data in the dry snow zone during the ARCTIC15 campaign to see if we could show an effect of a layered subsurface structure directly on a data level as we did for the percolation zone. In addition, in the other direction, with increasing melt periods, refrozen ice inclusions within the firn can become so abundant that no distinct layers could be present and the vertical structure could be interpreted again with volume scattering models. Therefore, one model seems not to be enough for the interpretation of Pol-InSAR data over different glacier zones of ice sheets, an approach which was already followed by [10] for PolSAR.

The potential to retrieve geophysical information about dominant subsurface layers was validated with in situ data, indicating that Pol-InSAR data could be exploited in the future for space borne retrieval of ice sheet subsurface structure. Further studies are necessary to investigate how a retrieval with a limited number of acquisitions can be achieved.

2.6 ACKNOWLEDGMENT

The authors would like to thank everyone involved in the ARCTIC15 campaign, which was conducted by DLR, Wessling, Germany, and ETH Zurich, Zurich, Switzerland, in cooperation with the Danish Defence Acquisition and Logistics Organization, Ballerup, Denmark, and the Alfred-Wegener-Institute, Bremerhaven, Germany, for providing the GPR system and general support for the campaign. They would also like to thank the anonymous reviewers for the valuable and constructive comments, which improved both clarity and quality of this paper.

2.7 REFERENCES

[1] D.G. Vaughan, J.C. Comiso, I. Allison, J. Carrasco, G. Kaser, R. Kwok, P. Mote, T. Murray, F. Paul, J. Ren, E. Rignot, O. Solomina, K. Steffen, and T. Zhang, “Observations: Cryosphere,” in *Climate Change 2013: The Physical Science Basis. Contribution of Working Group I to the Fifth Assessment Report of the Intergovernmental Panel on Climate Change,* [Stocker, T.F., D. Qin, G.-K. Plattner, M. Tignor, S.K. Allen, J. Boschung, A. Nauels, Y. Xia, V. Bex and P.M. Midgley (eds.)]. Cambridge University Press, Cambridge, United Kingdom and New York, USA, 2013.

[2] A. S. Gardner, G. Moholdt, J. G. Cogley, B. Wouters, A. A. Arendt, J. Wahr, E. Berthier, R. Hock, W. T. Pfeffer, G. Kaser, S. R. M. Ligtenberg, T. Bolch, M. J. Sharp, J. O. Hagen, M. R. van den Broeke, F. Paul, "A reconciled estimate of glacier contributions to sea level rise: 2003 to 2009," *Science*, vol. 340, pp. 852–857, May 2013.

[3] R. Forster, K. C. Jezek, J. Bolzan, F. Baumgartner, and S. P. Gogineni, "Relationships between radar backscatter and accumulation rates on the Greenland ice sheet," *International Journal of Remote Sensing*, vol. 20, nos. 15-16, pp. 3131–3147, Jan. 1999.

[4] G. Rotschky, W. Rack, W. Dierking, and H. Oerter, "Retrieving snowpack properties and accumulation estimates from a combination of SAR and scatterometer measurements," *IEEE Transactions on Geoscience and Remote Sensing*, vol. 44, no. 4, pp. 943–956, Apr. 2006.

[5] M. Fahnestock, R. Bindschadler, R. Kwok, and K. Jezek, "Greenland ice sheet surface properties and ice dynamics from ERS-1 SAR imagery," *Science*, vol. 262, no. 5139, pp. 1530–1534, Dec. 1993.

[6] K. C. Jezek, M. R. Drinkwater, J. P. Crawford, R. Bindschadler, and R. Kwok, "Analysis of synthetic aperture radar data collected over the southwestern Greenland ice sheet," *Journal of Glaciology*, vol. 39, no. 131, pp. 119–132, Jan. 1993.

[7] E. J. Rignot, S. Ostro, J. J. van Zyl, and K. C. Jezek, "Unusual radar echoes from the Greenland ice sheet," *Science*, vol. 261, no. 5129, pp. 1710–1713, Sep. 1993.

[8] E. J. Rignot, "Backscatter model for the unusual radar properties of the Greenland ice sheet," *Journal of Geophysical Research*, vol. 100, no. E5, pp. 9389–9400, May 1995.

[9] J. J. Sharma, I. Hajnsek, K. P. Papathanassiou, and A. Moreira, "Polarimetric decomposition over glacier ice using long-wavelength airborne PolSAR," *IEEE Transactions on Geoscience and Remote Sensing*, vol. 49, no. 1, pp. 519–535, Jan. 2011.

[10] G. Parrella, I. Hajnsek, and K. P. Papathanassiou, "Polarimetric decomposition of L-band PolSAR backscattering over the Austfonna ice cap," *IEEE Transactions on Geoscience and Remote Sensing*, vol. 54, no. 3, pp. 1267–1281, Mar. 2016.

[11] E. W. Hoen and H. Zebker, "Penetration depths inferred from interferometric volume decorrelation observed over the Greenland ice sheet," *IEEE Transactions on Geoscience and Remote Sensing*, vol. 38, no. 6, pp. 2571–2583, Nov. 2000.

[12] E. Rignot, K. Echelmeyer, and W. Krabill, "Penetration depth of interferometric synthetic-aperture radar signals in snow and ice," *Geophysical Research Letters*, vol. 28, no. 18, pp. 3501–3504, Sep. 2001.

[13] S. Oveisgharan and H. A. Zebker, "Estimating snow accumulation from InSAR correlation observations," *IEEE Transactions on Geoscience and Remote Sensing*, vol. 45, no. 1, pp. 10–20, Jan. 2007.

[14] P. Rizzoli, M. Martone, H. Rott, and A. Moreira, "Characterization of snow facies on the Greenland ice sheet observed by TanDEM-X interferometric SAR data," *Remote Sensing,* vol. 9, no. 4, p. 315, Mar. 2017.

[15] S.R. Cloude and K.P. Papathanassiou, "Polarimetric SAR interferometry," *IEEE Transactions on Geoscience and Remote Sensing*, vol. 36, no. 5, pp. 1551-1565, Sep. 1998.

[16] J. Sharma, I. Hajnsek, K.P. Papathanassiou, and A. Moreira, "Estimation of glacier ice extinction using long-wavelength airborne Pol-InSAR," *IEEE Transactions on Geoscience and Remote Sensing*, vol. 51, no. 6, pp. 3715-3732, Jun. 2013.

[17] O. Stebler, A. Schwerzmann, M. Luthi, E. Meier, and D. Nuesch, "Pol-InSAR observations from an Alpine glacier in the cold infiltration zone at L- and P-band," *IEEE Geoscience and Remote Sensing Letters*, vol. 2, no. 3, pp. 357-361, Jul. 2005.

[18] T. Nagler, H. Rott, I. Hajnsek, K.P. Papathanassiou, and R. Scheiber, "An airborne experiment on snow parameter retrieval by means of multi-channel SAR data," in *Proceedings of EUSAR*, Dresden, Germany, May 2006, pp 1-4.

[19] J. Dall, K.P. Papathanassiou, and H. Skriver, "Polarimetric SAR interferometry applied to land ice: Modeling," in *Proceedings of EUSAR*, Ulm, Germany, 2004, pp. 247-250.

[20] S. Leinss, G. Parrella, and I. Hajnsek, "Snow height determination by polarimetric phase differences in X-band SAR data," *IEEE Journal of Selected Topics in Applied Earth Observations and Remote Sensing*, vol. 7, no. 9, pp. 3794–3810, Jun. 2014.

[21] K. Sainath and S. Hensley, "Numerical modeling of subsurface layer resonance-based interferometric SAR (InSAR) correlation fluctuations," in *Proceedings of EUSAR*, Hamburg, Germany, Jun. 2016, pp. 567-572.

[22] G. Fischer, G. Parrella, K. P. Papathanassiou, and I. Hajnsek, "Interpretation of Pol-InSAR signatures from glaciers and ice sheets at different frequencies," in *Proceedings of EUSAR*, Hamburg, Germany, Jun. 2016, pp. 806-811.

[23] E. W. Hoen, "A correlation-based approach to modeling interferometric radar observations of the Greenland ice sheet," Ph.D. dissertation, Dept. Appl. Phys., Stanford Univ., Stanford, CA, USA, Mar. 2001.

[24] R. Horn, A. Nottensteiner, and R. Scheiber, "F-SAR – DLR's advanced airborne SAR system onboard DO228," in *Proceedings of EUSAR*, Friedrichshafen, Germany, Jun. 2008, pp. 195-198.

[25] I. Hajnsek, K. P. Papathanassiou, and S. R. Cloude, "Removal of additive noise in polarimetric eigenvalue processing," in *Proceedings of IGARSS*, Sydney, NSW, Australia, 2001, pp. 2778–2780.

[26] A. Reigber, "Range dependent spectral filtering to minimize the baseline decorrelation in airborne SAR interferometry," in *Proceedings of IGARSS,* Hamburg, Germany, 1999, pp. 1721–1723.

[27] J. Freitag, S. Kipfstuhl, S. Hoerz, L. Eling, B. Vinther, and T. Popp, "Melt layer statistic of two firn cores recently drilled at Dye3 and South Dome in the dry snow zone of Southern Greenland," presented at the *EGU General Assembly*, Vienna, Austria, Apr./May, 2014.

[28] H. M. Jol, *Ground Penetrating Radar Theory and Applications.* Amsterdam, The Netherlands: Elsevier, 2009.

[29] C. Leuschen, "IceBridge accumulation radar L1B geolocated radar echo strength profiles, version 2," subset 8 Apr. 2014 05_016, *Nat. Snow Ice Data Center*, Boulder, CO, USA, 2015. [Online]. Available: https://nsidc.org/data/iracc1b, doi: 10.5067/0ZY1XYHNIQNY.

[30] S.L. Buchardt, H.B. Clausen, B. M. Vinther, and D. Dahl-Jensen, "Investigating the past and recent δ^{18}O-accumulation relationship seen in Greenland ice cores," *Climate of the Past*, vol. 8, no. 6, pp. 2053–2059, Dec. 2012.

[31] C. Leuschen, "IceBridge snow radar L1B geolocated radar echo strength profiles, version 2," subset 10 Apr. 2015 01_116, *Nat. Snow Ice Data Center*, Boulder, CO, USA, 2016. [Online]. Available: https://nsidc.org/data/irsno1b, doi: 10.5067/FAZTWP500V70.

[32] K. Steffen, J. E. Box, and W. Abdalati, "Greenland climate network: GC-net," in *CRREL 96-27 Special Report on Glaciers, Ice Sheets and Volcanoes,* S. C. Colbeck, Ed., Hanover,

NH, USA: U.S. Army Cold Regions Research and Engineering Laboratory, 1996, pp. 98-103.

[33] S. Cloude, *Polarisation: Applications in Remote Sensing*, New York, NY, USA. Oxford Univ. Press, 2010.

[34] C. Mätzler, "Applications of the interaction of microwaves with the natural snow cover," *Remote Sensing Reviews*, vol. 2, pp. 259-387, 1987.

[35] T. Dunse, O. Eisen, V. Helm, W. Rack, D. Steinhage, and V. Parry, "Characteristics and small-scale variability of GPR signals and their relation to snow accumulation in Greenland's percolation zone," *Journal of Glaciology*, vol. 54, no. 185, pp. 333-342, Mar. 2008.

[36] S. R. Cloude and K. P. Papathanassiou, "Three-stage inversion process for polarimetric SAR interferometry," *IEE Proceedings - Radar, Sonar and Navigation*, vol. 150, no. 3, pp. 125-134, Jun. 2003.

3 MODELING THE VERTICAL BACKSCATTERING DISTRIBUTION IN THE PERCOLATION ZONE OF THE GREENLAND ICE SHEET WITH SAR TOMOGRAPHY

G. Fischer, M. Jäger, K. P. Papathanassiou, and I. Hajnsek

IEEE Journal of Selected Topics in Applied Earth Observations and Remote Sensing

Submitted May 2019, Accepted October 2019.

This chapter is a pre-print of the accepted paper.

The author's contributions:

- Tomographic processing and analysis of the SAR data.
- Suggestion, implementation, and assessment of the models.
- Analysis and interpretation of the tomographic profiles and the model performance.
- Writing of the manuscript.

The co-authors' contributions:

- M. Jäger is the main developer of the SAR processor and was responsible for the accurate interferometric multi-baseline phase calibration of the SAR data.
- I. Hajnsek and K. P. Papathanassiou provided guidance throughout the research.
- K. P. Papathanassiou had the idea for the polarimetric assessment of the tomographic profiles and helped in the interpretation of the profiles and the model performance.
- I. Hajnsek and K. P. Papathanassiou contributed to the main ideas, the discussion of the results, and reviewed the manuscript.

MODELING THE VERTICAL BACKSCATTERING DISTRIBUTION IN THE PERCOLATION ZONE OF THE GREENLAND ICE SHEET WITH SAR TOMOGRAPHY

Georg Fischer[1,2], Marc Jäger[1], Konstantinos P. Papathanassiou[1], and Irena Hajnsek[1,2]
[1] German Aerospace Center, Microwaves and Radar Institute, Wessling, Germany
[2] ETH Zurich, Institute of Environmental Engineering, Zurich, Switzerland

Abstract

The penetration of microwave signals into snow and ice, especially in dry conditions, introduces a bias in digital elevation models generated by means of synthetic aperture radar (SAR) interferometry. This bias depends directly on the vertical backscattering distribution in the subsurface. In addition, the sensitivity of interferometric SAR measurements on the vertical backscattering distribution provides the potential to derive information about the subsurface of glaciers and ice sheets from SAR data, which could support the assessment of their dynamics. The aim of this paper is to improve the interferometric modeling of the vertical backscattering distribution to support subsurface structure retrieval and penetration bias estimation. Vertical backscattering distributions are investigated at different frequencies and polarizations on two test sites in the percolation zone of Greenland using fully polarimetric X-, C-, L-, and P-band SAR data. The vertical backscattering distributions were reconstructed by means of SAR tomography and compared to different vertical structure models. The tomographic assessment revealed that the subsurface in the upper percolation zone is dominated by scattering layers at specific depths, while a more homogeneous scattering structure appears in the lower percolation zone. The performance of the evaluated structure models, namely an exponential function with a vertical shift, a Gaussian function and a Weibull function, is evaluated. The proposed models improve the representation of the data compared to existing models while the complexity is still low to enable potential model inversion approaches. The tomographic analysis and the model assessment is therefore a step forward towards subsurface structure information and penetration bias estimation from SAR data.

3.1 INTRODUCTION

Understanding the dynamics of ice sheets and their mass balance is important for climate change research and sea level rise projections [1]. One important element in mass balance estimations is the derivation of volume changes from digital elevation models (DEM) generated with synthetic aperture radar interferometry (InSAR) [2], laser altimetry [3] and radar altimetry [4]. Despite the clear advantages of InSAR, namely the large coverage, high spatial resolution

and all-year, weather independent acquisitions, an inherent elevation bias affects the InSAR DEMs due to the penetration of the microwave signals into dry snow, firn and ice. The penetration bias is defined as the difference between the actual surface and the interferometric phase center derived from InSAR. The bias depends on the vertical distribution of the backscattered power in the subsurface and varies with the snow, firn and ice conditions (e.g. density or temperature), as well as with polarization, frequency and the interferometric baseline [5]. A large range of values has been reported for this bias, e.g. -1 m to -10 m at X-band (in the transition from the percolation to the dry snow zone in Greenland) [2] and -14 m at L-band (Greenland Summit) [6], with rare cases down to 120 m (cold marginal ice) [6]. Since the bias, and its temporal change, can be larger than the measured surface elevation change in e.g. a one year time span, its assessment and compensation becomes essential.

At the same time, the penetration of microwaves into dry snow, firn and ice makes it possible to derive information about the subsurface structure of ice sheets and its dynamics from InSAR data. This could provide information about e.g. density changes in firn due to melt-refreeze processes, which represent an uncertainty in mass balance estimation and that can usually only be addressed by field measurements [1], [3].

The interferometric coherence depends on the vertical backscattering distribution and thus on the vertical subsurface structure of ice sheets. The latter is therefore also directly linked to the penetration bias of InSAR DEMs, because it determines the phase center depth of the interferometric coherence below the surface. However, the interpretation of the scattering behavior of different subsurface elements and thus their contribution to the vertical backscattering distribution is not always clear. For instance, fresh snow and even firn can be transparent, particularly at longer wavelengths, while ice lenses from refrozen melt water contribute strongly to the backscattered signal.

Therefore, the estimation of the penetration bias as well as the estimation of parameters related to the subsurface structure require models for the vertical backscattering distribution in glaciers and ice sheets.

Hoen & Zebker [7] modelled the vertical backscattering distribution as a uniform lossy volume with constant extinction and infinite depth for C-band data in Greenland. This leads to an exponential backscattering distribution, where the extinction coefficient is related to the geophysical subsurface characteristics and the penetration bias. This uniform volume (UV) model was used in [8] for the characterization of different glacier zones in Greenland. A next step was the combination of a UV model with a surface scattering component, also known as Random Volume under Ground model [9]. In this context, an extinction inversion scheme by means of polarimetric SAR interferometry (Pol-InSAR) was established and applied to L- and P-band data from Svalbard [10]. A similar formulation with not only a surface contribution on top of a UV, but also a boundary below the volume, in the sense of a snow-firn interface, was used in [11] to describe Ka-band penetration into the snow cover at Greenland's summit.

While these approaches showed the potential to estimate penetration and subsurface characteristics, they cannot adequately capture different scattering scenarios that occur within ice sheets because they are limited by the assumption of a constant extinction along depth. Also,

they are unable to locate the interferometric phase center correctly, which has been found to be deeper than UV models can predict [9].

A non-uniform volume was introduced in [9] by allowing an increasing extinction with depth proportional to the increase of density with depth in ice sheets. Nevertheless, unrealistic depth profiles were necessary to match the data. More physically accurate scattering models, which account for rough surface scattering contributions at hoar layer interfaces and use Mätzlers improved Born approximation [12] for volume scattering, were discussed in [11] to assess Ka-band penetration and in [13] to relate accumulation rates to C-band InSAR data from Greenland. These models describe the geophysical subsurface properties in more detail, but require extensive a priori information about grain size, density, temperature and interface roughness for their initialization.

The effect of refrozen melt layers within the firn column in the percolation zone of Greenland on interferometric coherences was modelled in [14] using Dirac deltas in combination with a UV model for the background volume. Although this model accurately reproduces coherence magnitudes, it also fails to explain the location of the interferometric phase center, which motivated the use of non-uniform volume models [5]. An indication for non-uniform volume models can be found in snow scattering models based on the improved Born approximation [12], where the scattering coefficient in snow or firn is largest for 50% volume fraction of the mixture of ice particles and air. The increase of density with depth in ice sheets therefore implies an initial increase of the scattering coefficient, followed by a decrease when the medium becomes more homogeneous at larger densities respectively volume fractions.

The starting point of this paper is the assessment of the subsurface structure in the percolation zone of the Greenland ice sheet by means of SAR tomography. SAR tomography allows the reconstruction of the 3-D backscattered power and provides a better understanding of the vertical backscattering distribution in SAR data from glaciers and ice sheets. By exploiting multi-baseline InSAR data, this technique was demonstrated for snow [15], lake and fjord ice [16], glaciers [17], and ice sheets [18] and can be used to investigate volume structure modeling. If distinct scattering from refrozen melt layers is present [14], a layer attenuation procedure needs to be applied first to access the general shape of the backscattering distribution of the background volume.

The objective of this paper is to improve the modeling of vertical backscattering distributions in the percolation zone of ice sheets. The goal is a model representation which is flexible enough to be applicable to different test sites, polarizations and frequencies, while, at the same time, being simple enough so that it can be used in model inversion schemes. Different parameterizations of the vertical backscattering distribution are investigated and compared to the vertical backscattering distributions derived with SAR tomography. The derived model performances show the improvement with respect to the conventional UV model. They also indicate which model can be generally preferred across test sites, polarizations and frequencies. The performance assessment of the investigated models will lay the foundation for future applications like subsurface structure retrieval and penetration bias estimation from (Pol-)InSAR data.

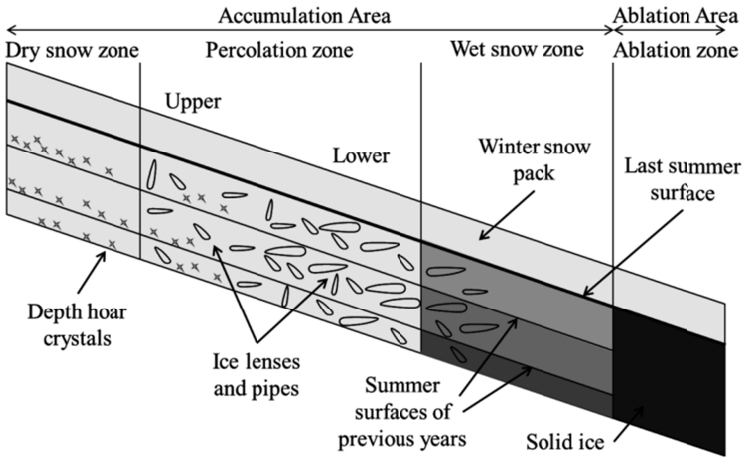

Fig. 1. Sketch of glacier zones from Rizzoli et al. [8] after Benson [19]. The South Dome test site can be classified as an upper percolation zone, the EGIG T05 test site as a lower percolation zone.

3.2 EXPERIMENTAL DATA

3.2.1 SAR DATA IN GREENLAND

The percolation zone in Greenland is characterized by an up to several tens of meters deep firn column until the density of glacier ice is reached. The melt water generated during summer refreezes within the firn and forms ice inclusions in the form of ice lenses and pipes. Depending on the duration and intensity of the melting season, the amount of ice inclusions within the firn changes, which affects the geophysical properties (e.g. density) and the backscattering characteristics of the subsurface.

This study focusses on two test sites in Greenland, which represent different parts of the percolation zone, as illustrated in Fig. 1. The first, South Dome (63.52° N, 44.54° W), can be classified as an upper percolation zone, which is characterized by a rather limited melting season due to its elevation of 2868 m. The second, EGIG T05 (69.87° N, 47.13° W), is an example for the lower percolation zone with an extended melting season at 1938 m elevation. Their locations in Greenland are shown in Fig. 2.

Experimental airborne SAR data from these test sites were acquired during the ARCTIC15 campaign in April and May 2015 with DLR's F-SAR system [20]. This study utilizes fully polarimetric, multi-baseline data at X-, C-, L- and P-band.

The multi-baseline acquisition setup consisted of six to nine parallel flight tracks at 3000 m altitude above ground from two opposite headings and the number of tracks and the range of nominal baselines are listed in Table I. The P-band data were acquired in separate flights 15 days (South Dome) and 11 days (EGIG T05) after the X-C-L acquisitions. The spatial resolution is between 0.5 m (azimuth) × 0.6 m (slant range) at X-band and 1.0 m × 3.8 m at P-band (see Table I). Single-pass X-band InSAR DEMs acquired for each test site were used for the processing and were referenced to corner reflectors on the ice sheet's surface. Multi-baseline phase calibration was carried out to compensate for residual platform motion errors [21].

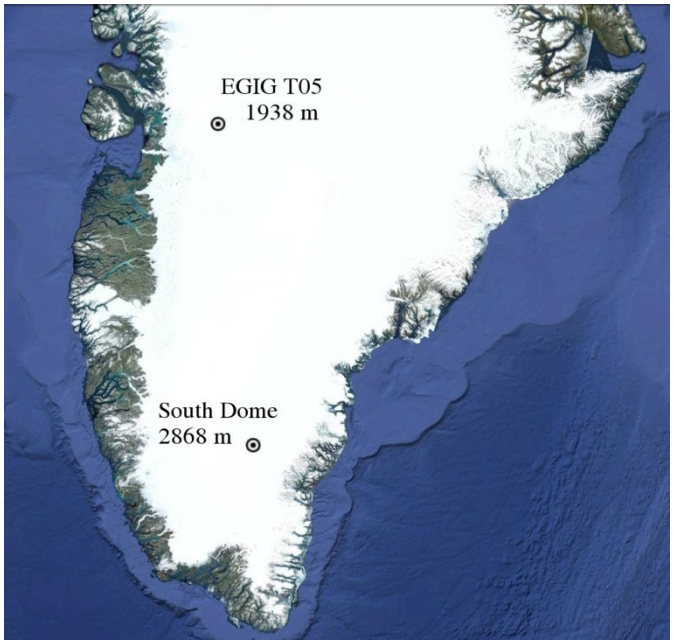

Fig. 2. Location and elevation of the EGIG T05 and South Dome test sites in the southern part of Greenland. © Google Earth.

TABLE I
SOUTH DOME

Band	Freq. [GHz]	# Tracks	Nom. BL [m]	Res. Az. x Rg. [m]
X	9.6	9	2-35	0.5 x 0.5
C	5.3	7	5-35	0.5 x 0.5
L	1.3	6	10-85	0.6 x 1.3
P	0.44	8	10-270	1.0 x 3.8

EGIG T05

Band	Freq. [GHz]	# Tracks	Nom. BL [m]	Res. Az. x Rg. [m]
X	9.6	11	2-40	0.5 x 0.5
C	5.3	9	5-40	0.5 x 0.5
L	1.3	9	5-90	0.6 x 1.3
P	0.44	9	10-270	1.0 x 3.8

Summary of SAR acquisition parameters at both test sites. The nominal baselines are horizontal baselines flown at 3000 m above ground. At X-band, a second antenna provided an additional 1.7 m vertical baseline. The azimuth and slant range resolution is single-look.

The snow and firn conditions at both test sites are considered temporally stable, as temperatures were well below freezing throughout the entire time period of 16 days of the acquisitions. The temporal decorrelation in each multi-baseline dataset can be neglected with only about 15 min between consecutive acquisitions and a maximum temporal separation of 1 h 45 min. Also noise decorrelation is neglected because it is above 0.96 for all frequencies and test sites in the areas investigated in this study, due to the strong backscatter in the percolation zone of Greenland.

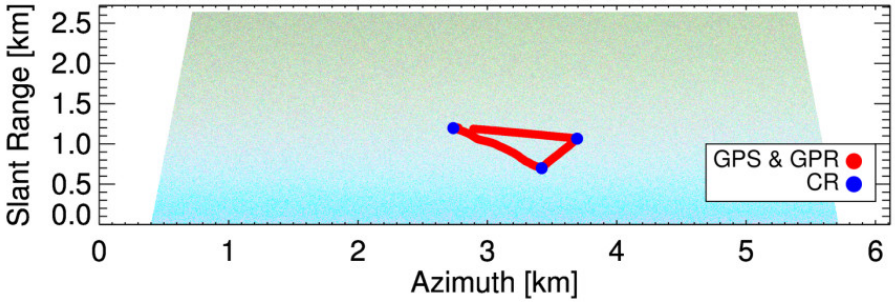

Fig. 3. Polarimetric data acquired at L-band at South Dome and shown in the Pauli basis (HH+VV: blue, HH-VV: red, HV: green). The location of the ground measurements is indicated. Similar ground measurements are available at the EGIG T05 test site.

3.2.2 Ground Measurements

The ground activities during the ARCTIC15 campaign comprised GNSS measurements of the surface elevation, the placement of corner reflectors, ground penetrating radar (GPR) measurements and manual subsurface layer probing with an accumulation probe. The corner reflectors were placed several hundred meters apart in the scene center. The triangle connecting the corner reflectors was sampled by GNSS and GPR (see Fig. 3). These ground activities were conducted 6 days (South Dome) and 11 days (EGIG T05) before the X-, C- and L-band SAR acquisitions and 12 days (South Dome) and 14 days (EGIG T05) after the P-band acquisitions.

The GNSS tracks were acquired in real-time kinematic mode, while the base station measured continuously for 4-5 h on each test site. Precise Point Positioning was applied to the base station in post processing, which served as a reference for the GNSS tracks. This lead to an accuracy in the cm-range which is accurate enough for the purpose of this study. The GNSS tracks provide a precise knowledge of the surface elevation and are, together with the corner reflectors, essential for establishing the correct height reference in SAR tomograms.

The movement of the test sites due to glacier flow between the GNSS measurements and the SAR acquisitions was accounted for by linearly interpolating the positions of corner reflectors and wooden reference sticks from the ground activities before and after the SAR flights. This resulted in a correction factor of 26.8 cm horizontal and 0.47 cm vertical movement per day at EGIG T05 and 0.23 cm and 0.0 cm, respectively, at South Dome.

The refreezing of melt water leads to ice inclusions within the firn in the percolation zone which contribute strongly to the backscattered signal not only in SAR measurements, but also in GPR data. Therefore, GPR data can provide valuable information on the vertical backscattering distribution in the subsurface. Fig. 4 shows examples of the GPR transects acquired along the sampling triangle (Fig. 3) at both test sites with a 500 MHz pulsed radar system. These examples can be considered representative for the entire test sites [14] due to the horizontal homogeneity of the area. The GPR profiles acquired before and after the SAR acquisitions are very similar without any perceptible differences. Further details on the GPR data can be found in [14].

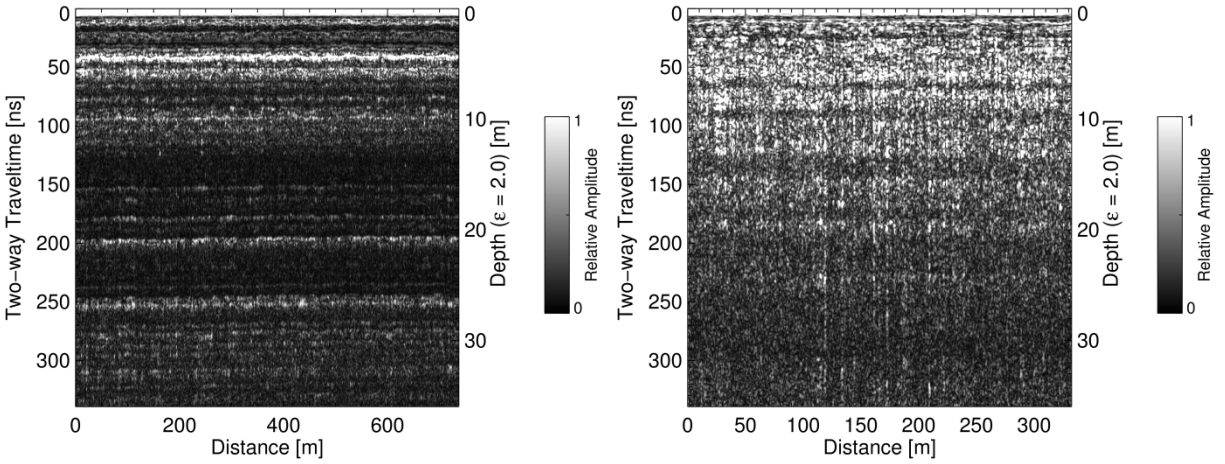

Fig. 4. Amplitude envelope of GPR profiles. (Left) South Dome, where several layers with varying backscattered power are visible. (Right) EGIG T05, with a relatively homogeneous backscattering level that decreases with depth.

The GPR data at South Dome, Fig. 4 (left), reveals distinct layers formed by refrozen melt water, e.g. the one at -4.5 m. In particular, layers related to years with stronger melting are visible, which is confirmed by firn cores [22]. In contrast, a relatively homogeneous backscattering can be found at the EGIG T05 test site, Fig. 4 (right), which indicates an abundance of ice inclusions distributed relatively homogeneous in the firn, due to the stronger melting at EGIG T05 compared to South Dome.

Complementary information concerning the stratigraphy in the first few meters was collected with an accumulation probe, which was used to manually identify hard layers within the firn. Thin ice lenses were detected at various depths at EGIG T05 but a layer at about -1.60 m was measured consistently and was often even impermeable. This depth could correspond to the last summer surface. At South Dome, a weaker layer at -2 m and a particularly strong layer at -3 m were detected, which are not visible in the GPR data [14].

All the in situ and SAR data were acquired within 37 days. The situation can be considered temporally stable throughout this period with temperatures well below freezing and only 1 cm snow height change based on data from the South Dome weather station of the Greenland Climate Network [23].

During the campaign, a partial cover of loose snow of about 5 cm was present on top of a compacted surface and can be neglected due to its marginal extent and its transparency at microwave wavelengths. The accumulation rate at the two test sites is about 0.5-0.6 m water equivalent per year [24], [25], which corresponds to roughly 1-1.5 m of compacted, metamorphic winter snow on top of the firn.

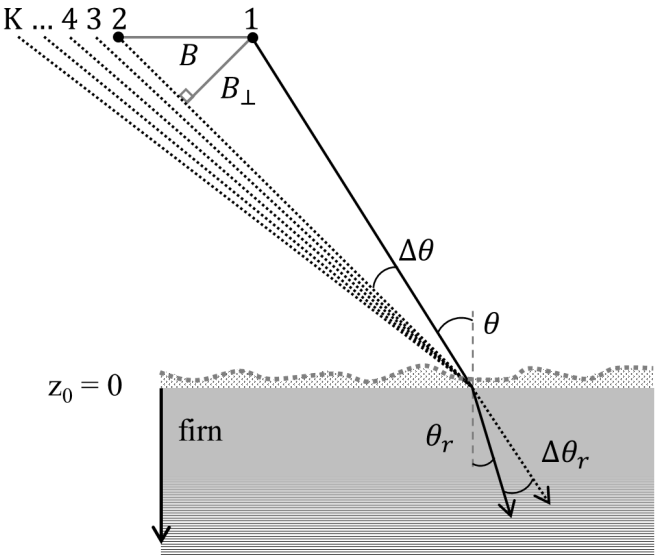

Fig. 5. Multi-baseline interferometric geometry with K acquisitions

3.3 METHODS

3.3.1 TOMOGRAPHY

SAR tomography entails the formation of an additional synthetic aperture in elevation direction, enabling 3-D SAR imaging by resolving the vertical backscattering distribution [26].

Multi-baseline InSAR data can be represented as the covariance matrix R of the data vector $y = [y_1, \dots, y_K]^T$, which contains the single look complex SAR data acquired along K tracks (Fig. 5). The corresponding estimate $\hat{R}$ is derived from spatially averaged multi-look cells with N looks.

$$\hat{R} = \frac{1}{\mathrm{N}} \sum_{\mathrm{n}=1}^{N} y(n) y^H(n) \tag{1}$$

The expected interferometric phase variation for the K acquisitions as a function of height z is described by the steering vector $a(z) = \left[1, e^{ik_{zVol}^2 z}, \dots, e^{ik_{zVol}^K z}\right]^T$ where

$$k_{zVol} = \frac{4\pi\sqrt{\epsilon_r}}{\lambda} \frac{\Delta\theta_r}{sin\theta_r}, \tag{2}$$

denotes the vertical wavenumber in the volume, considering the refracted incidence angle θ_r and propagation in the glacier subsurface [10]. The permittivity ϵ_r can be derived from density of firn cores [22] through a widely used relationship [27] and is set to 2.0 for this analysis. We use a real valued permittivity since scattering losses dominate over absorption losses under dry and frozen conditions [27]. λ is the wavelength in free space. $\Delta\theta_r$ is the angular difference between the radar look vectors due to the spatial separation between the acquisition tracks, after

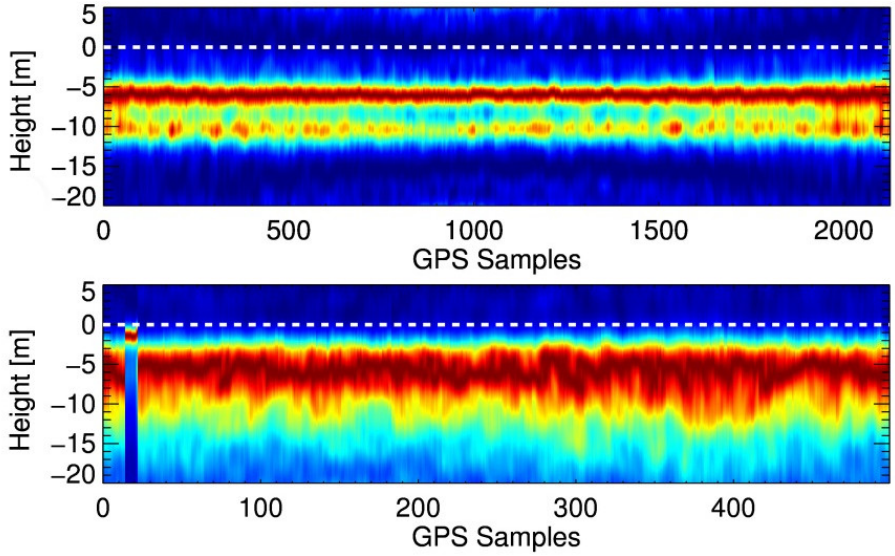

Fig. 6. Tomograms derived with the Capon adaptive beamformer from L-band VV data at South Dome (top) and L-band VV data at EGIG T05 (bottom). The effect of a corner reflector is visible in the EGIG T05 tomogram.

refraction into the firn volume, as depicted in Fig. 5. Similarly, θ_r is the refracted incidence angle within the firn volume given by Snell's law.

Tomographic imaging techniques can be applied to estimate the vertical backscattering distribution from the covariance estimate $\hat{R}$ and the steering vector $a(z)$. We selected the Capon adaptive beamformer, due to its enhanced sidelobe suppression and improved vertical resolution with respect to conventional Fourier beamforming [28].

The vertical Rayleigh resolutions [26] for each test site and frequency are shown in Fig. 7. The trend of the vertical resolution along the GNSS samples is mainly due to the changing incidence angle along the triangular GNSS track.

The minimum unambiguous height intervals for tomographic imaging [26] are 25 m at X-band, 24 m at C-band, 102 m at L-band, and 84 m at P-band for both test sites, which is large enough for the respective signal penetration depths. L-band at South Dome is an exception with only 22 m, because of the lack of a 5 m nominal baseline. Nevertheless, the main scattering is observed well within this unambiguous height interval.

Fig. 6 (top) shows an example of a Capon tomogram at L-band in VV polarization at the South Dome test site. Two dominant layers at -5 m and -10 m are visible, which roughly coincides with the GPR data in Fig. 4 (left). Fig. 6 (bottom) shows the corresponding tomogram from the EGIG T05 test site. In contrast to the layers at South Dome, the backscattering is vertically distributed as expected for volume scattering from abundant ice inclusions as also indicated by the GPR in Fig. 4 (right). The tomograms are derived at the locations of the entire triangular GNSS track, such that the vertical profiles at the first and last GNSS sample correspond to almost the same location on the ground. The vertical axis of the tomograms measures heights relative to the GNSS surface elevation at each point, such that the radar penetration is directly apparent in the results shown.

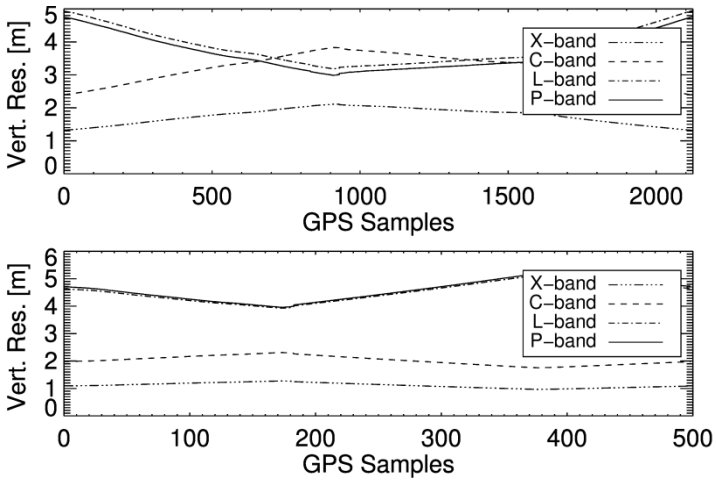

Fig. 7. Nominal vertical resolutions of the tomograms along the GNSS tracks for South Dome (top) and EGIG T05 (bottom).

3.3.2 SIMULATED TOMOGRAMS

The vertical backscattering distribution in the subsurface can be modelled by the superposition of a volume model and dominant subsurface layers represented by Dirac delta functions [14]. The multi-baseline covariance matrix is then [29]

$$R = \sum_{j=1}^{N} p_j a(z_j) a(z_j)^H + p_v \Gamma_v \tag{3}$$

for N subsurface layers located at depth z_j with layer power p_j and volume power p_v. The volume-only coherence matrix Γ_v contains the interferometric coherences obtained from a volume model (e.g. a UV model). Eq. (3) corresponds to coherence modeling in [10] and [14] with layer to volume ratio $m_j = p_j/p_v$. The volume coherences in Γ_v depend on the vertical backscattering distribution of the volume $\sigma_v(z)$, defined from z_0 at the glacier surface to depth z, as depicted in Fig. 5, and can be written as

$$\gamma_{Vol} = e^{ik_z z_0} \frac{\int_{-\infty}^{0} \sigma_v(z) e^{ik_{zVol} z} dz}{\int_{-\infty}^{0} \sigma_v(z) dz} . \tag{4}$$

The simulations in this paper reflect the geometries of the real airborne acquisitions at each individual frequency and test site as expressed by the k_{zVol} values along the GNSS tracks. Also the signal-to-noise ratio of the data is considered in all simulations, but its effect is negligible.

Three different models are considered for the parameterization of $\sigma_v(z)$.

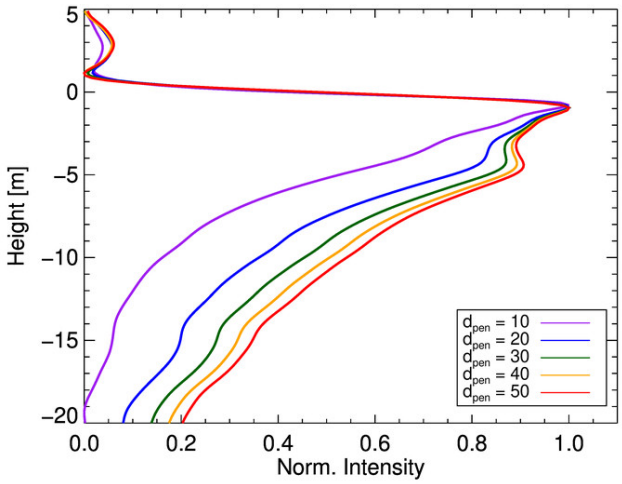

Fig. 8. Capon response of the UV model for different d_{pen} with South Dome X-band imaging geometry and z_{ul} = 0 m. Average of the simulations along the GNSS track.

1) Uniform Volume Model

Assuming a uniform distribution of scatterers and a constant extinction coefficient $\kappa_e(\vec{w})$ [7], the vertical backscattering function $\sigma_v(z)$ in (4) becomes exponential

$$\sigma_{uv}(z) = \sigma_v^0(\vec{w})\mathrm{e}^{\frac{2z\kappa_e(\vec{w})}{cos\theta_r}} = \sigma_v^0(\vec{w})\mathrm{e}^{\frac{2z}{d_{pen}(\vec{w})}}, \tag{5}$$

where $\sigma_v^0(\vec{w})$ is the nominal backscatter power per unit volume in a given polarization channel $\vec{w}$ and the extinction coefficient $\kappa_e(\vec{w})$ accounts for both scattering and absorption losses. We use the parameterization with one-way penetration depth d_{pen}, which is inversely related to κ_e through $\kappa_e = cos(\theta_r)/d_{pen}$. Inserting (5) into (4) leads to γ_{uv} for a uniform volume (UV) model [7]

$$\gamma_{uv} = e^{ik_z z_0}\frac{1}{1+\frac{id_{pen}(\vec{w})k_{zVol}}{2}}e^{ik_{zVol}z_{ul}}, \tag{6}$$

where z_{ul} is the height of the upper limit of the UV model and it is typically assumed to start at the surface $z_{ul} = z_0$ = 0 m. To account for the fact that the first 1-5 m, depending on the frequency, are largely transparent at South Dome, we allow the UV model to be shifted downwards with the z_{ul} parameter. Fig. 8 shows UV model simulations with z_{ul} = 0 m and varying d_{pen}. The exponential backscattering distribution of the UV model is slightly modified by the Capon imaging with the South Dome X-band k_{zVol} values.

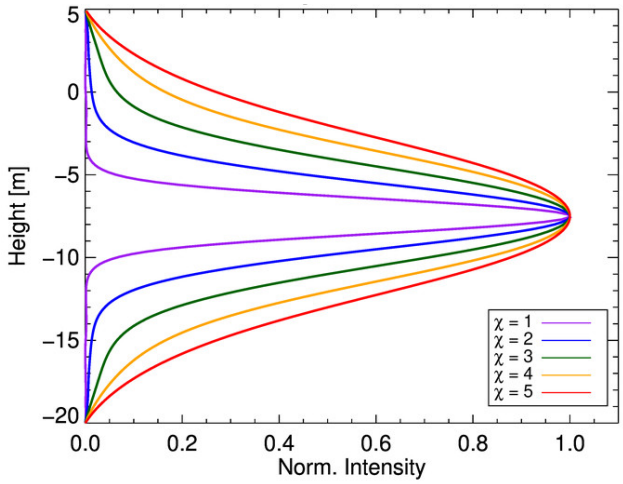

Fig. 9. Capon response of the Gaussian volume model for different χ with South Dome X-band imaging geometry and δ_g = -7.5 m.

2) Gaussian Volume Model

Physical snow scattering models motivate a vertical backscattering function with non-uniform extinction. In the upper part, the increase in grain size and density with depth leads to an increasing scattering coefficient. As density increases even further with depth, the volume fraction of the ice-air mixture exceeds 50% and the firn becomes more homogeneous and the scattering coefficient decreases again [12]. Such a model was shown to improve interferometric phase center modeling, but requires extensive in situ data [5]. A similar behavior can be approximated by a Gaussian function

$$\sigma_g(z) = \mathrm{e}^{\frac{-(z-\delta_g)^2}{2\chi^2}}, \tag{7}$$

where δ_g is the mean height of the Gaussian and χ its standard deviation.

Inserting $\sigma_g(z)$ in (4), the solution for integral boundaries [-∞, 0] for glaciers and ice sheets is, similar to [30],

$$\gamma_g = e^{-\frac{k_{zVol}^2\chi^2}{2}+i\delta k_{zVol}} \frac{\mathrm{erfc}\left(\frac{\delta_g+ik_{zVol}\chi^2}{\sqrt{2}\chi}\right)}{\mathrm{erfc}\left(\frac{\delta_g}{\sqrt{2}\chi}\right)}, \tag{8}$$

where erfc() is the complementary error function. The simulations of a Gaussian model with δ_g = -7.5 m and different χ in Fig. 9 show the increasing and decreasing nature of backscattering with depth, as intended by this approximation of physical snow scattering models.

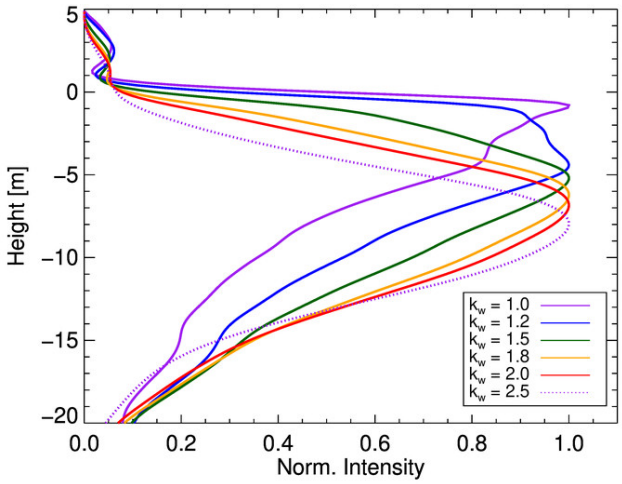

Fig. 10. Capon response of Weibull model with variable shape parameter k_w and fixed λ_w = 0.10 with South Dome X-band imaging geometry.

3) Weibull Volume Model

The Weibull function includes both the exponential (UV) and the Gaussian function and also allows shapes in the transition between these two cases. Its density function can be written as

$$\sigma_w(z) = \lambda_w k_w (\lambda_w z)^{k_w - 1} e^{-(\lambda_w z)^{k_w}} \tag{9}$$

where λ_w denotes the scale parameter, which is similar, but not identical, to the extinction coefficient $\kappa_e(\vec{w})$ in the UV model. k_w is the shape parameter and $k_w = 1$ results in an exponential, $k_w = 2$ leads to a Rayleigh distribution and $k_w \approx 3.6$ approximates a Gaussian. The integrals in (4) are solved numerically using (9), as closed form solutions are only available for particular values of k_w. Fig. 10 shows how the shape parameter k_w can change the vertical distribution from an exponential towards a Gaussian.

These three simple models for the vertical backscattering function can be used to approximate the volume contribution in the tomograms with only two model parameters. The limited number of parameters is important for future inversion approaches. The UV and Gaussian models have one parameter that defines the shape and one parameter that defines the vertical shift. The Weibull model cannot be shifted in height but has two parameters that provide a larger flexibility in shape.

4) Layer Plus Volume Model

Scenarios with dominant subsurface layers can be characterized with Dirac deltas superimposed on a volume model, see (3). In this way, the South Dome data, with the clear layers in Fig. 6, can be simulated as illustrated in Fig. 11 (top) and Fig. 12.

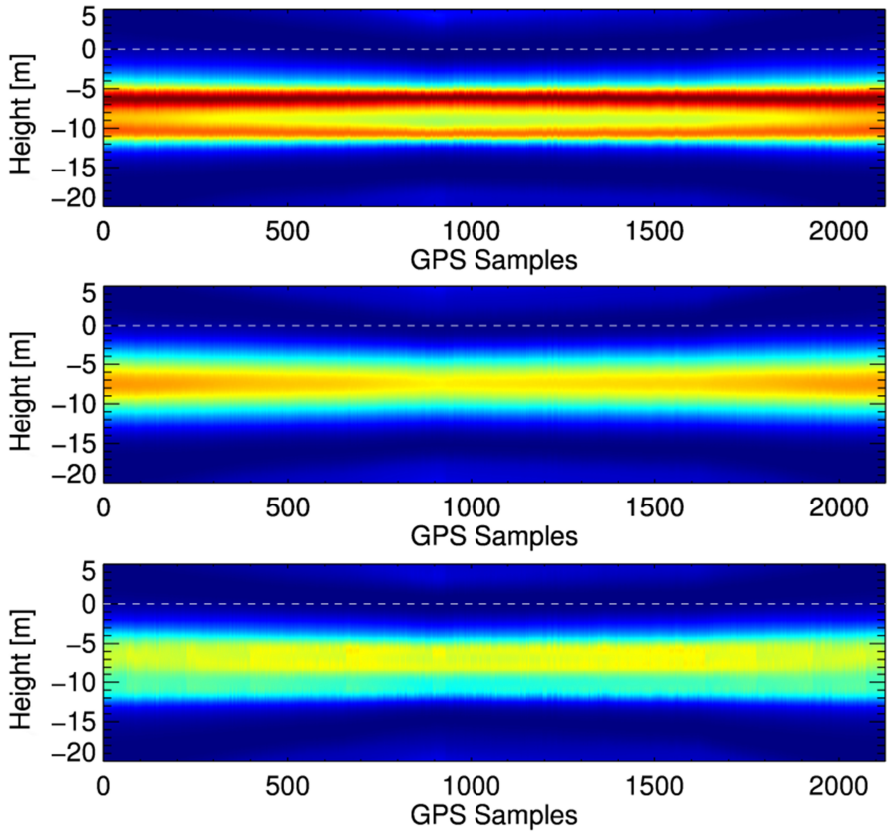

Fig. 11. Tomographic reconstructions, using the Capon beamformer, of simulated data for the L-band imaging geometry at the South Dome test site. (Top) Gaussian volume model plus two layers, roughly representing the data in Fig. 6 (top). $z_1 = -6\,m\,; z_2 = -11\,m\,; m_{1,2} = 0.2\,; \delta_g = -7.5\,m\,; \chi = 3\,m.$ (Middle) Only the Gaussian volume. (Bottom) Full simulation with layers attenuated, fixing the Dirac delta threshold for Δz at 3%.

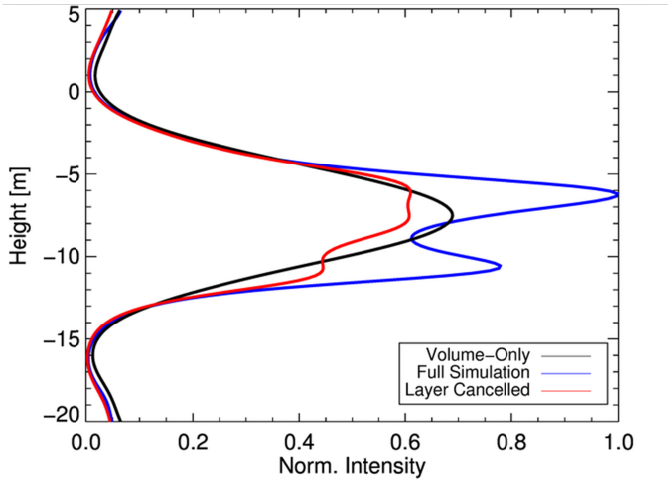

Fig. 12. Example of layer attenuation of a two layer plus Gaussian volume simulation of an L-band scenario. Average profiles of Fig. 11. Dirac threshold 0.03.

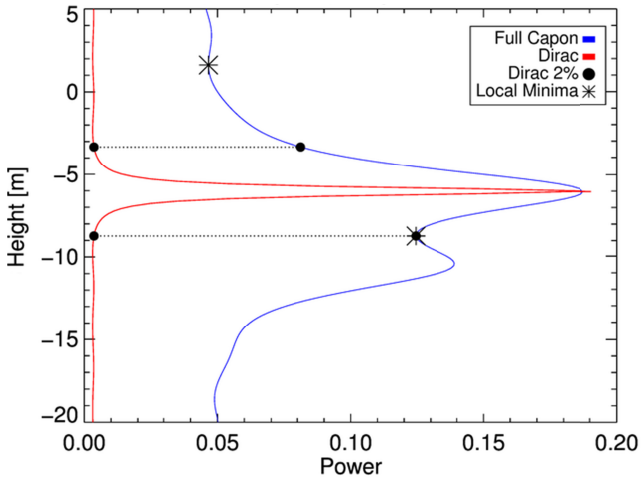

Fig. 13. One example of the South Dome L-band HH data to illustrate the power estimation depending on the position of the 2% power of the Dirac delta response and the local minima.

3.3.3 Layer Attenuation

To isolate and better assess the vertical backscattering distribution of the volume alone, the dominant subsurface layers in the South Dome data, which correspond to refrozen melt layers, can be attenuated. By rearranging (3), an estimate of the volume-only coherence matrix $\hat{\Gamma}_v$ can be extracted from the full covariance matrix $\hat{R}$ by coherently subtracting the signal contributions of Dirac deltas at the appropriate depths. The advantage of the proposed method is that it leaves the remaining volume untouched at the cost of imperfect layer attenuation.

If the vertical layer positions z_j and powers p_j can be estimated, the layers can be attenuated. The layer positions can be derived robustly from the maxima of the vertical Capon spectra and are confirmed by the positions found with MUSIC [31], which is an established method for localizing point scatterers [32]. In addition, a visual inspection of each South Dome profile verified that the detected Capon maxima correspond to the dominant layers in the data.

The estimation of the power p_j of the layers is more challenging. The Capon spectrum is a good estimate of the vertical backscattering distribution if a large number of independent samples is used [33]. This requirement can be considered fulfilled, as the covariance matrix estimates $\hat{R}$ at each GNSS sample are based on at least 310 looks. The resulting estimation window sizes do not exceed 32 m x 38 m (slant range x azimuth).

However, the backscattered power in a Capon spectrum at a position z_j represents the combined power of layer and volume at the given depth. A correct estimate of p_j therefore needs an estimate of the underlying volume power at position z_j.

A way to achieve this is by using the Capon impulse response function of a Dirac delta at z_j and calculating the vertical distance Δz between the peak at z_j and the minima of the Dirac impulse on each side. The powers of the full Capon spectrum at $z_j \pm \Delta z$ are considered to be not affected by the Dirac delta of the layer and can be averaged to estimate the volume power at z_j. A relatively smooth vertical backscattering function of the volume is assumed here. For more

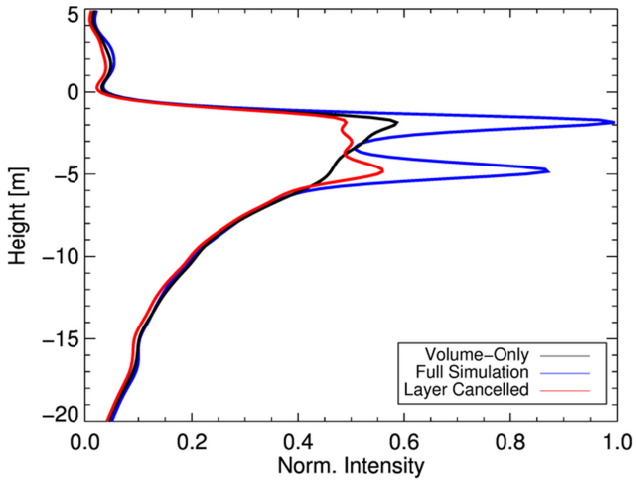

Fig. 14. Example of layer attenuation of a uniform volume plus two layers with South Dome X-band imaging geometry and SNR, roughly representing the X-band data. $z_1 = -1.8\ m$; $z_2 = -4.8\ m$; $m_{1,2} = 0.1$. UV model: $d_{pen} = 15\ m; z_{ul} = -1\ m$. Dirac threshold 0.02.

robustness, the minima are calculated as the positions were the Dirac impulse response drops to 2% of its maximum, see the example in Fig. 13. Tests on different simulations and data showed that this threshold has to be adjusted in the 2% to 3% range depending on the profile under investigation.

In case an adjacent layer would affect the volume power estimate at $z_j \pm \Delta z$, the local minimum of the profile between the two layers is used, instead. The final estimate of the layer power p_j is then the difference of the Capon spectrum at z_j and the mean of its values at $z_j \pm \Delta z$.

This estimation of the layer positions and amplitudes and the resulting estimation of the volume-only coherence matrix $\hat{\Gamma}_v$ was tested on simulations and one result is shown in Fig. 11. The volume component after the layer attenuation, Fig. 11 (bottom), is enhanced compared to the full simulation (layers and volume) in Fig. 11 (top) and better resembles the volume-only simulation in Fig. 11 (middle). Due to the amplitude estimation procedure, the layer attenuation depends on the vertical resolution, which explains the differences along the GNSS track. Fig. 12 and Fig. 14 show the comparison of average profiles between the full simulation, the volume-only component and the simulation after the layer attenuation for scenarios resembling the L-band and X-band data at South Dome. Layer residuals are still present, but the general shape of the volume can be assessed after the layer attenuation procedure.

The performance of the layer attenuation procedure was tested on the two model scenarios shown in Fig. 12 and Fig. 14. In both cases, the RMSE, which can be considered normalized because the simulated profiles are normalized, between the layer-attenuated profiles and the background volume stays below 5%, independent of the layer-to-volume ratios. Similarly, the RMSE remains almost constant and below 6% for Dirac response thresholds between 2% and 4%, which suggests that the procedure is robust with respect to the selection of this threshold parameter. However, a qualitative assessment of the layer attenuation results is important to avoid artefacts in the remaining profile.

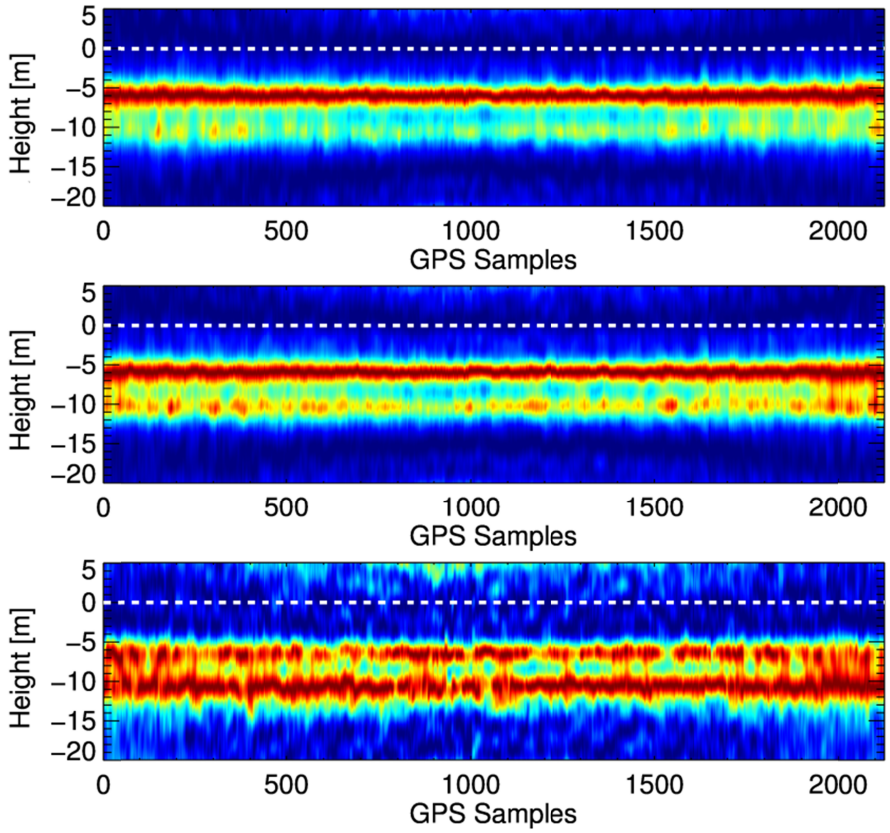

Fig. 15. Capon tomograms for L-band South Dome data in HH (top), VV (middle) and HV (bottom). The same layers are present in each polarization, but with different (normalized) intensities.

3.4 RESULTS

3.4.1 CHARACTERISTICS OF SUBSURFACE STRUCTURES

SAR tomography allows assessing the vertical subsurface structure of the test sites. Particularly the percolation features generated by refrozen melt water, e.g. ice lenses and pipes, are characterized by strong backscattering. In case refrozen melt-features are limited to certain depths, e.g. at a previous summer surface, they will appear as a continuous layer of strong backscatter.

Fig. 15 shows L-band Capon tomograms along the GNSS track for the South Dome test site in HH, VV, and HV polarizations. Two strong layers are visible at about -5 m and -10 m, which correspond roughly to the layers visible in the GPR profile in Fig. 4 (left). There is an increase in the relative intensity of the second layer from HH to VV and particularly to HV, which may be rather interpreted as a relative decrease of the first layer. It is important to note that the normalization of each tomogram hides the fact that the overall intensity in HV is weaker than in the co-polarized (co-pol) channels.

Fig. 16 shows tomograms at the other frequencies at South Dome. The VV channel is omitted because it is always very similar to HH, which is also true for the EGIG T05 data. The

P-band tomograms (Fig. 16, top) show strong similarities with the ones at L-band, with the difference that the layers have a slightly weaker contrast to the background volume.

At C-band (Fig. 16, middle), there is a clear difference between polarizations. The strong layer evident at -5 m in the L- and P-band tomograms is still present, while additional scattering appears below this dominant layer in HV. In addition, scattering contributions appear above the dominant layer in HH. Also a layer at around -2 m is indicated. The signatures of two corner reflectors are visible around GNSS samples 900 and 1600.

The layer at -2 m is clearly visible at X-band (Fig. 16, bottom), particularly in HH. This layer was also detected using an accumulation probe during the field measurements conducted in the frame of the campaign.

Overall, the backscatter occurs at greater depth as the wavelength increases. Also, there is a pronounced difference between co- and cross-polarizations, with HV showing deeper scattering contributions. Interestingly, the layer at -2 m, which is clearly visible in HH at X-band, disappears completely at lower frequencies.

In contrast to South Dome, the tomograms at EGIG T05 (Fig. 17 and average profiles in Fig. 19) show no discrete layers. Instead, the backscatter is vertically distributed, similar to the GPR in Fig. 4 (right), due to the abundance of refrozen melt features. Lower frequencies show volume scattering at greater depths than higher frequencies and, similarly, there is deeper scattering in HV than in the co-pol channels. The co-pol tomograms at C- and X-band almost appear as a distinct layer, but the steep increase in backscattered power just below the surface and the gradual decrease below the maximum points towards a UV model with high extinction. The HV channels show a similar vertical distribution, but with a lower extinction if interpreted in terms of a UV model.

Note that the corner reflectors appear below the surface in the EGIG T05 tomograms, because their effect in the reference DEM in the form of localized peaks is attenuated by the size of the applied estimation windows. For South Dome, the reference DEM was strongly multilooked, so that the reflectors appear correctly at the surface.

Interestingly, the first few transparent meters at both test sites in L- and P-band consist not only of the snow accumulation of the current winter, but also of firn from the previous 1-3 years (see Section 3.2.2).

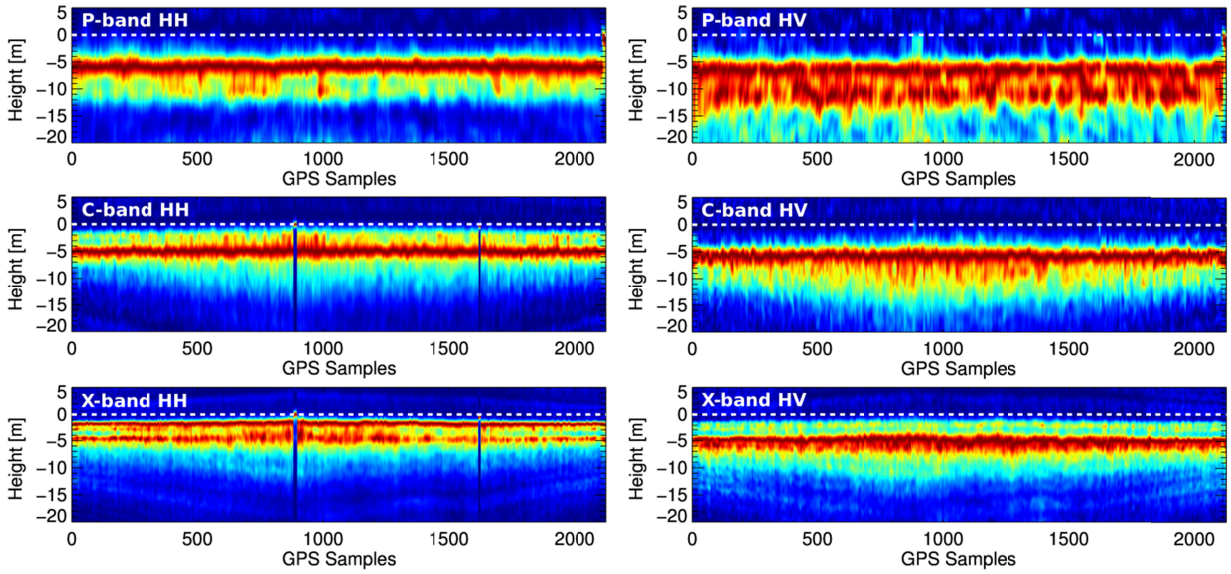

Fig. 16. Capon tomograms at the South Dome GNSS track. From top to bottom: P-, C-, and X-band. (Left) HH, (Right) HV. See Fig. 15 for L-band. Each tomogram is normalized individually.

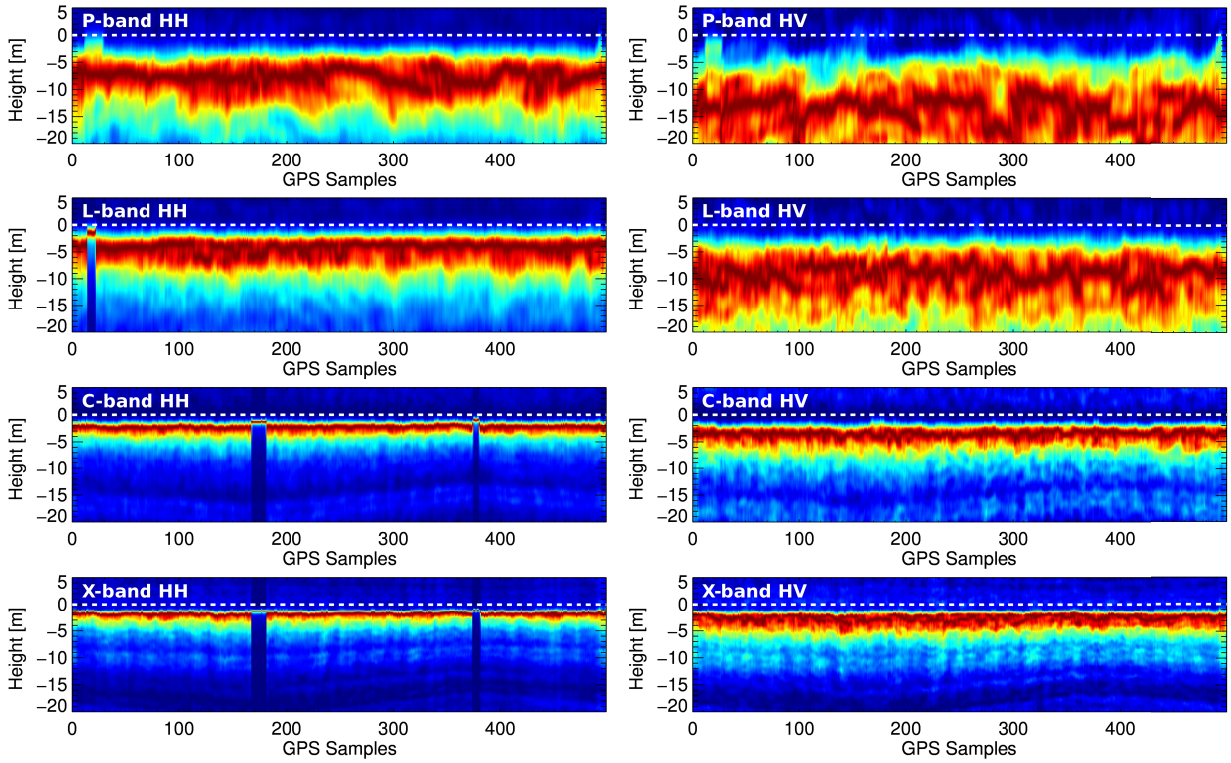

Fig. 17. Capon tomograms at the EGIG T05 GNSS track. From top to bottom: P-, L-, C-, and X-band. (Left) HH, (Right) HV. Each tomogram is normalized individually.

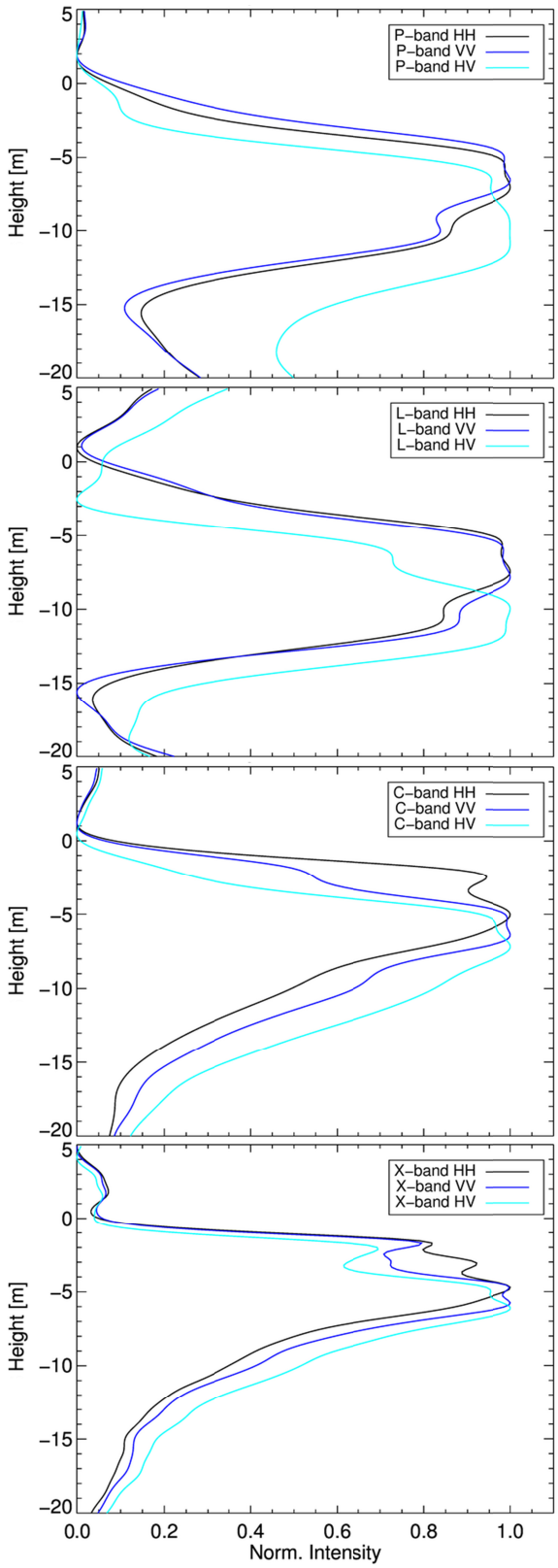

Fig. 18. Averaged and normalized layer-attenuated Capon tomograms for the South Dome data at P-, L-, C-, and X-band (Averages of Fig. 15 and Fig. 16 after layer attenuation).

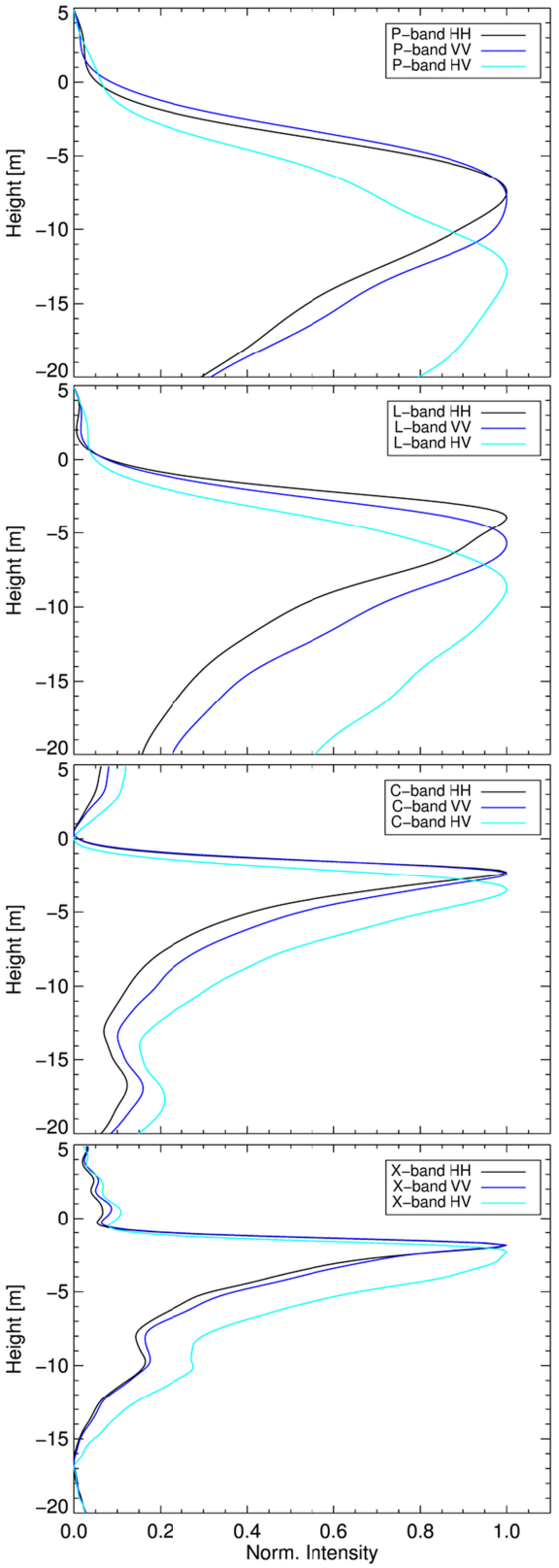

Fig. 19. Averaged and normalized Capon tomograms for the EGIG T05 data at P-, L-, C-, and X-band (Averages of Fig. 17).

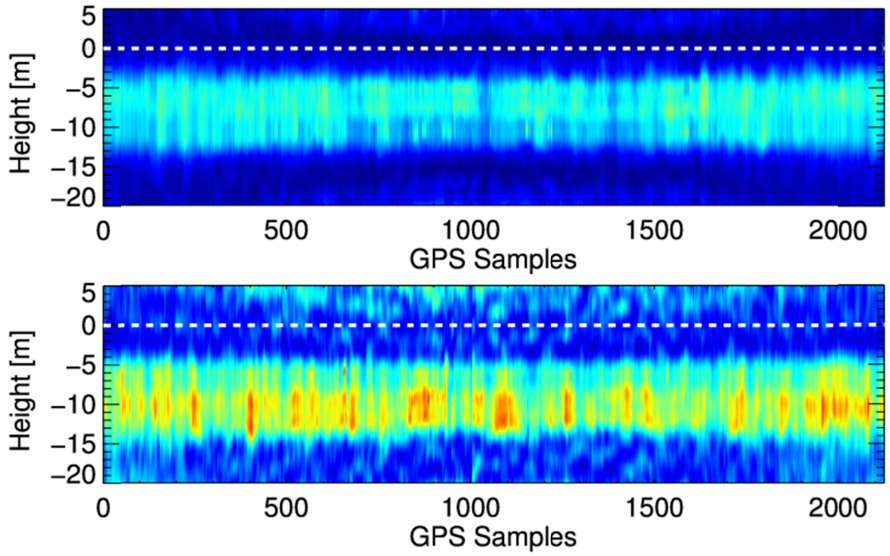

Fig. 20. Layer-attenuated tomograms from South Dome L-band data in HH (top) and HV (bottom). The shown colors are directly comparable to those in Fig. 15 due to an identical scaling.

3.4.2 Results of the Layer Attenuation Procedure

The strong scattering layers in the South Dome tomograms were attenuated with the procedure described in Section 3.3.3. Dirac delta thresholds of 2% provided the best attenuation for all frequencies. At P- and L-band, two layers were attenuated, while it was only one at C-band, as indicated by the full tomograms (Fig. 15 and Fig. 16). At X-band, a third layer at -3 m appeared after the two apparent layers were attenuated, and was attenuated with an additional iteration.

The attenuation results are shown for the L-band HH and HV tomograms in Fig. 20, with the same scaling as in Fig. 15. The layers are removed and the background volume is estimated. Average layer-attenuated profiles are shown in Fig. 18 for all South Dome data. The vertical distribution of the volume of the HV data appears deeper at all frequencies, even though the shape is similar across polarizations, particularly at X-band. The co-pol channels are always very similar, particularly at P- and L-band. Interestingly, the vertical backscattering distribution of the volume is rather symmetrical at L-band, while it appears skewed at higher frequencies, with a steep increase just below the surface followed by a gradual decrease with depth. Even though P-band appears symmetric in Fig. 18, there is a gradual decrease below -20 m, which is not shown. This suggests that different model representations, i.e. UV and Gaussian, are required at different frequencies.

3.4.3 Assessment of the Polarization Diversity

The layer-attenuated profiles for South Dome in Fig. 18 and the full profiles for EGIG T05 in Fig. 19 are a good basis for investigating the differences between polarizations across frequencies and test sites. This is important for potential Pol-InSAR model inversion techniques,

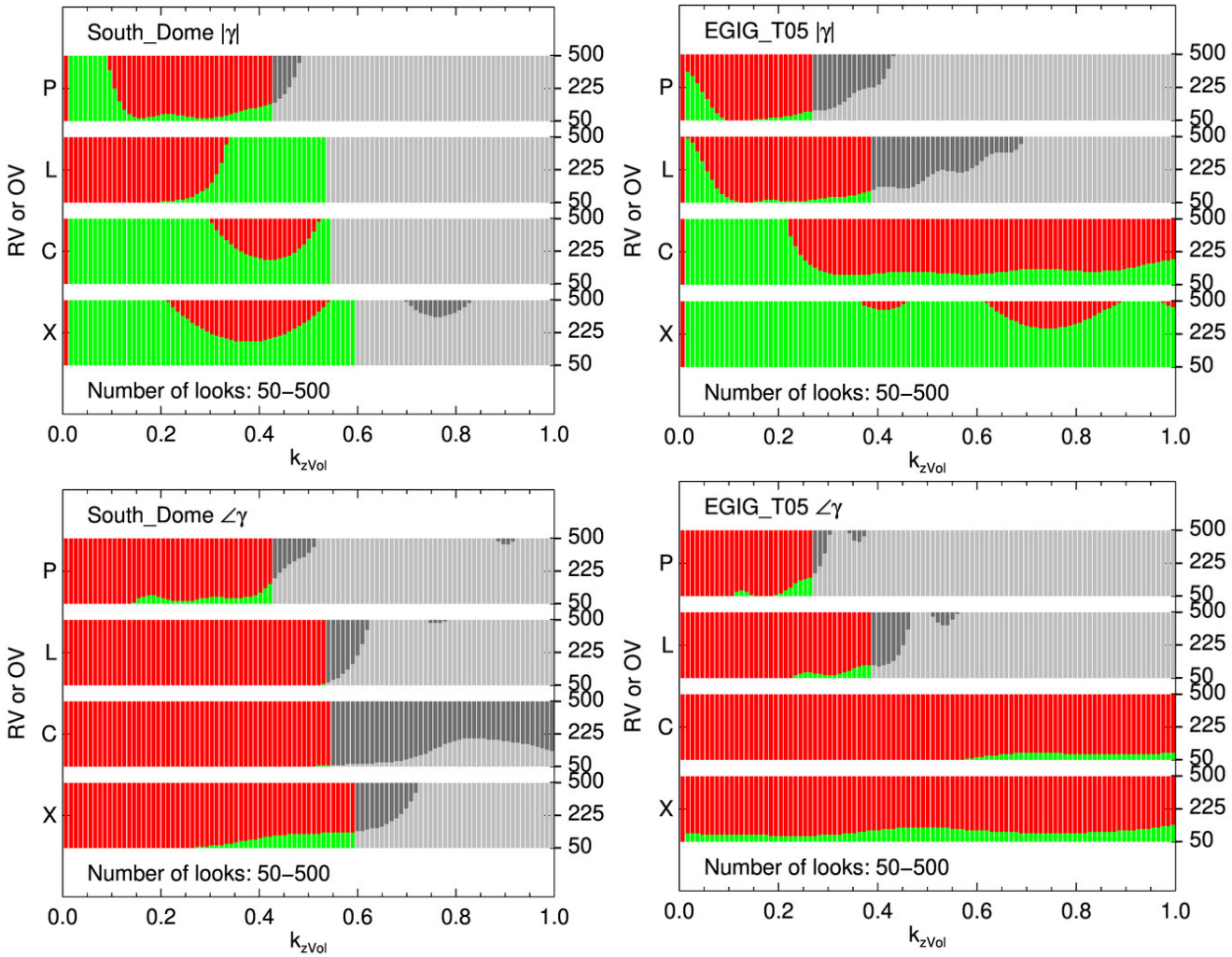

Fig. 21. The plots indicate if the magnitude (top) and phase (bottom) of the coherences derived for $0 < k_{zVol} < 1$ from the vertical profiles of the three polarizations in Fig. 18 and Fig. 19 are within each other's standard deviation (green) or not (red). This is used as an indicator if a random volume assumption could hold. (Left) South Dome. (Right) EGIG T05. This indicator is derived for each frequency and test site for 50 to 500 looks. Green and red become light and dark gray colors when the coherence magnitude of all three polarizations drops below 0.2.

where the assumption of a random volume is essential to reduce the parameter space. A random volume is considered here as the case where all polarizations have identical vertical backscattering distributions up to a constant amplitude factor. In an oriented volume scenario, the vertical backscattering distributions and thus also the volume model parameters are different across polarizations, which increases the parameter space and complicates future model inversions. The random volume assumption is tested by deriving coherences through (4) from the vertical profiles in Fig. 18 and Fig. 19 in the three different polarizations for a range of k_{zVol} values and number of looks. Magnitude and phase standard deviations [34] of the resulting coherences are then calculated and used to check if the coherences of the three polarizations are within each other's standard deviation. In Fig. 21, green and light gray indicates if the coherences are within each other's standard deviation (indication of a random volume), while red and dark gray points towards an oriented volume scenario. The results depend on k_{zVol} and

the number of looks. Gray colors indicate when the coherences in all polarizations drop below 0.2.

For coherences above 0.2, the large portions of red, particularly for the interferometric phase (Fig. 21, bottom), indicate that the coherences of the three polarizations are separated by more than their standard deviations. Higher number of looks lead to more accurate coherence estimations and thus to a finer separation of the coherences, while for smaller number of looks the random volume assumption can be considered sufficient due to the larger standard deviations. The coherences of the co-pol channels HH and VV coincide very closely and it is mainly the HV coherences which are not within the standard deviations of the co-pol coherences. This is mainly due to the standard deviation of the interferometric phase (Fig. 21, bottom) rather than the magnitude (Fig. 21, top). The coherence magnitudes are within each other's standard deviation for large parts of the investigated k_{zVol} and number of looks. This could make the assumption of a random volume sufficient for approaches which consider only the magnitude of coherences. In contrast, the phase is highly sensitive to even small differences in the vertical backscattering distribution between the polarizations, e.g. even for the seemingly similar profiles in X-band at both test sites in Fig. 18 and Fig. 19. The main reason are vertical shifts between the vertical backscattering distributions of the polarizations, which affect only the phase but not the magnitude. In general, the criterion applied in this study suggests that the random volume assumption is not valid. However, there are some green indications in Fig. 21 for low number of looks at almost all frequencies and test sites, even for the phase. This could suggest that, depending on the application, a random volume assumption can be still a useful approximation also at higher number of looks.

The standard deviation criterion is fulfilled for low coherences, indicated by light gray color in Fig. 21, because all polarizations tend towards $|\gamma| = 0$ for increasing k_{zVol}.

Note that the profiles used to calculate the coherences for this analysis extend deeper than the plotting limit of -20 m in Fig. 18 and Fig. 19 for L- and P-band. The lower limits of the profiles were chosen in a way to include scattering contributions as deep as possible while avoiding the effect of ambiguities, e.g. -20 m at X-band and -70 m at P-band for the EGIG T05 data. These lower limits are also used for the analyses in Sections 3.4.4 and 3.4.5. However, the main scattering appears in the first 20 m and the profiles at L- and P-band gradually decline below -20 m. Therefore, and to enhance the comparability with X- and C-band, the profiles are shown only until -20 m.

3.4.4 Comparison to Volume Models based on Vertical Profiles

The next step is to assess to what extent the observed vertical backscattering distributions can be described by simple volume models. For this comparison the layer-attenuated profiles from the South Dome test site (Fig. 18) and the full profiles from the EGIG T05 test site (Fig. 19) are used, since the latter do not show dominant scattering layers and can be considered as a pure volume response.

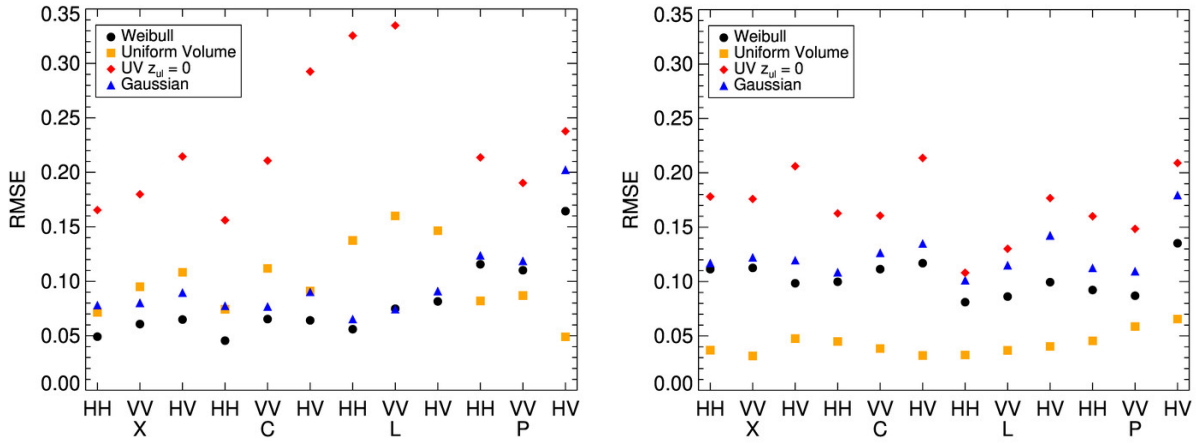

Fig. 22. RMSE of the best fit between the vertical profiles of the volume models and the layer-attenuated data for South Dome (left) and the full data at EGIG T05 (right). A UV model with fixed upper limit $z_{ul} = 0$ m is shown for comparison.

The South Dome and EGIG T05 profiles are compared to average profiles of simulated Capon tomograms based on the volume models described in Section 3.3.2. For each simulation, the imaging geometry of the corresponding frequency, represented by the k_{zVol} values, is used. This ensures similar Capon imaging characteristics. The investigated profiles extend deeper than the plotting limit of -20 m in Fig. 18 and Fig. 19, as described in Section 3.4.3.

The analysis of the profiles in Fig. 18 and Fig. 19 suggests that a UV shape with a steep increase at the top and a smooth decrease at the bottom is well suited for describing e.g. the X- and C-band profiles of the EGIG T05 test site. Other profiles such as the ones at L-band at South Dome, however, appear rather symmetric in the vertical direction, indicating a preferable parameterization with a Gaussian or a Weibull model.

The data is compared to the three models described in Section 3.3.2 by means of RMSE. The example in Fig. 23 shows the RMSE between a UV model and the layer-attenuated South Dome X-band HH profiles (Fig. 18) for a range of z_{ul} and d_{pen} values. Since the data does not follow a UV model as closely as e.g. the X-band data at EGIG T05, the correlation is spread across a wide range of d_{pen} values. But the steep increase of the vertical backscattering distribution at around -1 m leads to a correlation maximum at this value for z_{ul}.

The RMSE of the best-fit between the UV, Gaussian, and Weibull models and the real data profiles is reported in Fig. 22. The results of a conventional UV model starting at the surface with $z_{ul} = 0\ m$, as used in [7], [8], [9], and [10], are included for comparison.

The improvement with a second model parameter is obvious and the conventional UV model without any shift of the upper limit performs significantly and consistently worse than any of the other three models. At South Dome, the Weibull model performs best at X-, C-, and L-band, with the Gaussian performing almost as well. The UV model performs better only in case of very skewed vertical distributions at P-band. This is mainly due to a gradual decrease below the lower plotting limit of -20 m in Fig. 18, which is accurately reproduced by a low extinction UV model.

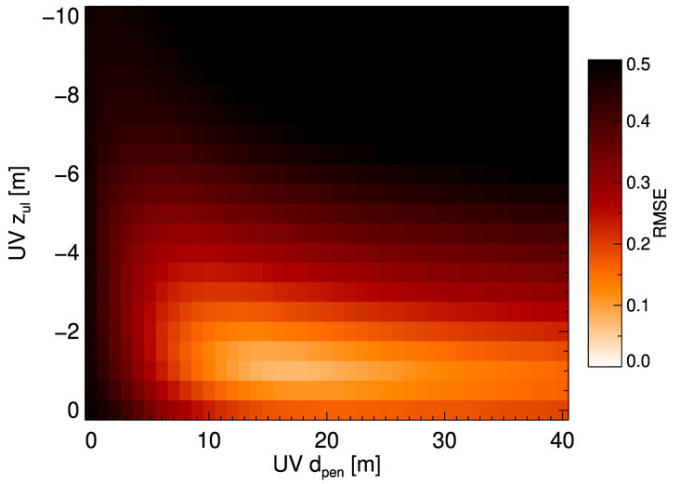

Fig. 23. RMSE of a UV model for varying upper limit z_{ul} and penetration depth d_{pen} with the layer-attenuated South Dome X-band HH data.

In the EGIG T05 case, the conventional UV model without shift also performs significantly worse, as expected due to the fact that the other models have an additional degree of freedom. As already indicated by the skewed vertical distributions in Fig. 19, the shifted UV model clearly performs best for all frequencies and polarizations at EGIG T05.

3.4.5 Comparison to Volume Models based on Coherence

The evaluation of the volume models based on the comparison of vertical profiles of models and tomographic data in the previous Section 3.4.4 gives a good understanding of the preferred theoretical model choice. However, considering model inversion for geophysical parameter retrieval or phase center depth estimation for DEM penetration bias compensation, the quantity of interest is the interferometric coherence. This section therefore investigates how well the different models perform at reproducing the complex coherences (see Fig. 24) instead of how well they reproduce the actual vertical backscattering distribution as it was shown in Section 3.4.4. For this comparison, coherences are calculated by using (4) based on the profiles in Fig. 18 and Fig. 19 and compared to coherences derived in the same way from the Capon response of the models with the imaging geometry of the data. This comparison yields slightly different results, because the results based directly on the vertical profiles in Section 3.4.4 are very sensitive to the vertical alignment of models and data, which strongly affects the interferometric phase $\angle\gamma$, but not the coherence magnitude $|\gamma|$. For instance, a UV model will always yield identical $|\gamma|$ independent of the vertical shift, which only affects the phase.

The RMSE in Fig. 24 was derived on complex coherences calculated for increasing k_{zVol} starting from $k_{zVol} = 0$ until $|\gamma|$ drops to 0.2. The profiles used to calculate the coherences extend deeper than the plotting limit of -20 m in Fig. 18 and Fig. 19, as described in Section 3.4.3.

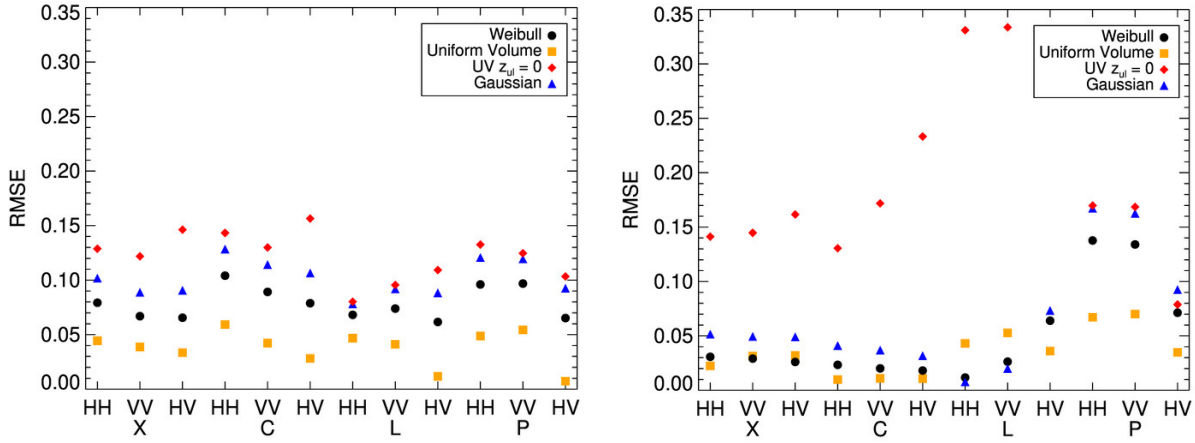

Fig. 24. RMSE of the best fit between interferometric coherences derived from the volume models and the layer-attenuated data for South Dome (left) and the full data at EGIG T05 (right). A UV model with fixed upper limit $z_{ul} = 0$ m is shown for comparison.

The results in Fig. 24 show that, as in the previous section, the conventional UV model starting at the surface with $z_{ul} = 0\,m$ performs worse at both test sites. For the South Dome data (Fig. 24, left), the UV and Weibull models perform best for X- and C-band. At L-band, HH and VV are better modelled by a Gaussian or Weibull function as expected given the rather symmetric profiles in Fig. 18. At P-band, the UV model fits better to the complex coherences derived from the data. In general, the difference between the UV, Gaussian and Weibull models is small for X-, C-, and L-band. In the EGIG T05 case (Fig. 24, right), the UV model performs again best, which was expected due to the skewed vertical distributions in Fig. 19. This is consistent across all frequencies and polarizations at this test site.

Since the RMSE in Fig. 24 is derived by comparing complex coherences instead of vertical profiles as it was the case in Fig. 22, the coherence magnitude has a stronger influence. In contrast, the comparison based on vertical profiles in Section 3.4.4 is very sensitive to vertical shifts and thus to the interferometric phase. This explains why in a few cases, e.g. at C-band at South Dome, the best model differs between Fig. 22 and Fig. 24. This indicates that the preferred model choice depends additionally on the application, i.e. whether it is required to accurately simulate coherences or to estimate phase center depths. But in most cases, the best model is the same for both analyses.

An important finding is that, for almost all frequencies at both test sites, the same model performs best across all polarizations. The only exception is L-band and to a small extent X-band at South Dome. This is important for potential Pol-InSAR approaches, because it suggests that in general the same volume model can be applied for all polarizations.

3.5 Discussion and Conclusion

There is the need for modeling the vertical backscattering distributions from glaciers and ice sheets to better interpret interferometric SAR data acquired over such areas. At the same time, it is desirable to develop simple models, with few parameters, to facilitate future inversion

approaches. Such models could allow the correction of the penetration bias in InSAR DEMs over glaciers and ice sheets and support the retrieval of subsurface information from Pol-InSAR data.

The vertical backscattering distributions, derived with SAR tomography, at the EGIG T05 test site in the lower percolation zone are characterized by a steep increase at the top and a gradual drop towards greater depths. Dominant scattering layers at the South Dome test site, in the upper percolation zone, were attenuated to better assess the background volume backscattering distribution. These layer-attenuated profiles tend to be vertically more symmetrical. This suggests that different parameterizations of the vertical backscattering distribution are required to describe the observations at the two test sites.

GPR data (Fig. 4) confirm the vertically homogeneous scattering at the EGIG T05 test site. At South Dome, on the other hand, the GPR data are dominated by the refrozen melt layers and give no indication on the background volume.

Three different volume models, namely the exponential (UV) model extended by an additional vertical shift parameter, the Gaussian model, and the Weibull model, were compared to the data. All of them are able to describe the data better than the conventional UV model, which is forced to start at the surface and thus has less flexibility. This is in agreement with previous studies that concluded that interferometric phase center depths cannot be explained with a UV model without shift [5], [9]. The present analysis illustrates the need for this type of shift, as tomographic measurements revealed that the first 1-5 m meters below the surface are widely transparent.

The general conclusion is that simple models are able to describe the data, which opens the door for future model inversions. The UV model with a vertical shift is the preferred choice when looking for a model that is applicable to all investigated test sites, frequencies, and polarizations. It performs best among the tested models, particularly for simulating coherences. At the EGIG T05 test site, this model performs consistently best at all frequencies and polarizations, independent of whether vertical backscattering distributions or coherences are investigated. It is also the best choice for simulating coherences at the South Dome test site at C- and P-bands and performs also well at X- and L-bands. It is also the preferred model for vertical backscattering distributions at P-band.

Despite the overall good performance of the UV model with a vertical shift, the vertical backscattering distributions can be more accurately reproduced at South Dome at X-, C- and L-bands by the Weibull model. When the vertical backscattering distributions instead of coherences are investigated, vertical shifts have a stronger influence and thus also the interferometric phase center respectively the penetration bias. This has to be taken into account for applications that focus on the InSAR phase.

It is important to note that, for a given frequency and test site, the same model performs best or equally good across all polarizations, with only one exception. This consistency across polarizations is essential for Pol-InSAR approaches.

The vertical profiles in HH, VV and HV polarizations were also used to assess the validity of a random volume assumption i.e. the assumption that the vertical backscattering distribution of

the volume only component is – up to a constant scale (i.e. intensity) factor – polarization independent. This would significantly simplify the inversion problem in a multi-polarimetric context by reducing the number of polarization dependent model parameters. The obtained profiles, however, indicate that the random volume assumption is, in a strict sense, not valid for the two considered test sites. On the one hand, the vertical profiles appear differently in the three polarizations, indicating a polarization dependent distribution of the scatterers. On the other hand, the differences between coherence magnitudes of the polarizations can be small, since large parts of the differences are caused by vertical shifts between the vertical profiles of the polarizations. The origin of vertical shifts between polarizations is not yet understood and one possible interpretation is the presence of polarized scattering that cannot be resolved by the vertical resolution of the tomograms. For applications focusing on coherence magnitudes, a random volume assumption could be still a sufficient approximation.

Generally, the interpretation of the profiles with volume models can be considered an approximation, as also more complex scattering scenarios, e.g. a multitude of adjoining layers, can appear as vertically distributed volumes at a finite tomographic resolution.

The tradeoff between the number of model parameters and the observation space of Pol-InSAR data has to be considered in future model inversion approaches. The EGIG T05 data can be considered an oriented volume scenario, which could be theoretically inverted with dual-baseline, full-pol SAR data based on the volume models presented in this paper. If dominant scattering layers are present, as it is the case at South Dome, the requirements on the observation space increase and a model inversion becomes more challenging. A potential approach is a random volume approximation and Dirac deltas for the layers. This scenario requires dual-baseline, full-pol SAR data for an inversion approach as well.

This paper focuses on only two test sites in the percolation zone. Therefore, the presented results are not necessarily valid for other glacier zones. Tomographic studies in the ablation zone have revealed very heterogeneous subsurface structures [18], [35], which might make different modeling approaches necessary. In the dry snow zone, where no refrozen melt features exist, no strong scattering layers, as observed at the South Dome test site, are expected. There, the volume scattering from the firn could potentially be described with the volume models presented in the paper. Unfortunately, the ARCTIC15 campaign did not cover sites in the dry snow zone, such that this hypothesis cannot be verified.

The tomographic subsurface assessment, the analysis of the polarimetric diversity, and the improved performance of the investigated volume models in this paper can provide the basis for subsurface structure retrievals and penetration bias estimations from Pol-InSAR data.

3.6 ACKNOWLEDGMENT

The authors would like to thank everyone involved in the ARCTIC15 campaign, which was conducted by DLR and ETH Zurich in cooperation with the Danish Defence Acquisition and Logistics Organization (DALO), and the Alfred-Wegener-Institute for providing the GPR system and general support for the campaign. Special thanks go to M. Keller (DLR) and Dr. S.

Leinss (ETH Zurich) for the acquisition and processing of the GNSS data and to Dr. M. Pardini (DLR) for the support regarding the tomographic processing.

3.7 REFERENCES

[1] D.G. Vaughan, J.C. Comiso, I. Allison, J. Carrasco, G. Kaser, R. Kwok, P. Mote, T. Murray, F. Paul, J. Ren, E. Rignot, O. Solomina, K. Steffen, and T. Zhang, "Observations: Cryosphere," in *Climate Change 2013: The Physical Science Basis. Contribution of Working Group I to the Fifth Assessment Report of the Intergovernmental Panel on Climate Change,* [Stocker, T.F., D. Qin, G.-K. Plattner, M. Tignor, S.K. Allen, J. Boschung, A. Nauels, Y. Xia, V. Bex and P.M. Midgley (eds.)]. Cambridge University Press, Cambridge, United Kingdom and New York, USA, 2013.

[2] B. Wessel, A. Bertram, A. Gruber, S. Bemm, and S. Dech, "A New High-Resolution Elevation Model of Greenland Derived from Tandem-X," *ISPRS Annals of Photogrammetry, Remote Sensing and Spatial Information Sciences*, vol. III–7, pp. 9–16, Jun. 2016.

[3] A. S. Gardner, G. Moholdt, J. G. Cogley, B. Wouters, A. A. Arendt, J. Wahr, E. Berthier, R. Hock, W. T. Pfeffer, G. Kaser, S. R. M. Ligtenberg, T. Bolch, M. J. Sharp, J. O. Hagen, M. R. van den Broeke, F. Paul, "A reconciled estimate of glacier contributions to sea level rise: 2003 to 2009," *Science*, vol. 340, pp. 852–857, May 2013.

[4] V. Helm, A. Humbert, and H. Miller, "Elevation and elevation change of Greenland and Antarctica derived from CryoSat-2," *The Cryosphere*, vol. 8, no. 4, pp. 1539–1559, 2014.

[5] G. Fischer, G. Parrella, K. P. Papathanassiou, and I. Hajnsek, "Sensitivity of polarimetric SAR interferometry data to different vertical subsurface structures of the Greenland ice sheet," in *Proceedings of IGARSS*, Forth Worth, USA, 2017, pp. 3581–3584.

[6] E. Rignot, K. Echelmeyer, and W. Krabill, "Penetration depth of interferometric synthetic aperture radar signals in snow and ice," *Geophysical Research Letters*, vol. 28, no. 18, pp. 3501–3504, Sep. 2001.

[7] E. W. Hoen and H. Zebker, "Penetration depths inferred from interferometric volume decorrelation observed over the Greenland ice sheet," *IEEE Transactions on Geoscience and Remote Sensing*, vol. 38, no. 6, pp. 2572–2583, Nov. 2000.

[8] P. Rizzoli, M. Martone, H. Rott, and A. Moreira, "Characterization of Snow Facies on the Greenland Ice Sheet Observed by TanDEM-X Interferometric SAR Data," *Remote Sensing,* vol. 9, no. 4, Mar. 2017

[9] J. Dall, K.P. Papathanassiou, and H. Skriver, "Polarimetric SAR interferometry applied to land ice: Modeling," in *Proceedings of EUSAR*, Ulm, Germany, 2004, pp. 247-250.

[10] J.J. Sharma, I. Hajnsek, and K.P. Papathanassiou, "Estimation of glacier ice extinction using long-wavelength airborne Pol-InSAR," *IEEE Transactions on Geoscience and Remote Sensing*, vol. 51, no. 6, pp. 3715-3732, Jun. 2013.

[11] S. Hensley, D. Moller, S. Oveisgharan, T. Michel, and X. Wu, "Ka-Band Mapping and Measurements of Interferometric Penetration of the Greenland Ice Sheets by the GLISTIN Radar," *IEEE Journal of Selected Topics in Applied Earth Observations and Remote Sensing*, vol. 9, no. 6, pp. 2436–2450, Jun. 2016.

[12] C. Mätzler, “Improved Born approximation for scattering of radiation in a granular medium,” *Journal of Applied Physics*, vol. 83, no. 11, pp. 6111–6117, Jun. 1998.

[13] S. Oveisgharan and H. Zebker, “Estimating snow accumulation from InSAR correlation observations,” *IEEE Transactions on Geoscience and Remote Sensing*, vol. 45, no. 1, pp. 10–20, Jan. 2007.

[14] G. Fischer, K. P. Papathanassiou and I. Hajnsek, "Modeling Multifrequency Pol-InSAR Data From the Percolation Zone of the Greenland Ice Sheet," *IEEE Transactions on Geoscience and Remote Sensing*, vol. 57, no. 4, pp. 1963-1976, April 2019.

[15] B. Rekioua, M. Davy, L. Ferro-Famil, and S. Tebaldini, “Snowpack permittivity profile retrieval from tomographic SAR data,” *Comptes Rendus Physique*, vol. 18, no. 1, pp. 57–65, Jan. 2017.

[16] T. G. Yitayew, L. Ferro-Famil, T. Eltoft, and S. Tebaldini, “Lake and Fjord Ice Imaging Using a Multifrequency Ground-Based Tomographic SAR System,” *IEEE Journal of Selected Topics in Applied Earth Observations and Remote Sensing*, vol. 10, no. 10, pp. 4457–4468, Oct. 2017.

[17] S. Tebaldini, T. Nagler, H. Rott, and A. Heilig, “Imaging the Internal Structure of an Alpine Glacier via L-Band Airborne SAR Tomography,” *IEEE Transactions on Geoscience and Remote Sensing*, vol. 54, no. 12, pp. 7197–7209, Dec. 2016.

[18] F. Banda, J. Dall, and S. Tebaldini, “Single and Multipolarimetric P-Band SAR Tomography of Subsurface Ice Structure,” *IEEE Transactions on Geoscience and Remote Sensing*, vol. 54, no. 5, pp. 2832–2845, May 2016.

[19] C. S. Benson, *Stratigraphic Studies in the Snow and Firn of the Greenland Ice Sheet*, U.S. Army Snow, Ice and Permafrost Research Establishment, Aug. 1996.

[20] R. Horn, A. Nottensteiner, and R. Scheiber, “F-SAR – DLR’s advanced airborne SAR system onboard DO228,” in *Proceedings of EUSAR*, Friedrichshafen, Germany, Jun. 2-5, 2008, pp. 195-198.

[21] A. Reigber, P. Prats, and J. J. Mallorqui, “Refined Estimation of Time-Varying Baseline Errors in Airborne SAR Interferometry,” *IEEE Geoscience and Remote Sensing Letters*, vol. 3, no. 1, pp. 145–149, Jan. 2006.

[22] J. Freitag, S. Kipfstuhl, S. Hoerz, L. Eling, B. Vinther, and T. Popp, “Melt layer statistic of two firn cores recently drilled at Dye3 and South Dome in the dry snow zone of Southern Greenland,” *presented at the EGU General Assembly*, Vienna, Austria, Apr./May 2014.

[23] K. Steffen, J. E. Box, and W. Abdalati, “Greenland Climate Network: GC-Net,” in *CRREL 96-27 Special Report on Glaciers, Ice Sheets and Volcanoes, trib. to M. Meier*, S. C. Colbeck, Ed., pp. 98-103, 1996.

[24] S.L. Buchardt, H.B. Clausen, B. M. Vinther, and D. Dahl-Jensen, “Investigating the past and recent δ^{18}O-accumulation relationship seen in Greenland ice cores,” *Climate of the Past*, vol. 8, no. 6, pp. 2053–2059, Dec. 2012.

[25] V. Helm, W. Rack, R. Cullen, P. Nienow, D. Mair, V. Parry, and D. J. Wingham, “Winter accumulation in the percolation zone of Greenland measured by airborne radar altimeter,” *Geophysical Research Letters*, vol. 34, no. 6, Mar. 2007.

[26] A. Reigber and A. Moreira, “First demonstration of airborne SAR tomography using multibaseline L-band data,” *IEEE Transactions on Geoscience and Remote Sensing*, vol. 38, no. 5, pp. 2142–2152, Sep. 2000.

[27] C. Mätzler, "Applications of the interaction of microwaves with the natural snow cover," *Remote Sensing Reviews*, vol. 2, pp. 259-387, 1987.

[28] F. Gini, F. Lombardini, and M. Montanari, "Layover solution in multibaseline SAR interferometry," *IEEE Transactions on Aerospace and Electronic Systems*, vol. 38, no. 4, pp. 1344–1356, Oct. 2002.

[29] H. Joerg, M. Pardini, I. Hajnsek and K.P. Papathanassiou, "On the Separation of Ground and Volume Scattering Using Multibaseline SAR Data," *IEEE Geoscience and Remote Sensing Letters*, vol. 14, no. 9, pp. 1570-1574, Sept. 2017.

[30] F. Garestier and T. Le Toan, "Forest Modeling For Height Inversion Using Single-Baseline InSAR/Pol-InSAR Data," *IEEE Transactions on Geoscience and Remote Sensing*, vol. 48, no. 3, pp. 1528–1539, Mar. 2010.

[31] G. Fischer, M. Pardini, G. Parrella, K. P. Papathanassiou, and I. Hajnsek, "Cancellation of Dominant Scattering Layers in Greenland's Subsurface for the Characterization of Ice Volumes," in *Proceedings of EUSAR*, Aachen, Germany, Jun. 4-7, 2018.

[32] R. Schmidt, "Multiple emitter location and signal parameter estimation," *IEEE Transactions on Antennas and Propagation*, vol. 34, no. 3, pp. 276–280, Mar. 1986.

[33] T. Marzetta, "A new interpretation of Capon's maximum likelihood method of frequency-wavenumber spectral estimation," *IEEE Transactions on Acoustics, Speech, and Signal Processing*, vol. 31, no. 2, pp. 445–449, Apr. 1983.

[34] M. S. Seymour and I. G. Cumming, "Maximum likelihood estimation for SAR interferometry," in *Proceedings of IGARSS*, Pasadena, CA, USA, 1994, vol. 4, pp. 2272–2275.

[35] M. Pardini, G. Parrella, G. Fischer, and K. Papathanassiou, "A Multi-Frequency SAR Tomographic Characterization of Sub- Surface Ice Volumes," in *Proceedings of EUSAR*, Hamburg, Germany, Jun. 6-9, 2016

4 MODELING AND COMPENSATION OF THE PENETRATION BIAS IN INSAR DEMS OF ICE SHEETS AT DIFFERENT FREQUENCIES

G. Fischer, K. P. Papathanassiou, and I. Hajnsek

IEEE Journal of Selected Topics in Applied Earth Observations and Remote Sensing

Submitted October 2019.

This chapter is a pre-print of the submitted paper.

The author's contributions:

- Interferometric processing and analysis of the SAR data.
- Implementation and assessment of the model inversions.
- Development of the Weibull model inversion technique.
- Analysis and interpretation of penetration bias modeling and compensation.
- Writing of the manuscript.

The co-authors' contributions:

- I. Hajnsek and K. P. Papathanassiou provided guidance throughout the research.
- I. Hajnsek and K. P. Papathanassiou contributed to the main ideas, the discussion of the results, and reviewed the manuscript.

MODELING AND COMPENSATION OF THE PENETRATION BIAS IN INSAR DEMS OF ICE SHEETS AT DIFFERENT FREQUENCIES

Georg Fischer[1,2], Konstantinos P. Papathanassiou[1], and Irena Hajnsek[1,2]
[1] German Aerospace Center, Microwaves and Radar Institute, Wessling, Germany
[2] ETH Zurich, Institute of Environmental Engineering, Zurich, Switzerland

Abstract

Synthetic Aperture Radar Interferometry (InSAR) is able to provide important information for the characterization of the surface topography of glaciers and ice sheets. However, due to the inherent penetration of microwaves into dry snow, firn, and ice, InSAR elevation models are affected by a penetration bias. The fact that this bias depends on the snow and ice conditions as well as interferometric acquisition parameters complicates its assessment and makes it also an error source when measuring changes in topography. Recent studies indicated the potential for model based compensation of this penetration bias. This paper follows this approach and investigates two different subsurface volume models for this task. Single-channel and polarimetric approaches are discussed for random and oriented volume scenarios. The model performance is assessed on two test sites in the percolation zone of the Greenland ice sheet using fully polarimetric airborne X-, C-, L-, and P-band InSAR data. The results indicate that simple models are able to partially compensate the penetration bias and provide more accurate topographic information than the interferometric phase center measurements alone.

4.1 INTRODUCTION

Digital elevation models (DEMs) of ice sheets derived during dry and frozen conditions from interferometric synthetic aperture radar (InSAR) measurements are affected by a bias, due to the penetration of microwave signals into snow, firn, and ice. The penetration bias is the difference between the surface elevation and the elevation of the interferometric phase center, which is located in the subsurface. In other words, the penetration bias in an InSAR DEM corresponds to the depth of the interferometric phase center. This depth depends on the snow and ice conditions, like the presence of refrozen ice inclusions within the firn, as well as on the acquisition parameters, i.e., polarization, frequency, incidence angle and interferometric baseline [1], [2]. Values of -1 m to -10 m at X-band (in the transition from the percolation to the dry snow zone in Greenland) [3], down to -13 m at C-band (with decreasing trend with increasing elevation in the percolation zone) [4], and -14 m at L-band (Greenland Summit) [5], with rare cases down to -120 m (cold marginal ice) [5], have been reported. These values indicate that the

penetration bias can dominate the uncertainties in mass balance estimations of glaciers and ice sheets [6] derived from InSAR DEMs [3]. Even more so, the seasonal and long term changes of geophysical subsurface properties as well as variations in interferometric acquisition geometry can make a direct interpretation of elevation changes in InSAR DEMs difficult. The penetration bias, and its temporal change, can be of the same order than the occurring surface elevation change. Therefore, the estimation and compensation of the penetration bias becomes essential.

Different approaches have been followed to address the bias by using indicators of constant penetration bias [7], selected acquisitions during melting periods in order to minimize penetration [8], and by empirically deriving altitude-dependent bias estimates [6]. The spatial and temporal differences in penetration, as well as the dependence of the bias on the interferometric baseline hamper these approaches. An alternative option to account for the bias is the use of scattering models. Studies indicated the potential of a model based estimation of the phase center depth directly from (polarimetric) InSAR data [1]. This paper follows this approach and investigates the ability of simple subsurface volume models to estimate and compensate the penetration bias.

A successful bias compensation has to consider four aspects. First, its absolute value, in case InSAR surface elevations are compared to DEMs derived from optical data or radar altimetry. Second, the temporal changes of the bias that are relevant for comparing InSAR DEMs acquired at different dates. Third, differences in penetration in InSAR DEMs derived at different frequencies or polarizations. Fourth, the baseline dependence of the bias in order to account for DEMs acquired with different acquisition geometries.

The significant baseline dependence of the phase center depth was described under the assumption of a uniform volume (UV) model in [1]. Therefore, the penetration bias at the same time, space, frequency, and polarization is different at different baselines. The experimental validation of these findings is reported in Section 4.3.

The relevant question is what model complexity is necessary to describe the baseline dependence and to compensate for the penetration bias. The modeling has to account for the vertical backscattering profile in the subsurface and should be applicable to different ice sheet areas. The assumption of a uniform volume described by a constant scattering coefficient in the subsurface, the UV model, was first used by [9] to estimate penetration depths from the coherence magnitude, without the comparison to measured phase center depths. However, phase centers often appear deeper in experimental data than a UV model predicts [2], [10].

More recent studies have shown that a feasible approach for modeling the vertical backscattering profile in the subsurface of ice sheets is by combining a volume model with distinct subsurface layers represented by Dirac deltas [11]. However, this increases the parametric complexity of the vertical backscattering profile (i.e., the number of model parameters that need to be estimated) and makes its inversion only possible in the context of full polarimetric multi-baseline observation spaces. However, with respect to the estimation of the phase center depth, which requires only the estimation of the centroid of the vertical backscattering profile, the modeling can be simplified. Volume models, which are invertible

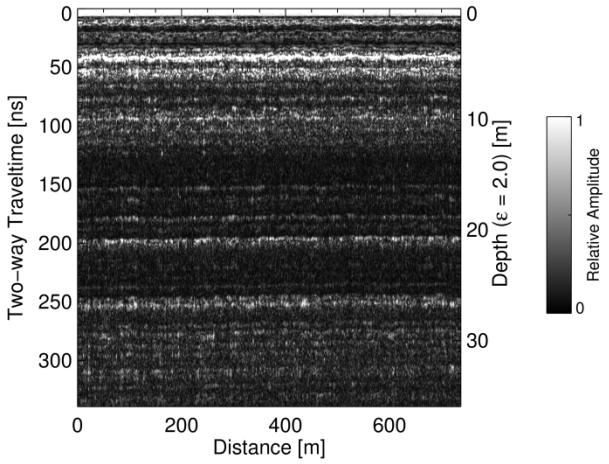

Fig. 1. Amplitude envelope of GPR profiles at South Dome, where several layers with varying backscattered power are visible.

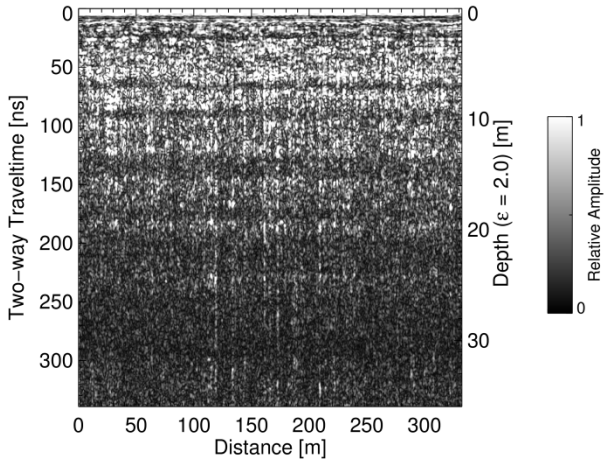

Fig. 2. Amplitude envelope of GPR profiles at EGIG T05, with a relatively homogeneous backscattering level that decreases with depth.

also in lower dimensional observation spaces as single-baseline InSAR data, can approximate the phase center depth and its dependence on the baseline.

The goal of this paper is to quantify how accurately simple interferometric volume models can estimate and compensate the penetration bias in InSAR ice sheet surface elevations. First, the phase center depth and its spatial baseline dependence is characterized at different frequencies and polarizations by using airborne InSAR data acquired at two different test sites on the Greenland ice sheet. The two test sites are characterized by different subsurface structures, which allow assessing the applicability of the investigated models to different scattering scenarios. Then the performance of UV model inversions to compensate the penetration bias is investigated. Approaches based on single channel as well as fully polarimetric InSAR data are discussed. An alternative, more flexible, model based on the Weibull function, is introduced and compared. The presented approaches address both random and oriented volume assumptions, since the vertical backscattering profiles in ice sheets were shown to be polarization dependent [12]. The accuracy of the penetration bias estimates is assessed by comparison with GNSS measurements of the surface elevation.

4.2 DATA

Experimental airborne SAR data were acquired during the ARCTIC15 campaign in April and May 2015 on the Greenland ice sheet with DLR's F-SAR system. This study focusses on two test sites, both located in the percolation zone, but with different subsurface structures. The first test site, South Dome (63.52° N, 44.54° W, 2868 m a. s. l), experiences only limited melting during summer, which leads to refrozen ice inclusions within the firn that appear as layers at specific depths, which are visible in the ground penetrating radar (GPR) data in Fig. 1. The second test site, EGIG T05 (69.87° N, 47.13° W, 1938 m a. s. l), is characterized by an abundance of ice inclusions within the firn, due to more refrozen melt water because of its lower

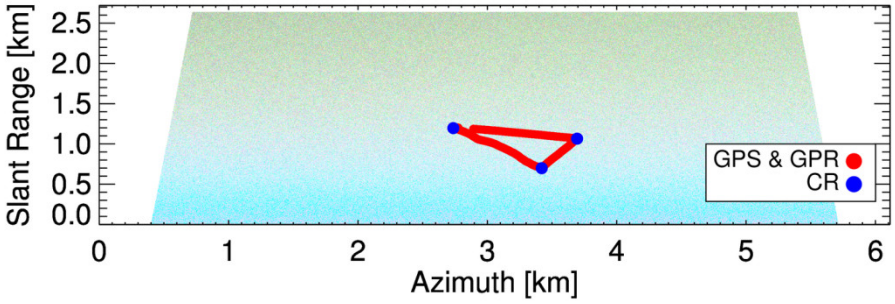

Fig. 3. Polarimetric image of the L-band data acquired at South Dome shown in the Pauli basis (HH+VV: blue, HH-VV: red, HV: green). The location of the ground measurements is indicated. Similar ground measurements are available at the EGIG T05 test site.

TABLE I
SOUTH DOME

Band	Freq. [GHz]	# Tracks	Nom. BL [m]	Res. Az. x Rg. [m]
X	9.6	9	2-35	0.5 x 0.5
C	5.3	7	5-35	0.5 x 0.5
L	1.3	6	10-85	0.6 x 1.3
P	0.44	8	10-270	1.0 x 3.8

EGIG T05

Band	Freq. [GHz]	# Tracks	Nom. BL [m]	Res. Az. x Rg. [m]
X	9.6	11	2-40	0.5 x 0.5
C	5.3	9	5-40	0.5 x 0.5
L	1.3	9	5-90	0.6 x 1.3
P	0.44	9	10-270	1.0 x 3.8

Summary of SAR acquisition parameters at both test sites. The nominal baselines are horizontal baselines flown at 3000 m above ground. At X-band, a second antenna provided an additional 1.7 m vertical baseline on two of the tracks. The azimuth and slant range resolution is single-look.

elevation. This leads to a more homogeneous vertical backscattering structure, which is visible in the GPR data in Fig. 2. More information about the campaign including SAR tomograms can be found in [11] and [12].

In this study, fully polarimetric, multi-baseline SAR data at X-, C-, L-, and P-bands, acquired along six to nine parallel flight tracks are used. The acquisitions are summarized in Table I. The snow and firn conditions are considered stable during the acquisition period and temporal decorrelation can be neglected [11].

GNSS measurements were acquired on both test sites along a triangular path in the scene center, see Fig. 3, which provide the surface reference height. The interferometric phase centers are derived at the locations of the GNSS measurements. The corner reflectors were used to validate and refine the multi-baseline interferometric phase calibration [13].

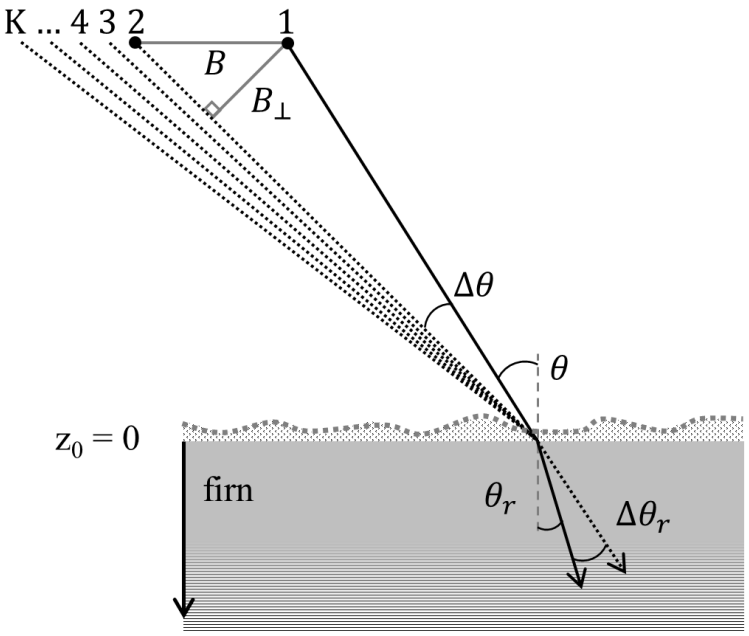

Fig. 4. Multi-baseline interferometric geometry with K acquisitions.

4.3 BASELINE DEPENDENCE OF PHASE CENTERS

The interferometric phase $\angle\gamma$ is derived from the complex interferometric coherence γ

$$\gamma(\vec{w}) = \frac{\langle s_1(\vec{w}) s_2^*(\vec{w})\rangle}{\sqrt{\langle s_1(\vec{w}) s_1^*(\vec{w})\rangle \langle s_2(\vec{w}) s_2^*(\vec{w})\rangle}} \tag{1}$$

obtained from the interferometric image pair s_1 and s_2 at a given polarization $\vec{w}$ [14]. The phase center location is given by $\angle\gamma / k_{zVol}$, where the vertical wavenumber k_{zVol} is [15]

$$k_{zVol} = \frac{4\pi\sqrt{\epsilon_r}}{\lambda} \frac{\Delta\theta_r}{sin\theta_r}, \tag{2}$$

which describes the variation of the interferometric phase $\angle\gamma$ as a function of depth z. The permittivity of the volume ϵ_r is set to 2.0 for this analysis based on its relationship to density [16] measured in firn cores [17]. λ is the wavelength in free space. θ_r is the refracted incidence angle within the firn volume. $\Delta\theta_r$ is the difference in θ_r introduced by the spatial baseline between the acquisitions, as depicted in Fig. 4.

After conventional InSAR processing and without temporal decorrelation, the coherence γ depends on the vertical backscattering profile $\sigma_v(z)$

$$\gamma(\vec{w}) = e^{ik_z z_0} \frac{\int_{-\infty}^{0} \sigma_v(z,\vec{w}) e^{ik_{zVol} z} dz}{\int_{-\infty}^{0} \sigma_v(z,\vec{w}) dz}. \tag{3}$$

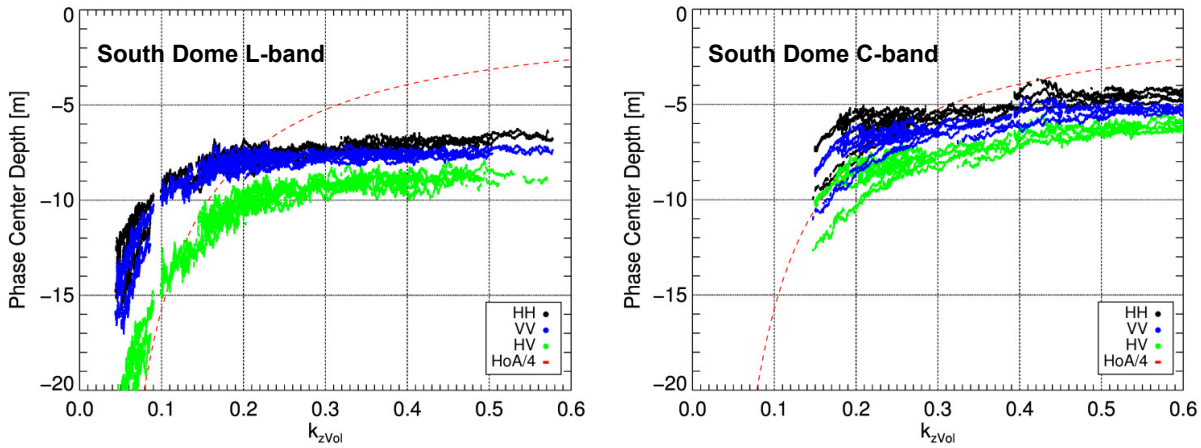

Fig. 5. Phase center depths referenced to GNSS measurements from several baselines of the South Dome data at L-band (left) and C-band (right) in three polarizations. The lower theoretical limit, $HoA/4$, of a UV model is also shown.

The depth of the phase center is related to the effective centroid of the vertical backscattering profile $\sigma_v(z)$ in the subsurface, while the magnitude of the interferometric coherence is related to the vertical spread of $\sigma_v(z)$. In an oriented volume scenario, $\sigma_v(z)$ depends on polarization $\vec{w}$, while $\sigma_v(z)$ is independent of $\vec{w}$ for a random volume.

The interferometric phase is referenced to corner reflectors and GNSS measurements at the surface. The surface is defined at $z_0 = 0\ m$ so that the phase center location $\angle\gamma/k_{zVol}$ is directly the phase center depth, which is equal to the penetration bias of an InSAR DEM. The phase centers are measured at a wide range of k_{zVol} at the locations of the GNSS measurements within the SAR scene, shown in Fig. 3. Small k_{zVol} variations in the set of samples derived from one baseline mainly come from small differences in incidence angle between the GNSS locations. In addition, larger k_{zVol} variations are achieved by using different baselines. The analysis is restricted to samples with $k_{zVol} < 0.6$ and $|\gamma| > 0.1$.

The phase center depths shown in Fig. 5 for South Dome L- and C-band data at HH, VV, and HV polarizations are derived from multiple baselines which overlap in their k_{zVol}-range. The L-band phase centers at small k_{zVol} are up to a factor of 2 deeper than at larger k_{zVol}, even though they are from the same set of GNSS locations. A variation in interferometric baseline can change the penetration bias by up to 10 m in this example. The baseline dependence leads to a strong phase center depth variation mainly for $k_{zVol} < 0.2$, with a more stable behavior at higher k_{zVol}. The co-polarized channels are very similar and the VV phase centers are about 1 m deeper than at HH. In contrast, the HV phase centers are 3-7 m deeper.

South Dome C-band phase centers can be derived only for $k_{zVol} > 0.15$ with the available baselines. They are about 2-3 m closer to the surface than at L-band, but the difference is expected to be larger for smaller k_{zVol}.

Phase center depths at the EGIG T05 test site in L- and C-band are shown in Fig. 6. They appear less densely sampled than at South Dome because a smaller amount of GNSS measurements was acquired at EGIG T05. This is related to a shorter GNSS track, which leads also to a smaller k_{zVol} variation for each baseline, causing gaps in k_{zVol}. The EGIG T05 phase

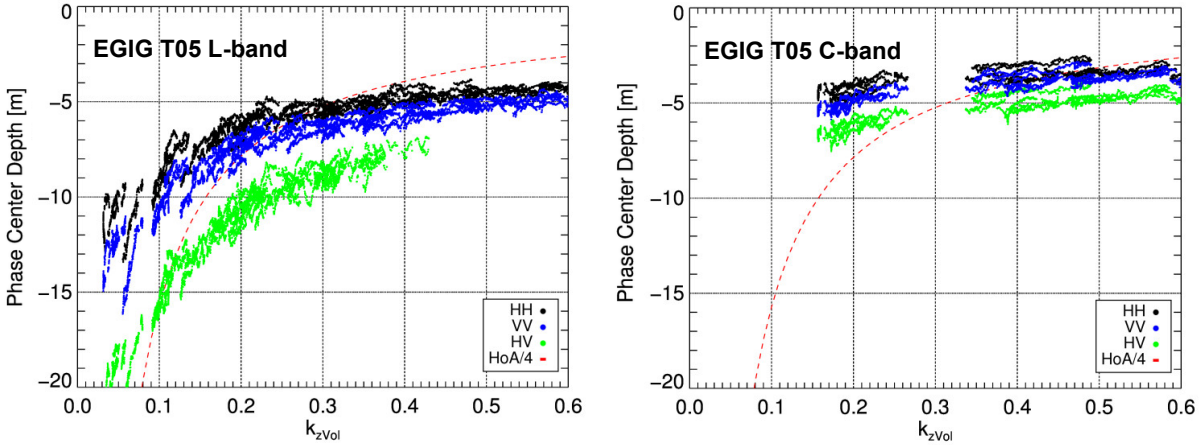

Fig. 6. Phase center depths referenced to GNSS measurements from several baselines of the EGIG T05 data at L-band (left) and C-band (right) in three polarizations. The lower theoretical limit, $HoA/4$, of a UV model is also shown.

center depths are on average 1-2 m closer to the surface than their South Dome counterparts. This comes from the larger amount of refrozen ice inclusions in the subsurface, which leads to a more homogeneous scattering closer to the surface than at South Dome [12]. This homogeneous subsurface scattering behavior fits better to the assumptions of the UV model, therefore the EGIG T05 L-band phase centers follow closer the UV model indicated by the red dashed line. The EGIG T05 L-band phase center depths at HV at higher k_{zVol} values are not shown as their coherence magnitudes are below 0.1.

The baseline dependence is a result of the Fourier transform of the non-symmetric $\sigma_v(z)$ in (3), which is complex valued and has a phase that changes with sampling frequency k_{zVol} [18]. A more descriptive interpretation is in terms of the phase wrapping of deeper scattering contributions with increasing k_{zVol}. Accordingly, deeper scatterers contribute with the same phase as scatterers just below the surface. This moves the phase center depth upwards with increasing k_{zVol}. Phase centers of a UV model cannot be deeper than a quarter of the height of ambiguity, due to this effect [1]. This limit is also shown by the red dashed line in Fig. 5 and Fig. 6. The phase centers roughly follow the theoretical limit, but are often deeper than the UV model predicts.

Note that there are small, but visible, residual phase offsets in the data. For instance, the two "lines" at each polarization in the South Dome C-band phase center depths in Fig. 5 at $k_{zVol} = 0.15$ come from two different baselines, which cover the same k_{zVol} range. The difference of about 2 m between the phase center depths derived from these two baselines is due to the residual phase offsets. Similar, but smaller effects are also visible in the other data sets, for instance the small jumps of less than 1 m at $k_{zVol} = 0.13$ in the South Dome L-band data.

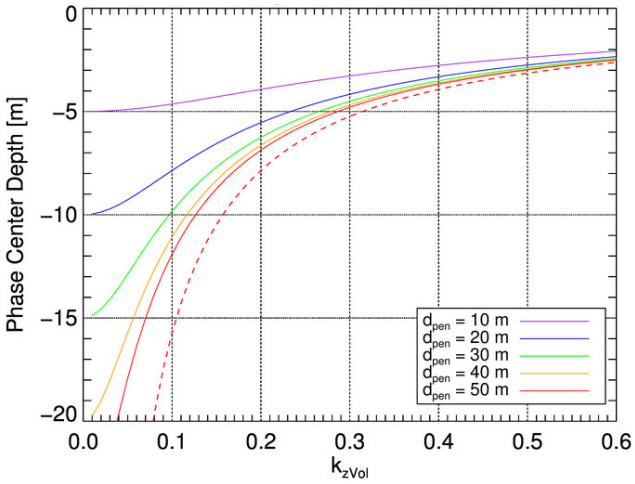

Fig. 7. Simulated phase center depths for the UV model with different d_{pen}.

4.4 Modeling and Inversion

Simulations of the vertical backscattering profile with the UV model [9] and the Weibull [12] model are used to investigate the modeling and compensation of the penetration bias. For the UV model, a single-polarization and full-polarization inversion are tested. For the Weibull model, a full-polarization inversion is analyzed, as its complexity does not allow a single-polarization inversion.

4.4.1 Uniform Volume Model

Assuming a uniform volume of scatterers with a constant extinction coefficient $\kappa_e(\vec{w})$ [9], the vertical backscattering function $\sigma_v(z)$ in (3) becomes exponential

$$\sigma_{uv}(z,\vec{w}) = \sigma_v^0(\vec{w})\mathrm{e}^{\frac{2z\kappa_e(\vec{w})}{cos\theta_r}} = \sigma_v^0(\vec{w})\mathrm{e}^{\frac{2z}{d_{pen}(\vec{w})}}, \tag{4}$$

where $\sigma_v^0(\vec{w})$ is the nominal backscatter power per unit volume at a given polarization $\vec{w}$ and the extinction coefficient $\kappa_e(\vec{w})$ accounts for both scattering and absorption losses. Parameterizing with the one-way penetration depth d_{pen}, which is inversely related to κ_e through $\kappa_e = cos(\theta_r)/d_{pen}$ and inserting (4) into (3) leads to γ_{uv} for a UV model [9]

$$\gamma_{uv}(\vec{w}) = e^{ik_z z_0}\frac{1}{1+\frac{id_{pen}(\vec{w})k_{zVol}}{2}}. \tag{5}$$

The phase center depths for a UV model are shown in Fig. 7, simulated for different d_{pen} and $z_0 = 0\ m$. A stronger baseline dependence for deeper penetration is indicated, which agrees with the stronger baseline dependence of the deeper HV phase centers in Fig. 5.

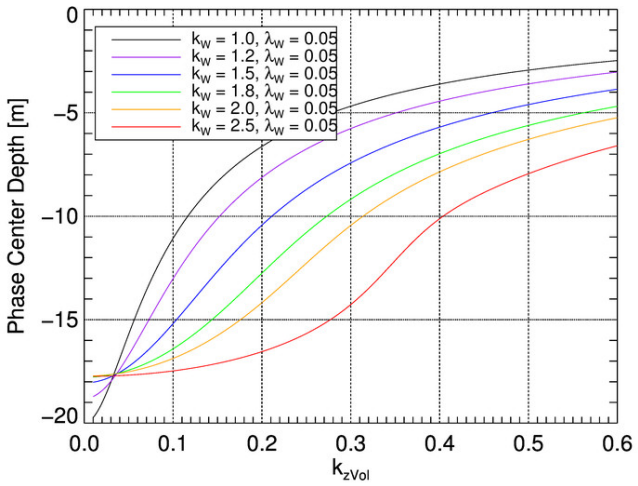

Fig. 8. Simulated phase center depths for a Weibull model with $\lambda_w = 0.05$ and varying k_w.

4.4.2 Weibull Volume Model

The Weibull function allows more flexible shapes for the vertical profile with

$$\sigma_w(z) = \lambda_w k_w (\lambda_w z)^{k_w - 1} e^{-(\lambda_w z)^{k_w}}. \tag{6}$$

The scale parameter λ_w is similar, but not identical, to the extinction coefficient $\kappa_e(\vec{w})$ in (4). k_w is the shape parameter and $k_w = 1$ leads to an exponential, $k_w = 2$ to a Rayleigh distribution and $k_w \approx 3.6$ approximates a Gaussian. The integrals in (3) are numerically solved in the interval $[0, \infty]$ using (6), as closed form solutions are only available for particular k_w values.

Simulated phase center depths for varying k_w of the Weibull model are shown in Fig. 8. It is evident that the two model parameters of the Weibull function, compared to one parameter in the UV model, provide increased flexibility in describing the baseline dependence of phase center depths.

4.4.3 Uniform Volume Inversion

The inversion of the penetration bias using the UV model is straight forward. While the phase center depth obviously depends on the penetration depth d_{pen}, see Fig. 7, the relationship between the phase $\angle\gamma_{uv}$ and the magnitude $|\gamma_{uv}|$ of the complex coherence is always the same and describes a semi-circle in the unit circle, given by the black line in Fig. 12. As a result, $\angle\gamma_{uv}$ can be derived from $|\gamma_{uv}|$ independently of d_{pen} [1]

$$\angle\gamma_{uv} = tan^{-1}\left(\sqrt{\frac{1}{|\gamma_{uv}|^2} - 1}\right). \tag{7}$$

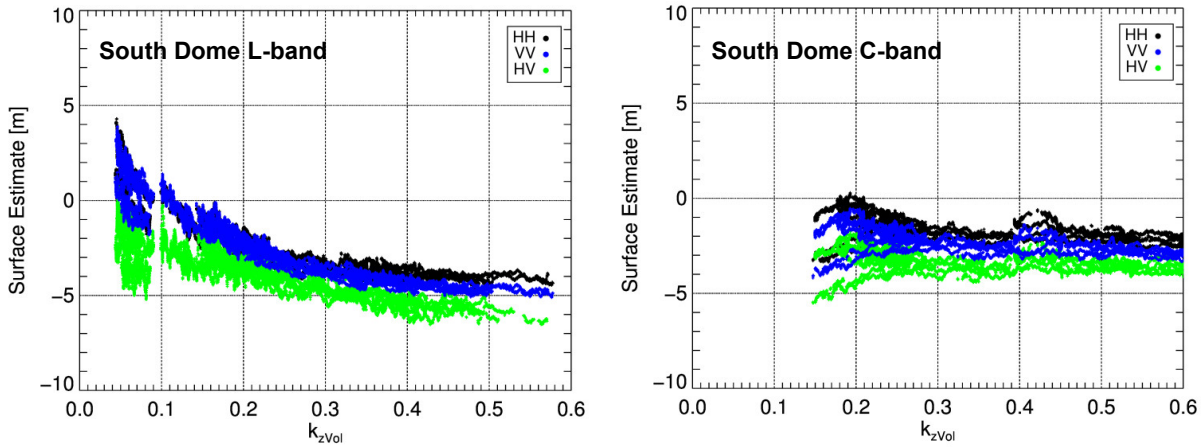

Fig. 9. UV surface estimates from South Dome L-band (left) and C-band (right) coherences from single channel UV inversions limited to $|\gamma| > 0.1$.

This allows the estimation of the phase from only a single coherence magnitude. The compensation of the penetration bias is then performed by subtracting this phase term from the measured phase.

Results from single channel UV inversions are shown for the South Dome data in Fig. 9. The surface estimates, despite being not exactly at $z = 0\,m$, provide more accurate topographic information than the corresponding phase centers in Fig. 5. The baseline dependence is partially compensated. At L-band, the UV model predicts a stronger baseline dependence than what is found in the data, which can be seen by comparing the simulations in Fig. 7 with Fig. 5. Therefore, while the phase center depths around $k_{zVol} = 0.1$ in Fig. 5 are accurately compensated with surface estimates around 0 m in Fig. 9, the surface estimates at higher k_{zVol} values are still a few meters below the surface. For instance, the UV model predicts only 2.5 m at $k_{zVol} = 0.6$, so that the HH phase center depths of -6.5 m in Fig. 5 can only be compensated to a surface estimate at -4 m in Fig. 9. The surface estimates based on the single channel UV inversion are even overestimated at the smaller k_{zVol} values. In contrast, the baseline dependence of the South Dome C-band phase center depths (Fig. 5) is accurately compensated by the UV surface estimates in Fig. 9 and the UV surface estimates are clearly closer to the surface. Residual differences between polarizations remain.

The results from the UV model inversions for the EGIG T05 data are shown in Fig. 10. The EGIG T05 UV surface estimates at L-band show a better removal of the baseline dependence for $k_{zVol} > 0.1$ than at South Dome, which was expected, because the phase center depths agree better with the behavior of the UV model. In contrast, the overestimation of the surface location at smaller k_{zVol} values is even stronger. At C-band, the penetration bias and its baseline dependence is compensated to a large extent and some of the co-polarized estimates are at the surface at $z = 0\,m$. The set of surface estimates based on the baseline that provides the samples around $k_{zVol} = 0.2$ is slightly overestimated.

The surface location is overestimated in the L-band data at both test sites at small k_{zVol} values and a residual baseline dependence is visible. In a general sense, it appears that there are scattering components that the modeled vertical backscattering profile $\sigma_v(z)$ does not account

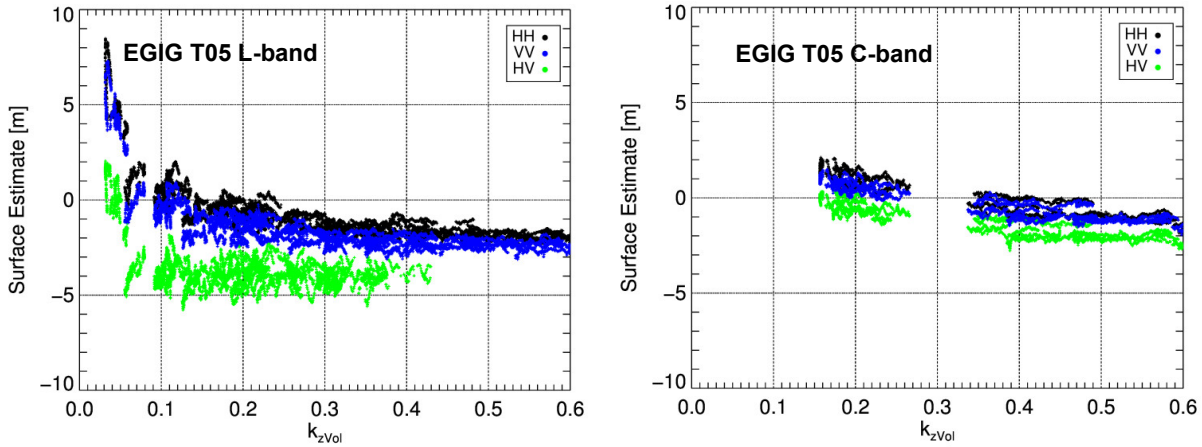

Fig. 10. UV surface estimates from EGIG T05 L-band (left) and C-band (right) coherences from single channel UV inversions limited to $|\gamma| > 0.1$.

for. The fact that the residual trend is similar in the data from both test sites contradicts an explanation based on the distinct subsurface layers at the South Dome test site. Additionally, simulations with Dirac deltas for the subsurface layers do not show the observed behavior. The origin appears to be rather in the dominant role of the coherence magnitude $|\gamma|$ in the model inversion, so that any deviation from the assumed exponential profile is fitted in terms of $|\gamma|$ at the cost of a larger deviation in the phase $\angle\gamma$. In other words, at small k_{zVol} values, the UV inversion predicts a too large phase term in (7) based on $|\gamma|$.

The effect of the residual phase offsets, mentioned in Section 4.3, are again visible in Fig. 9 as differences of 1-2 m between the sets of surface estimates derived from different baselines. A slightly different residual phase calibration effect is visible in the surface estimates with the UV model for the EGIG T05 L-band data in Fig. 10. The set of samples from one baseline that is around $k_{zVol} = 0.08$ is on average consistent with the results from other baselines, but shows an opposing trend within the set of samples.

Note that the use of a permittivity value of $\epsilon_r = 2.0$, based on density information, for the calculation of k_{zVol} in (2) is not critical for the trends in the surface estimations. The effect of ϵ_r is largely compensated by the respective change in refracted incidence angle in (2). Even the use of extreme values of 1 (permittivity of air) and 3.15 (permittivity of solid glacier ice) shift the phase center depths and the surface estimations only by about 1 m with only a marginal effect on the trend.

The UV model inversion can be straight forwardly applied to a fully polarimetric observation space. Averaging the surface estimates from the UV inversion across different polarizations gives essentially the surface estimate of an oriented uniform volume with polarization dependent $d_{pen}(w)$. In the following we use the term "oriented" to characterize polarization dependent vertical backscattering profiles. The surface estimation with an oriented UV model is shown in Fig. 11 and was applied first only on HH, VV, and HV polarizations, and second, by exploiting the full polarimetric space of the coherence region, by randomly sampling $\vec{w}$ in (1) [14]. The oriented UV inversion is similar to the single-polarization result in Fig. 9, but clearly reduces the variability due to polarizations. Interestingly, the results barely differ

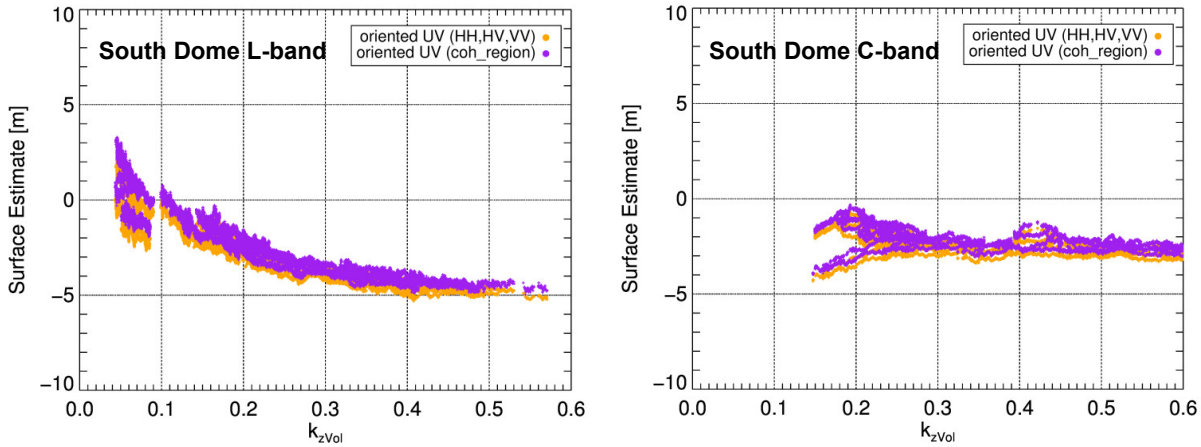

Fig. 11. Surface estimates from South Dome L-band (left) and C-band (right) coherences with the oriented volume UV inversion limited to $|\gamma| > 0.1$, based on fully polarimetric InSAR data.

between the inversion based on only HH, VV, and HV or the coherence region. The results based on the coherence region are only slightly higher, because the coherence regions are more densely populated around the HH and VV coherence loci, which leads to a stronger weighting of these polarization states.

4.4.4 Weibull Model Inversion

The Weibull model leads to a more challenging inversion problem. An oriented Weibull model, where both k_w and λ_w can vary with polarization, is not invertible with full polarimetric single-baseline InSAR data.

The tomographic analysis in [12] motivates the idea that the shape k_w is identical across polarizations and only λ_w varies. This can be exploited because numerical results show that the shape of the line of Weibull coherences in the unit circle depends only on k_w, while λ_w and k_{zVol} move the coherences along the line defined by k_w, as shown in Fig. 12.

Therefore, while the phase $\angle\gamma_w$ depends on the Weibull model, cf. Eq. (6),

$$\angle\gamma_w = f(k_w, \lambda_w, k_{zVol}, z_0), \tag{8}$$

when considering coherence magnitudes $|\gamma_w|$, it can be reduced to

$$\angle\gamma_w = f(k_w, |\gamma_w|, z_0). \tag{9}$$

Unfortunately, no analytic solution could be established for (9). However, the slope between $\angle\gamma$ and $|\gamma|$ for coherences measured at different polarizations can be compared to the same slope of simulated coherences in the respective $|\gamma|$ range. In this way, an estimate of the k_w parameter can be obtained by minimizing the difference in this slope between the data and simulations. The difference in phase between the complex mean of the measured and the simulated coherences in the $|\gamma|$-range of interest provides then the surface estimate $\hat{z}_0$.

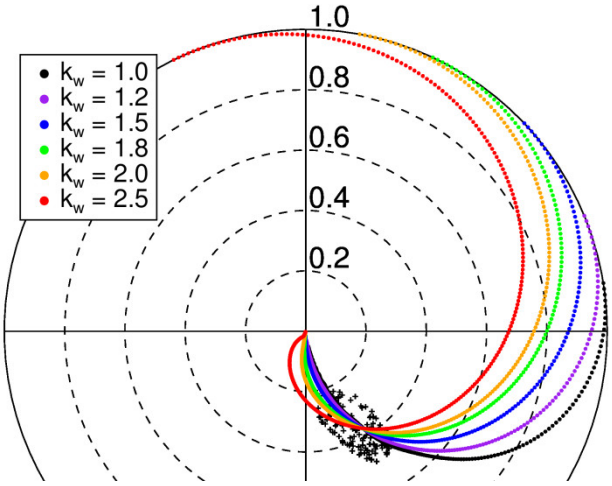

Fig. 12. Unit circle representation of coherences simulated with a Weibull model and fitted to an example coherence region from the South Dome L-band data (black crosses). $k_w = 1.0$ (black line), corresponds to a UV model.

Higher k_w parameters produce shapes of the Weibull coherences in the unit circle that overestimate the surface phase. This effect is visible in Fig. 12, when comparing the distance between the coherence region (black crosses) and the surface phase (intersection with the unit circle) of e.g. the red line. Constraining $k_w < 1.2$ is required for achieving reasonable results. Fig. 13 shows surface estimates with the Weibull inversion for the South Dome L- and C-band data based on HH, HV, and VV coherences as well as on full coherence regions, which largely overlap. The general behavior is similar to the oriented volume UV inversion in Fig. 11. At C-band, the Weibull results are slightly closer to the surface and the baseline dependence is equally good removed. However, at L-band, the surface is overestimated for small k_{zVol}, while for larger k_{zVol} the estimates are slightly closer to the surface than the UV estimates in Fig. 11. Similar observations can be made for the Weibull inversion of the EGIG T05 phase centers, which are not shown here.

4.5 Results

The phase center depths are compared to the surface estimates of the three investigated inversions in Fig. 14. The statistics are derived for all results with $k_{zVol} < 0.6$ and $|\gamma| > 0.1$. For instance, the boxplots of the phase center depths at South Dome in L-band in Fig. 14 are derived from the measurements shown in Fig. 5 (left). The upper and lower quartiles as well as the maximum and minimum values indicate the variability in the results including the baseline dependence.

The phase center depths show the expected behavior with deeper phase centers at longer wavelengths and in the HV channel compared to shorter wavelengths and the co-polarized channels, respectively. At X- and C-band, the phase centers at EGIG T05 are closer to the surface than at South Dome, as expected based on the more homogeneous scattering closer to the surface at EGIG T05, which is indicated by the GPR data (Fig. 2) and tomograms [12]. This

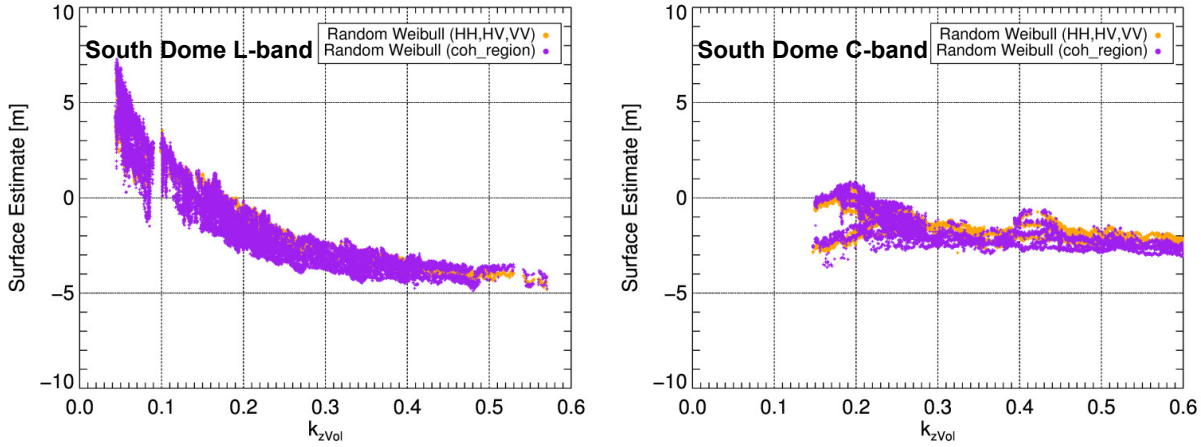

Fig. 13. Surface estimates from South Dome L-band (left) and C-band (right) coherences with the Weibull inversion constrained to $k_w < 1.2$, based on fully polarimetric InSAR data.

applies also to the co-polarized channels at L-band, but is the opposite for P-band. The subsurface at South Dome is characterized by dominant scattering layers, with very similar vertical backscattering profiles in L- and P-band [12]. This leads to very similar L- and P-band phase center depths, while the more homogeneous subsurface at EGIG T05 leads to P-band penetrating deeper than L-band.

The single-polarization inversion of the UV model provides already a good compensation of the median phase center depth and gives surface estimates which are only few meters below the real surface. Also the baseline dependence is reduced and the inversion results show a smaller variability than the phase center depths. The variability is further reduced by applying the oriented volume UV inversion to the interferometric coherences of all polarization channels.

The Weibull inversion needs to be constrained to $k_w < 1.2$ in order to limit overestimation. The Weibull inversions have a slightly larger variation in the surface estimates because of its tendency to overestimate the distance between the phase center and the surface, while the median values are closer to the real surface than for the UV inversions. The Weibull model therefore presents a way to account for the slight underestimation of the UV model, but is also prone to overestimation.

4.6 Discussion and Conclusion

The single-polarization UV inversion, which can be applied to any InSAR coherence, provides more accurate surface elevation than obtained by the measured interferometric phase center. For instance, the median value of the phase center depth of the South Dome L-band HH data in Fig. 14 is -7.8 m, while the median of the UV surface estimates is -2.3 m. This corresponds to a significant reduction in the penetration bias of an InSAR DEM. On average, the penetration bias is reduced by a factor of 2.5 to 6.5 in the investigated data. The variability of the UV surface estimates is reduced compared to the variability of the measured phase center depths. The compensation of the baseline dependence with a UV model was demonstrated. The remaining uncertainties come from a residual baseline dependence but also from the variance in

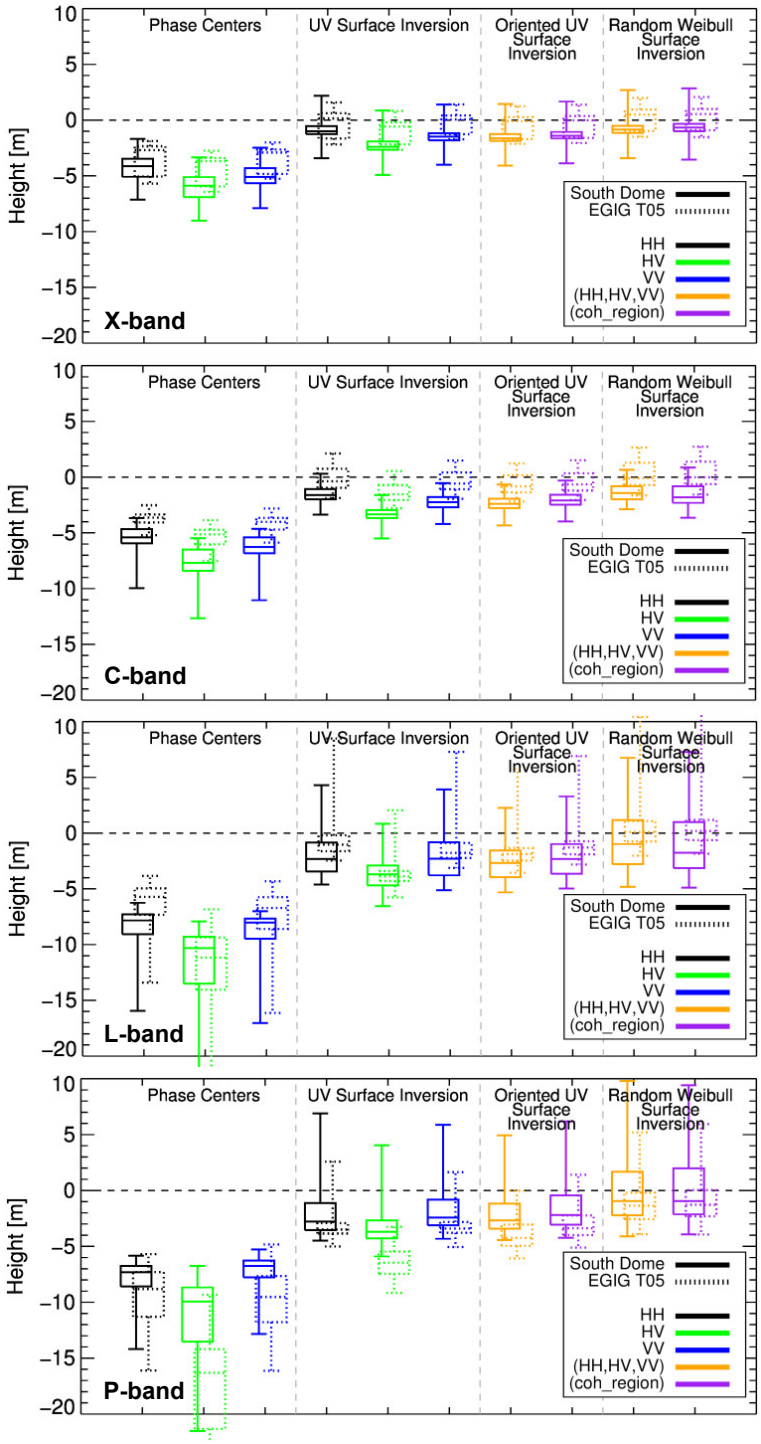

Fig. 14. Boxplots (Max, upper quartile, median, lower quartile, min) of the phase centers and different surface estimates at the South Dome and EGIG T05 test sites. From top to bottom: X-, C-, L-, and P-band. The Weibull inversion was constrained to $k_w < 1.2$.

the experimental data. A further reduction of the variability can be gained by applying an oriented volume UV inversion to polarimetric InSAR data. This combines the information from different polarizations and improves the result.

The Weibull inversion is introduced for a more flexible representation of the shape of the vertical backscattering profile. The Weibull inversion is helpful if the UV model underestimates the surface, because it can predict larger distances between the surface and the phase center.

However, the Weibull inversion overestimates the surface, making a constraint on the Weibull shape parameter k_w necessary. The Weibull model shows potential for better surface estimation than the UV model, but its inversion needs to be improved through further research.

Interestingly, the oriented volume UV and Weibull inversions perform very similarly based on the HH, HV, and VV coherences and based on a densely sampled coherence region even though the latter theoretically has a larger information content.

Given the performance of the UV inversion and because it can be applied to any single-polarization interferometric coherence, the main conclusion is that UV surface estimations should be preferred over the sole phase center information, as long as other decorrelation sources, e.g. temporal decorrelation, can be neglected or accounted for.

This is particularly true for the compensation of the absolute value of the penetration bias in case InSAR DEMs are compared to other sources of surface elevation. If two InSAR DEMs at different dates are compared, e.g. with a one year difference, only the temporal difference of the penetration bias is relevant. The presented approaches rely only on the coherences measured by each InSAR acquisition. A temporal change in penetration bias is related to changing scattering characteristics, which will affect the measured coherences accordingly. Therefore, also the temporal differences of the model based surface estimates are expected to be smaller than the temporal differences of the measured phase center depths. The same applies to InSAR DEMs acquired at different frequencies or polarizations. If InSAR DEMs are generated at the same snow and ice conditions and acquisitions parameters, except for a difference in baseline, which is a likely scenario for space borne SAR, only the baseline dependence of the penetration bias is relevant. The presented model inversions are able to compensate this effect to a varying extent depending on the frequency.

One has to accept that, in dry and frozen conditions, the first few meters of snow and firn can be transparent depending on the frequency. Tomographic analyzes showed that the thickness of this transparent part is between 1 m at X-band and 5 m at L- and P-bands in the investigated data [12]. Nevertheless, the inversion of a “radar surface”, which ignores this transparent part, provides more reliable topographic information over ice sheets than using the pure interferometric phase center information. The simple volume models investigated in this paper demonstrate the compensation of the penetration bias in InSAR DEMs. However, models of higher complexity could account for more aspects of subsurface scattering and improve the estimation performance, but their inversion requires also higher dimensional observation spaces. This could be addressed in the context of future SAR missions [19] that are able to provide polarimetric InSAR measurements of the same area at multiple baselines within few weeks.

4.7 ACKNOWLEDGMENT

The authors would like to thank everyone involved in the ARCTIC15 campaign, which was conducted by DLR and ETH Zurich in cooperation with the Danish Defence Acquisition and Logistics Organization (DALO).

4.8 REFERENCES

[1] J. Dall, "InSAR Elevation Bias Caused by Penetration Into Uniform Volumes," *IEEE Transactions on Geoscience and Remote Sensing*, vol. 45, no. 7, pp. 2319–2324, Jul. 2007.

[2] G. Fischer, G. Parrella, K. P. Papathanassiou, and I. Hajnsek, "Sensitivity of polarimetric SAR interferometry data to different vertical subsurface structures of the Greenland ice sheet," in *Proceedings of IGARSS*, Forth Worth, USA, 2017, pp. 3581–3584.

[3] B. Wessel, A. Bertram, A. Gruber, S. Bemm, and S. Dech, "A New High-Resolution Elevation Model of Greenland Derived from Tandem-X," *ISPRS Annals of Photogrammetry, Remote Sensing and Spatial Information Sciences*, vol. III–7, pp. 9–16, Jun. 2016.

[4] J. Dall, S. N. Madsen, K. Keller, and R. Forsberg, "Topography and penetration of the Greenland Ice Sheet measured with Airborne SAR Interferometry," *Geophysical Research Letters*, vol. 28, no. 9, pp. 1703–1706, May 2001.

[5] E. Rignot, K. Echelmeyer, and W. Krabill, "Penetration depth of interferometric synthetic aperture radar signals in snow and ice," *Geophysical Research Letters*, vol. 28, no. 18, pp. 3501–3504, Sep. 2001.

[6] J. Gardelle, E. Berthier, Y. Arnaud, and A. Kääb, "Region-wide glacier mass balances over the Pamir-Karakoram-Himalaya during 1999-2011," *The Cryosphere*, vol. 7, no. 4, pp. 1263–1286, Aug. 2013.

[7] H. Rott, W. A. Jaber, J. Wuite, S. Scheiblauer, D. Floricioiu, J. M. van Wessem, T. Nagler, N. Miranda, and M. R. van den Broeke, "Changing pattern of ice flow and mass balance for glaciers discharging into the Larsen A and B embayments, Antarctic Peninsula, 2011 to 2016," *The Cryosphere*, vol. 12, no. 4, pp. 1273–1291, Apr. 2018.

[8] W. Abdel Jaber, H. Rott, D. Floricioiu, J. Wuite, and N. Miranda, "Heterogeneous spatial and temporal pattern of surface elevation change and mass balance of the Patagonian icefields between 2000 and 2016," *The Cryosphere Discussions*, pp. 1–39, Dec. 2018.

[9] E. W. Hoen and H. Zebker, "Penetration depths inferred from interferometric volume decorrelation observed over the Greenland ice sheet," *IEEE Transactions on Geoscience and Remote Sensing*, vol. 38, no. 6, pp. 2572–2583, Nov. 2000.

[10] J. Dall, K.P. Papathanassiou, and H. Skriver, "Polarimetric SAR interferometry applied to land ice: Modeling," in *Proceedings of EUSAR*, Ulm, Germany, 2004, pp. 247-250.

[11] G. Fischer, K. P. Papathanassiou and I. Hajnsek, "Modeling Multifrequency Pol-InSAR Data From the Percolation Zone of the Greenland Ice Sheet," *IEEE Transactions on Geoscience and Remote Sensing*, vol. 57, no. 4, pp. 1963-1976, April 2019.

[12] G. Fischer, M. Jäger, K. P. Papathanassiou, and I. Hajnsek, "Modeling the Vertical Backscattering Distribution in the Percolation Zone of the Greenland Ice Sheet with SAR Tomography," *IEEE Journal of Selected Topics in Applied Earth Observations and Remote Sensing*, to be published.

[13] M. Jäger, R. Scheiber, and A. Reigber, "External Calibration of Multi-Channel SAR Sensors Based on the Pulse-by-Pulse Analysis of Range Compressed Data," in *Proceedings of EUSAR*, Aachen, Germany, Jun. 2018, pp. 75–78.

[14] S.R. Cloude and K.P. Papathanassiou, "Polarimetric SAR interferometry," *IEEE Transactions on Geoscience and Remote Sensing*, vol. 36, no. 5, pp. 1551-1565, Sept. 1998.

[15] J.J. Sharma, I. Hajnsek, and K.P. Papathanassiou, "Estimation of glacier ice extinction using long-wavelength airborne Pol-InSAR," *IEEE Transactions on Geoscience and Remote Sensing*, vol. 51, no. 6, pp. 3715-3732, Jun. 2013.

[16] C. Mätzler, "Applications of the interaction of microwaves with the natural snow cover," *Remote Sensing Reviews*, vol. 2, pp. 259-387, 1987.

[17] J. Freitag, S. Kipfstuhl, S. Hoerz, L. Eling, B. Vinther, and T. Popp, "Melt layer statistic of two firn cores recently drilled at Dye3 and South Dome in the dry snow zone of southern Greenland", presented at *EGU General Assembly*, Vienna, Austria, Apr. 27–May 2, 2014.

[18] R. N. Bracewell, *The Fourier transform and its applications*, 3rd ed. Boston: McGraw Hill, 2000.

[19] A. Moreira, G. Krieger, I. Hajnsek, K. Papathanassiou, M. Younis, P. Lopez-Dekker, S. Huber, M. Villano, M. Pardini, M. Eineder, F. De Zan, and A. Parizzi, "Tandem-L: A Highly Innovative Bistatic SAR Mission for Global Observation of Dynamic Processes on the Earth's Surface," *IEEE Geoscience and Remote Sensing Magazine*, vol. 3, no. 2, pp. 8–23, Jun. 2015.

5 SUMMARY AND CONCLUSIONS

This chapter starts with a general summary of the research contributions of this thesis. Then, the conclusions of all research contributions are described with respect to the main research objective, followed by conclusions on the specific questions stated in Section 1.6. Limitations of the investigated approaches are discussed as a part of the conclusions. The thesis is completed with implications and an outlook.

5.1 SUMMARY

The main objective of this thesis is the modeling of the vertical backscattering distribution in the subsurface of ice sheets for Pol-InSAR applications. The fundamentals and the state of the art are addressed in Chapter 1. On the one hand, the influence of the subsurface scattering on the interferometric coherences measured by InSAR and Pol-InSAR through the concept of volume decorrelation is well known. This is also the reason why the potential for subsurface information retrieval using Pol-InSAR has been mentioned in literature since many years. The same applies to the potential for compensating the penetration bias in InSAR DEMs. On the other hand, scattering models are required to describe and invert that relationship. This allows to characterize the subsurface scattering based on the limited observation space of Pol-InSAR measurements, but only very few related approaches have been published. Most of them are based on the assumption of a uniform signal extinction along depth in the subsurface, the uniform volume (UV) model. This model describes an exponential vertical backscattering distribution, which is a useful, yet strong simplification of the scattering scenario in the subsurface of an ice sheet.

This thesis improves the modeling and understanding of subsurface scattering effects on Pol-InSAR measurements based on the SAR data acquired during the airborne ARCTIC15 campaign in Greenland. This unique data set enabled investigations with InSAR, Pol-InSAR, and SAR tomography techniques at different frequencies, polarizations, and over a wide range of vertical wavenumbers k_{zVol}, due to the multi-baseline acquisitions. The goal was to develop simple models, with a limited number of parameters, to facilitate future inversion approaches. The modeling is targeted towards the compensation of the penetration bias in InSAR DEMs over glaciers and ice sheets and to support future subsurface information retrievals from Pol-InSAR data.

Chapter 2 "*Modeling Multifrequency Pol-InSAR Data From the Percolation Zone of the Greenland Ice Sheet*" introduces a multiple layer plus volume model. This allows the simulation and interpretation of the effect of distinct subsurface scattering layers on interferometric coherences. Such layers correspond to ice inclusions within the firn originating from the refreezing of melt water. In the upper percolation zone, they are found to be very limited in their vertical extent and can be modelled as Dirac deltas in the vertical backscattering distribution.

Simulations show how the layer contributions constructively and destructively interfere and generate a coherence undulation pattern in dependence of k_{zVol} that matches the InSAR data. The developed model allows the characterization of the subsurface layers from the InSAR data at different polarizations and frequencies. This comprises the layer-to-volume scattering ratio and the vertical distance between the layers, which was validated with GPR measurements.

While Chapter 2 focusses on the effects of distinct layers, the general vertical backscattering distribution is addressed in Chapter 3 "*Modeling the Vertical Backscattering Distribution in the Percolation Zone of the Greenland Ice Sheet with SAR Tomography*". This concerns the general vertical backscattering distribution either in the background behind the layers or in the case when no distinct layers are present. A layer attenuation procedure is applied to access the background volume contribution. Different parameterizations of the vertical backscattering distribution are investigated, namely the UV model with a vertical shift, a Gaussian and a Weibull distribution. Even though the Weibull function theoretically fits better to the vertical distributions motivated by physical scattering models, it turned out that the UV model with a vertical shift is generally the best to reproduce the interferometric coherences and the vertical profiles obtained from SAR tomography. This result is interesting, since this model still relies on the assumption of a uniform scattering extinction in the subsurface, but allows for a vertical shift that accounts for the first few transparent meters of winter snow and young firn below the surface.

The transparency of the surface and the first few meters, revealed by tomography, provided an update on previous assumptions made in Chapter 2 about the scattering from the surface. The main undulation pattern of the L-band coherences was interpreted in Chapter 2 by Dirac deltas at 0 m and -4.75 m, but an alternative explanation with layers at -4.75 m and -10 m was already provided. The latter was then confirmed by the tomograms in Chapter 3 and further coherence simulations [1]. The slightly larger layer separation explains the undulation pattern equally well and the difference is within the uncertainty of about 0.5 m due to the contribution of the background volume, as mentioned in Chapter 2.

The performance of the interferometric models in Chapter 3 motivated the model based compensation of the penetration bias in InSAR ice sheet surface elevation measurements in Chapter 4 "*Modeling and Compensation of the Penetration Bias in InSAR DEMs of Ice Sheets at Different Frequencies*". A single-polarization InSAR inversion of the UV model, an oriented UV model inversion based on Pol-InSAR data, and a novel random volume Weibull inversion based on Pol-InSAR data were investigated. In all cases, the model based surface elevation estimations are clearly more accurate than the sole InSAR phase center information, which is conventionally used to derive topographic information. On average, the penetration bias is reduced by a factor of 2.5 to 6.5 with the single-polarization UV model inversion, for instance from -7.8 m to -2.3 m in the L-band HH data at South Dome. The variance of the UV inversion can be further reduced by using fully polarimetric InSAR data in the oriented UV model inversion. The Weibull inversion provides a better average estimation of the surface across the investigated k_{zVol} range, but suffers from a larger variance, which is mainly a larger residual baseline dependence. The model based surface estimates of all three approaches are still below

the actual surface. However, the estimation of such a “radar surface” can be seen as a more reliable concept, ignoring the first few transparent meters. From a forward modeling perspective, this is equivalent to the UV model with a vertical shift. The presented UV model inversion is recommended to improve surface elevation information derived with (Pol-)InSAR, particularly at longer wavelengths.

5.2 CONCLUSIONS

The conclusions of the research conducted in this thesis are summarized by addressing the main research objective of this thesis: Improving the modeling of the vertical backscattering distribution in the subsurface of ice sheets and its effect on polarimetric interferometric SAR measurements.

In this thesis, several model improvements were investigated that can be divided into two aspects. First, the modeling of distinct scattering layers in the subsurface of the upper percolation zone originating from refrozen melt water within the firn column, and second, the improvement of the volume models.

The effect of layers can be accurately simulated by Dirac deltas in the modeled vertical backscattering distribution. This is particularly relevant for the interpretation of coherence magnitudes at higher k_{zVol} values, for instance in the context of the planned Tandem-L mission [2], where k_{zVol} values up to 0.6 are expected due to the larger baselines suitable for SAR tomography. At such an acquisition geometry, the destructive interference of subsurface layers can lead to very low coherence values, which would result in wrong interpretations based on the conventional UV model or any other pure volume model. The same is true for constructive interference, which leads to higher coherence values than volume models can explain. Therefore, future work towards subsurface information retrieval from Pol-InSAR data should consider such layer effects and can profit from the model improvements of this thesis.

Regarding the volume models, which describe the general vertical distribution of backscattering, the first conclusion is that simple models are able to interpret the data. This paves the way for future model inversions. All of the improved volume models investigated in this thesis are able to describe the data better than the conventional UV model, by accounting for distributions that are shifted or skewed towards deeper scattering contributions. In most cases, the RMSE between simulations and measurements is improved by at least a factor of 3. This is in agreement with previous studies, which concluded that measured interferometric phase center depths are deeper than the limits of the conventional UV model [3]. The Weibull model shows a good performance in comparison to the vertical scattering profiles derived with SAR tomography and matches well the distributions motivated by physical scattering models. However, following the assumption of a uniform scattering extinction but allowing for a vertical shift, by means of a shifted UV model, generally performs best among the volume models investigated in the thesis.

This thesis, therefore, improved the modeling of the vertical backscattering distributions in the subsurface of ice sheets for Pol-InSAR applications compared to the previous state of the art

of a uniform scattering extinction in the entirety of the subsurface. This was achieved by accounting for the first few transparent meters below the surface with vertical shifts in the UV model, by establishing the Weibull model for skewed vertical backscattering distributions, and by adding layer effects in the form of Dirac deltas.

The specific research questions stated in Section 1.6 are addressed in the following.

- Can different subsurface structures be recognized in InSAR, Pol-InSAR, and SAR Tomography measurements?

The subsurface structure has an effect on InSAR coherences, but it is not trivial to invert that relationship and derive subsurface characteristics from InSAR measurements. The measured coherences indicate the vertical spread of the backscattering and the depth of scattering centroid, but this is not yet a clear link to actual subsurface structure. In general, subsurface structures can be recognized from InSAR and Pol-InSAR only through modeling. More specifically, the effect of distinct subsurface layers was observed through a coherence magnitude undulation with vertical wavenumber k_{zVol} in single channel InSAR coherences at the South Dome test site. Using the model introduced in Chapter 2, the vertical distance between the layers can be assessed as well as their relative scattering contribution in terms of layer-to-volume ratios, based on single channel InSAR data. The added polarimetric observation space by means of Pol-InSAR allows a further characterization of the layer effects, due to the higher sensitivity of the HH and VV channel to their characteristic surface scattering mechanism, compared to the HV channel. Therefore, the presence of subsurface layers can be recognized in InSAR and Pol-InSAR data, but the retrieval of further subsurface structure information requires additional physical modeling to provide a link to geophysical parameters.

SAR tomography is more powerful to observe subsurface structures due to the 3-D imaging capability. In this way, not only layers can be identified but also the vertical distribution of the backscattering can be derived, which can provide more insights into subsurface structures. For instance, the vertical backscattering distributions, derived with SAR tomography, at the EGIG T05 test site in the lower percolation zone are characterized by a steep increase at the top and a gradual drop towards greater depths. This is related to the homogeneous presence of refrozen melt features in the subsurface. At South Dome, the vertical backscattering distributions tend to be vertically more symmetrical and dominated by distinct layers. Therefore, SAR tomography represents a great tool to assess the effects of melt-refreeze processes on the subsurface structure.

In addition, SAR tomography revealed that the assumption of scattering from the snow surface or a snow-firn interface does not necessarily apply, which was used in earlier studies [3], [4]. The thickness of the transparent part below the surface in the investigated data is 1 m at X-band and up to 5 m in the HV channel at L- and P-band, which includes even young firn from the last 1-3 years.

- Are different polarizations and frequencies providing additional information content?

Different frequencies provide complementary information content, which is related to the deeper penetration capabilities of longer wavelengths as well as the sensitivity to scatterers of different size. For instance, the distance between the subsurface layers at the South Dome test site was estimated to be 4.75 m at P- and L-bands and 3.0 m for C- and X-bands, based on the model introduced in Chapter 2. The comparison with GPR data and SAR tomography confirmed these layer distances and showed that P- and L-bands are indeed sensitive to deeper subsurface layers than C- and X-bands. Apart from layers, the work in this thesis confirms that deeper backscattering contributions can be investigated with longer wavelengths. The choice of frequency is therefore important, whether the goal is to gain sensitivity to surface or to subsurface properties.

The added value of polarimetric data is also confirmed by this thesis. HH and VV channels are more sensitive to the scattering from refrozen melt layers than the HV channel, (see Chapter 2) while the latter is more sensitive to the volume component. In addition, the HV signals penetrate deeper (see Chapter 3). For the estimation and correction of InSAR penetration bias, polarimetric data mainly provides the means to reduce the variance of the estimates (see Chapter 4). Towards future approaches of geophysical subsurface information retrieval, the added information content of polarizations will be essential in order to distinguish between different scattering contributions, e.g., from distinct layers and the firn volume.

- Are existing models accurate enough to describe the effect of the vertical backscattering distribution in the subsurface of ice sheets on InSAR data?

Regarding existing models, it is mainly referred to the UV [5] and RVuG [3], [4] models. They all rely on the assumption of a constant signal extinction in the entire subsurface, which results in the exponential backscattering distribution. As demonstrated in Chapter 2, they cannot account for more complex scattering scenarios with distinct subsurface layers, as well as shifted or skewed vertical backscattering distributions (see Chapter 3). A crucial limitation is that existing models fail to describe InSAR phase center depths in all frequencies and polarizations at the investigated test sites (see Chapter 4). This is in agreement with the underestimation of the phase center depth reported in [3].

However, it is an interesting finding of this thesis that the simple introduction of a vertical shift in the UV model leads to significant improvements in the simulations of vertical backscattering distributions and coherences, as well as in the estimation of phase center depths.

- To what extent are the investigated models applicable to different areas, frequencies, and polarizations?

The models described in this thesis are generic and therefore applicable at different frequencies or polarizations. Being focused on the simulation of Pol-InSAR data based on vertical backscattering distributions, such models are not necessarily limited to applications for ice sheets or glaciers. Even the application to other media that are characterized by microwave penetration, like dry sand in deserts, is possible.

Focusing on ice sheets, the model assessment in Chapter 3 shows that the preferred model choice is very consistent across polarizations and frequencies. The consistency across polarizations is particularly important for Pol-InSAR approaches. While the UV model with a shift performs generally the best among all investigated areas, frequencies, and polarizations, there is a slight tendency that models which can account for more symmetrical vertical backscattering distributions, like the Weibull model, are equally or more suitable to describe the subsurface scattering in the upper percolation zone.

The research in this thesis was focused on the percolation zone. One could speculate, that the investigated volume models could also be suitable for the dry snow zone, where a relatively homogeneous subsurface structure is expected without large scatterers formed by refreezing of melt water. In contrast, tomographic studies in the ablation zone have revealed very heterogeneous subsurface structures [6], [7] which might require different modeling approaches.

- Is the vertical backscattering distribution in the subsurface of ice sheets polarization dependent and to which extent does this have to be considered in the modeling?

The polarization dependence of the vertical backscattering distribution is important for Pol-InSAR applications. Polarization independent scattering processes can be modeled identically for all polarization channels, which reduces the parameter space. In contrast, polarized scattering has to be considered by polarization dependent model parameters.

Subsurface layers have a clearly polarization dependent effect on Pol-InSAR data. The depth of the layers is consistent across polarizations, but the cross-polarized layer-to-volume scattering ratios are smaller than at the co-polarized channels (see Chapter 2). This fits to the interpretation of layer scattering with a surface scattering mechanism.

Tomographic profiles in different polarizations were also used in Chapter 3 to assess the polarization dependence of the vertical backscattering distributions without the layers. On the one hand, they appear differently across polarizations, indicating a polarization dependent distribution of the scatterers. On the other hand, the differences between coherence magnitudes at different polarizations can be small, since large parts of such differences are caused by vertical shifts between the vertical profiles of the polarizations, which only affect the phase term of the coherence but not its magnitude. Therefore, a random volume assumption could still be a sufficient approximation for applications focusing on coherence magnitudes.

- Do the investigated models provide a link to the geophysical subsurface properties?

The multiple-layer-plus-volume model introduced in Chapter 2 is used to derive the vertical distance between dominant subsurface layers and to infer layer-to-volume scattering ratios, revealing the relative importance of different scattering mechanisms. Therefore, the modeling in this thesis provides a link to layers of refrozen melt water, which could support the assessment of accumulation rates, density changes, or melt-refreeze processes. The volume models investigated in this thesis provide a first link to the subsurface distributions of refrozen ice inclusions, and can indicate for instance the homogeneous presence of such features throughout the subsurface in the lower percolation zone. However, inversion techniques remain to be established and more advanced parameterizations of the layer and volume models are necessary to retrieve geophysical information. Still, the modeling in this thesis provides the foundation for further research in this direction.

- Can the models be used to estimate the penetration bias in InSAR surface elevation measurements (DEMs) and how accurate is the estimation?

Interestingly, in contrast to coherence magnitudes, the effect of the layers on the interferometric phase center depth can be approximated with volume only models. The layers pull the phase centers below the limit of a conventional UV model, but a similar behavior is also observed for the improved volume models investigated in this thesis. Therefore, volume models are appropriate to describe the phase centers depths even in the presence of distinct subsurface layers.

The proposed model inversions clearly provide more accurate surface elevation estimates than using the directly measured interferometric phase center location (Chapter 4). The models can account for most of the penetration bias and compensate the baseline dependence of the measured phase center depths to a large extent. However, one has to accept that the retrieved surface location does not necessarily correspond to the real surface, since the tomographic profiles in Chapter 3 showed that the surface and the first few meters below the surface can be transparent, particularly at lower frequencies. Therefore, the model-based estimates of the surface elevation are on average still slightly below the real surface. Nevertheless, the inversion of such a “radar surface” can clearly provide more reliable topographic information over ice sheets than using the pure interferometric phase information. The Weibull model inversion provides estimates which are on average closest to the real surface but suffer from a larger variance. Given the performance of the UV inversion and since it can be applied to any single channel interferometric coherence, the main conclusion is that UV surface estimations should be preferred over the sole phase center information, as long as other decorrelation sources, e.g. temporal decorrelation, can be neglected or accurately compensated. On average, the penetration bias is reduced by a factor of 2.5 to 6.5 with the single-polarization UV model inversion, for instance from -7.8 m to -2.3 m in the L-band HH data at South Dome. The accuracy can be

further improved by incorporating the full polarimetric observation space of Pol-InSAR measurements in the UV model inversion.

The model-based compensation of the penetration bias is particularly relevant for the derivation of surface elevation changes through comparison with other elevation measurements, e.g., from altimetry or optical stereo photogrammetry. In case the surface elevation change is derived from InSAR DEMs acquired by the same sensor at different dates (InSAR DEM differencing), only the temporal variation of the penetration bias is relevant. For instance, if the subsurface firn structure would change from the scenario at South Dome, due to increased melting, to a different subsurface structure similar to the EGIG T05 test site, the difference in the average penetration bias in L-band in HH would be 2.1 m, which would propagate directly as an error in the elevation change estimation. This error can be reduced by 40% with the single polarization UV model inversion and by over 50% with the fully polarimetric UV inversion. In general, the differences in the phase center depths of the two test sites are always larger than the differences in the model-based surface estimates at all frequencies and polarizations (by a factor of at least 1.2 and up to 4.9, see Chapter 4). Therefore, the model-based compensation of the penetration bias also improves the accuracy of surface elevation changes estimated from InSAR DEM differencing. This benefit is even stronger for InSAR DEMs acquired at different frequencies or polarizations, for instance when SRTM C-band measurements are compared to TanDEM-X data to achieve a large temporal separation. If InSAR DEMs are generated at the same snow and ice conditions and acquisitions parameters, except for a difference in baseline, which is a likely scenario for space borne SAR, only the baseline dependence of the penetration bias is relevant, which is also accounted for by the model-based inversions.

5.3 IMPLICATIONS AND OUTLOOK

One important implication for the field of (Pol-)InSAR applications over ice sheets is the understanding of the potential complexity of the subsurface scattering and its influence on interferometric coherences. It should be clear that areas on ice sheets exist, where the assumption of a uniform signal extinction in the subsurface is not valid. This thesis demonstrates that more flexibility is required in the modeling of the vertical backscattering distribution and that distinct layers have to be accounted for. The contributions of this thesis provide the modeling tools to address this and pave the way for future applications.

One possible application is the estimation and compensation of the penetration bias in InSAR DEMs, which is also a key contribution of this thesis. Based on Chapter 4, the estimation of a “radar surface”, which might be below the real surface due to microwave transparency of snow and young firn, is recommended for interferometric surface elevation measurements. The use of polarimetric InSAR data for the UV inversion and the novel Weibull inversion indicated the potential for further improvements of the penetration bias compensation. Even though the estimation with pure volume models was also successful for the test site with dominant subsurface layers, there is, as an outlook, the potential to account also for layers in the penetration bias estimation. However, the added complexity leads to more demanding

requirements on the observation space, i.e., dual-baseline fully polarimetric InSAR data. Furthermore, the ice sheet wide application with space borne data requires a validation across larger areas and different glacier zones than covered by this thesis.

The investigated penetration bias compensation is of particular relevance for future long wavelength SAR missions like Tandem-L [2], which are perfectly suited to derive monthly surface elevations of entire ice sheets with few tens of meters spatial resolution. Further improvements of such model-based Pol-InSAR surface elevations can be achieved by the combination with altimetry measurements [8], [9], which have a higher vertical accuracy in the cm-range, but lack the spatial and temporal coverage and resolution of a SAR system. Altimeters are also limited to smooth and flat terrain and are therefore mainly suited for the interior of ice sheets. The synergy of the high vertical accuracy of altimeter measurements with the coverage and resolution of upcoming SAR missions could therefore provide surface elevation measurements of entire ice sheets, both in the interior and in more complex terrain near the ice sheet margins, with an unprecedented combination of vertical accuracy, coverage, and resolution.

The tradeoff between the model complexity and the observation space of Pol-InSAR data has to be considered as well in future model inversion approaches towards subsurface information retrieval. The development of inversion techniques depends on the observation scenario as well as on the subsurface characteristics of the area under investigation. A simple case, which roughly represents the subsurface of the test site in the upper percolation zone of Greenland, consists of two layers and a polarization independent UV model with a vertical shift. The resulting twelve model parameters could be theoretically inverted with a dual-baseline Pol-InSAR setup providing twelve observables. Any additional layer or a polarization dependent volume (i.e. oriented volume) would result in at least two additional model parameters and will complicate the inversion.

There is potential in improving the parameterization with more physical volume and layer scattering models, when larger observation spaces can be exploited in the form of multi-baseline Pol-InSAR data. For instance, through a more explicit volume scattering modelling [10], [11] or the parameterization of the polarimetric scattering from refrozen ice inclusions based on their shape and orientation [12]. However, this research direction leads quickly to potentially ambiguous solutions in the model inversions based on Pol-InSAR data, because the required parameter space is likely larger than the observation space. Clever retrieval strategies have to be developed in order to reduce the requirements on a priori information or model assumptions.

As a next step towards the retrieval of geophysical subsurface information, cooperation with the glaciological community and researchers in the fields of ground penetration radar and radar sounders are recommended. This will not only contribute to closing the gap between the modeling of Pol-InSAR measurements and the geophysical properties of the subsurface of ice sheets, but also help identifying the added value of Pol-InSAR information and potential applications more precisely.

5.4 REFERENCES

[1] G. Fischer, G. Parrella, K. P. Papathanassiou, and I. Hajnsek, "Sensitivity of polarimetric SAR interferometry data to different vertical subsurface structures of the Greenland ice sheet," in *Proceedings of IGARSS*, Forth Worth, USA, 2017, pp. 3581–3584.

[2] A. Moreira, G. Krieger, I. Hajnsek, K. Papathanassiou, M. Younis, P. Lopez-Dekker, S. Huber, M. Villano, M. Pardini, M. Eineder, F. De Zan, and A. Parizzi, , "Tandem-L: A Highly Innovative Bistatic SAR Mission for Global Observation of Dynamic Processes on the Earth's Surface," *IEEE Geoscience and Remote Sensing Magazine*, vol. 3, no. 2, pp. 8–23, Jun. 2015.

[3] J. Dall, K.P. Papathanassiou, and H. Skriver, "Polarimetric SAR interferometry applied to land ice: Modeling," in *Proceedings of EUSAR*, Ulm, Germany, 2004, pp. 247-250.

[4] J. Sharma, I. Hajnsek, K.P. Papathanassiou, and A. Moreira, "Estimation of glacier ice extinction using long-wavelength airborne Pol-InSAR," *IEEE Transactions on Geoscience and Remote Sensing*, vol. 51, no. 6, pp. 3715-3732, Jun. 2013.

[5] E. W. Hoen and H. Zebker, "Penetration depths inferred from interferometric volume decorrelation observed over the Greenland ice sheet," *IEEE Transactions on Geoscience and Remote Sensing*, vol. 38, no. 6, pp. 2571–2583, Nov. 2000.

[6] F. Banda, J. Dall, and S. Tebaldini, "Single and Multipolarimetric P-Band SAR Tomography of Subsurface Ice Structure," *IEEE Transactions on Geoscience and Remote Sensing*, vol. 54, no. 5, pp. 2832–2845, May 2016.

[7] M. Pardini, G. Parrella, G. Fischer, and K. Papathanassiou, "A Multi-Frequency SAR Tomographic Characterization of Sub- Surface Ice Volumes," in *Proceedings of EUSAR*, Hamburg, Germany, 2016, pp. 1-6.

[8] V. Helm, A. Humbert, and H. Miller, "Elevation and elevation change of Greenland and Antarctica derived from CryoSat-2," The Cryosphere, vol. 8, no. 4, pp. 1539–1559, 2014.

[9] H. J. Zwally, J. Li, A. C. Brenner, M. Beckley, H. G. Cornejo, J. DiMarzio, M. B. Giovinetto, T. A. Neumann, J. Robbins, J. L. Saba, D. Yi, and W. Wang, "Greenland ice sheet mass balance: distribution of increased mass loss with climate warming; 2003–07 versus 1992–2002," Journal of Glaciology, vol. 57, no. 201, pp. 88–102, 2011.

[10] C. Mätzler, "Improved Born approximation for scattering of radiation in a granular medium," *Journal of Applied Physics*, vol. 83, no. 11, pp. 6111–6117, Jun. 1998.

[11] G. Picard, M. Sandells, and H. Löwe, "SMRT: an active–passive microwave radiative transfer model for snow with multiple microstructure and scattering formulations (v1.0)," *Geoscientific Model Development*, vol. 11, no. 7, pp. 2763–2788, Jul. 2018.

[12] G. Parrella, I. Hajnsek, and K. P. Papathanassiou, "Polarimetric decomposition of L-band PolSAR backscattering over the Austfonna ice cap," *IEEE Transactions on Geoscience and Remote Sensing*, vol. 54, no. 3, pp. 1267–1281, Mar. 2016.

6 CURRICULUM VITAE

Personal Information

First name / Surname	Georg Fischer
Work Address	German Aerospace Center (DLR), Münchener Strasse 20, 82234 Wessling, Germany.
Telephone	+49 8153-28-3068
E-mail	fischer_georg@gmx.net
Date of Birth	29.03.1986

Professional Experience

Since April 2013	PhD Candidate
Thesis Title	"Modeling of Subsurface Scattering from Ice Sheets for Pol-InSAR Applications" ▪ Planning and execution of an airborne SAR campaign and in situ measurements in Greenland. ▪ Polarimetric, interferometric and tomographic processing of SAR data. ▪ Model development for Pol-InSAR applications over ice sheets. ▪ Supervision of guest scientists and internship students. German Aerospace Center (DLR), Münchener Strasse 20, 82234 Weßling, Germany.
April 2013 – March 2014	Administrative Coordinator of the Helmholtz Alliance: Remote Sensing and Earth System Dynamics German Aerospace Center (DLR), Münchener Strasse 20, 82234 Weßling, Germany.
February 2012 – February 2013	Traineeship Support to scientific preparation activities of ESA's Earth Explorer candidates CoReH2O and Biomass. European Space Agency, Keplerlaan 1, 2200 AG Noordwijk, The Netherlands.
October 2008 – December 2011	Scientific Assistant (part-time job) Support to projects: ▪ CLIMB – Climate Induced Changes on the Hydrology of Mediterranean Basins ▪ Validation of EADS SmartRadar data ▪ Understanding Directionality in Surface Scattering by Imaging Radar Department of Geography, Ludwig-Maximilians-University Munich. Luisenstraße 37, 80333 Munich, Germany
February – March 2009	Internship Processing and analysis of multitemporal Envisat ASAR and ERS-2 SAR data for the detection of directional scattering effects on agricultural fields GAMMA Remote Sensing AG, Worbstrasse 225, 3073 Gümligen, Switzerland

Education

Since November 2013	PhD Studies
Thesis Title	"Modeling of Subsurface Scattering from Ice Sheets for Pol-InSAR Applications"
	ETH Zurich, Institute for Environmental Engineering, Zurich, Switzerland.
October 2009 – January 2012	Master of Science in Environmental Systems and Sustainability - Monitoring, Modelling, Management
Thesis Title	"Potential of SAR Interferometry for the Detection of Subsidence in the Western Nile Delta, Egypt"
	Ludwig-Maximilians-University Munich, Germany.
October 2006 – August 2009	Bachelor of Science in Physical Geography, minor subject Informatics
Thesis Title	"Understanding Directionality in Surface Scattering by Imaging Radar"
	Ludwig-Maximilians-University Munich, Germany.
1996 – 2005	Abitur (Intensive courses: Physics and Geography)
	Hans-Leinberger Gymnasium Landshut, Germany.

Training Courses

Since April 2013	DLR Graduate Program ▪ The basics of communication ▪ Speed reading ▪ Basics of project management ▪ Rhetoric and personality ▪ Effective scientific presentations ▪ Project management – follow up ▪ Effective scientific presentations – follow up ▪ How to publish in peer-reviewed journals ▪ Basics of business administration German Aerospace Center (DLR)
July 2019	1-day course on "Remote Sensing with Reflected Global Navigation Satellite System and Signals of Opportunity". Tutorial of the International Geoscience and Remote Sensing Symposium.
July 2017	1-day course on "Machine Learning in Remote Sensing". Tutorial of the International Geoscience and Remote Sensing Symposium.
July 2016	2-week Summer School Alpbach: Development of a space mission concept for radar altimetry for snow water equivalent estimation. European Space Agency, ESA, and Austrian Research Promotion Agency, FFG.
June 2014	1-day course on "Multistatic and Multi-Aperture SAR Systems: Introduction and Applications". Tutorial of the European Conference on Synthetic Aperture Radar.
October 2013	5-day course "SAR Principles and Applications". Carl-Cranz-Gesellschaft e. V.

January 2013	5-day course “Advanced Course on Radar Polarimetry”. European Space Agency, ESA.
March 2012	2-day course on “Introduction to Space Systems Engineering” European Space Agency, ESA.

Awards

2018	Student Paper Award (Third place) at the European Conference on Synthetic Aperture Radar, EUSAR.

Publications

Journals	G. Fischer, K. P. Papathanassiou, and I. Hajnsek, “Modeling and Compensation of the Penetration Bias in InSAR DEMs of Ice Sheets at Different Frequencies,” submitted to *IEEE Journal of Selected Topics in Applied Earth Observations and Remote Sensing*, October 2019. G. Fischer, M. Jäger, K. P. Papathanassiou, and I. Hajnsek, “Modeling the Vertical Backscattering Distribution in the Percolation Zone of the Greenland Ice Sheet with SAR Tomography,” accepted for publication in *IEEE Journal of Selected Topics in Applied Earth Observations and Remote Sensing*, October 2019. G. Fischer, K. P. Papathanassiou, and I. Hajnsek, “Modeling Multifrequency Pol-InSAR Data From the Percolation Zone of the Greenland Ice Sheet,” *IEEE Transactions on Geoscience and Remote Sensing*, vol. 57, no. 4, pp. 1963–1976, Apr. 2019. J. Sušnik, L. S. Vamvakeridou-Lyroudia, N. Baumert, J. Kloos, F. G. Renaud, I. La Jeunesse, B. Mabrouk, D. A. Savić, Z. Kapelan, R. Ludwig, G. Fischer, R. Roson, and C. Zografos, “Interdisciplinary assessment of sea-level rise and climate change impacts on the lower Nile delta, Egypt,” *Science of The Total Environment*, vol. 503–504, pp. 279–288, Jan. 2015. U. Wegmüller, M. Santoro, F. Mattia, A. Balenzano, G. Satalino, P. Marzahn, G. Fischer, R. Ludwig, and N. Floury, “Progress in the understanding of narrow directional microwave scattering of agricultural fields,” *Remote Sensing of Environment*, vol. 115, no. 10, pp. 2423–2433, Oct. 2011.
Conferences	G. Fischer, G. Parrella, K. P. Papathanassiou, and I. Hajnsek, “Investigating the Potential to Estimate InSAR Penetration Depth over Ice Sheets from Pol-InSAR Data,” in *Proceedings of IGARSS*, Yokohama, Japan, 2019. G. Fischer, K. P. Papathanassiou, and I. Hajnsek, “Investigating the Potential to Retrieve Vertical Subsurface Structures of Ice Sheets by Means of Pol-InSAR Data,” in *Proceedings of ESA POLinSAR Workshop*, Frascati, Italy, 2019. G. Fischer, M. Pardini, G. Parrella, K. P. Papathanassiou, and I. Hajnsek, “Cancellation of Dominant Scattering Layers in Greenland’s Subsurface for the Characterization of Ice Volumes,” in *Proceedings of EUSAR*, Aachen, Germany, 2018. G. Fischer, K. P. Papathanassiou, and I. Hajnsek, “Recent Advances Towards Glacier Subsurface Information Retrieval by Means of Tomographic SAR Techniques,” in Pro*ceedings of ESA BioGeoSAR Workshop*, Oberpfaffenhofen, Germany, 2018. G. Fischer, G. Parrella, K. P. Papathanassiou, and I. Hajnsek, “Sensitivity of polarimetric SAR interferometry data to different vertical subsurface structures of the Greenland ice sheet,” in *Proceedings of IGARSS*, Forth Worth, USA, 2017.

	G. Fischer, G. Parrella, K. P. Papathanassiou, and I. Hajnsek, "Impact of vertical subsurface structure, frequency and polarization on the accuracy of InSAR phase center depth modelling for glaciers and ice sheets," in *Proceedings of ESA POLinSAR Workshop*, Frascati, Italy, 2017.
	G. Fischer and I. Hajnsek, "Investigation of Penetration Bias of Surface Elevation Models From SAR Interferometry in Dependence of Subsurface Structure, Frequency and Polarization," in *Proceedings of EARSeL Workshop on Land Ice and Snow*, Bern, Switzerland, 2017.
	G. Fischer, G. Parrella, K. P. Papathanassiou, and I. Hajnsek, "Interpretation of Pol-InSAR signatures from glaciers and ice sheets at different frequencies," in *Proceedings of EUSAR*, Hamburg, Germany, 2016.
	M. Pardini, G. Parrella, G. Fischer, and K. Papathanassiou, "A Multi-Frequency SAR Tomographic Characterization of Sub-Surface Ice Volumes," in *Proceedings of EUSAR*, Hamburg, Germany, 2016.
	G. Fischer and I. Hajnsek, "Dual-Pol X-Band Pol-InSAR Time Series of a Greenland Outlet Glacier," in *Proceedings of ESA POLinSAR Workshop*, Frascati, Italy, 2015.
	G. Fischer, I. Hajnsek, and K. P. Papathanassiou, "Temporal Variations of X-Band Pol-InSAR Coherence over Glaciers," in *Proceedings of EARSeL Workshop on Land Ice and Snow*, Bern, Switzerland, 2014.
	G. Fischer, I. Hajnsek, and K. P. Papathanassiou, "Pol-InSAR Signatures of Glaciers at X-Band: A Preliminary Analysis," in *Proceedings of EUSAR*, Berlin, Germany, 2014
	U. Wegmüller, M. Santoro, F. Mattia, A. Balenzano, G. Satalino, P. Marzahn, G. Fischer, R. Ludwig, and N. Floury, "Progress in the Understanding of Narrow Directional Scattering over Agricultural Fields," in *Proceedings of the ESA Living Planet Symposium*, Bergen, Norway, 2010.
Other	ESA (2012): Report for Mission Selection: Biomass. ESA SP-1324/1 (3 volume series), European Space Agency, Noordwijk, The Netherlands.